Measurement and Application of Heat Generation from Gold Nanoparticle Systems under Laser Irradiation in Biomedicine

A Dissertation
SUBMITTED TO THE FACULTY OF
UNIVERSITY OF MINNESOTA
BY

Yiru Wang

IN PARTIAL FULFILLMENT OF THE REQUIREMENTS
FOR THE DEGREE OF
DOCTOR OF PHILOSOPHY

Advisor: John C. Bischof

March. 2019

Acknowledgements

This work is only made possible under the help of my advisor, collaborators, colleagues, friends and family members.

I am very grateful for the privilege of joining Bioheat and Mass Transfer Lab and being advised by Dr. John Bischof. The education and training I received has defined who I am for my life and career. Dr. Bischof taught me the most important skills and knowledge for being an independent researcher, and his vision and attitude towards work and life will always inspire me. I want to thank him for his patience, trust, persistence and guidance during these years.

Thanks to my collaborators for their generous contribution to this work. Dr. Scott Prahl and Dr. Chris Hogan provided the missing pieces of my projects. Dr. Xiaojia Wang, Dr. Taner Akkin, Dr. Zhenpeng Qin and Dr. Warren Chan provided insightful directions to my research. The clinical studies would not be possible without the help of Dr. David Boulwere, Dr. Bobbi Pritt, Dr. Iveth González, Dr. Steffen Rameil, Dr. Daniel Larkin and other clinical collaborators. Thanks also to our industrial collaborator Dr. John Ballard for his inputs to a portable and industrial version of Thermal Contrast Reader.

I would also like to acknowledge current and former members of our lab. I feel so proud being part of the BHMT team. They are all intelligent and supporting people who inspired me a lot by their work and ideas. Special thanks to Dr. Zhenpeng Qin, under whose help I started my research and life in a new country. Dr. Qin is a model showing how far one can reach by hard work.

To my parents and my fiancé Ying Lin, your contained, unconditional love supported me going through the uncertainty and anxiety of these years. You believe in me, celebrate the smallest progress I made, and never stop shaping me into a better person.

Abstract

Gold nanoparticles (GNPs) are widely used for biomedical applications due to their unique optical properties, established synthesis methods, and biological compatibility. The tunable surface plasmon resonance in a wide range (visible to NIR) makes GNPs a favorable heat generator for photothermal hyperthermic treatment and many emerging new fields. All of these biomedical applications rely on geometry, concentration, distribution and interaction with the media to create bulk heat generation. This heat generation is usually estimated under idealized condition assumptions. However, in real conditions, GNPs are polydisperse in size, their distribution is not homogeneous, and their media is absorbing and scattering.

Currently we are unaware of any standard methods for systematically studying the non-idealized factors for GNP heating systems. We aim to address this need by providing precise measurement approaches of GNP heating a highly scattering membrane and aqueous solution using the integrating sphere spectrophotometry approach and cuvette laser calorimetry. Specifically, these are applied to characterize a Thermal Contrast Amplification Reader and the effect of GNP aggregation. Both methods can be extended to other non-idealized conditions such as gel, cell suspension and GNP-laden tissues or tumors. This work aims to provide reproducible, simple, and precise evaluation of bulk heat generation in paper-based and solution GNP-laden systems and examples of application in preservation, diagnostics and therapeutics.

Table of Contents

List of Tables

List of Figures

Chapter 1 Introduction to Gold Nanoparticle Heating in Biomedicine

Part of this chapter was published in the following citation:

- Qin, Z., **Wang, Y.**, Randrianalisoa, J., Raeesi, V., Chan, W. C. W., Lipiński, W., & Bischof, J. C. "Quantitative comparison of photothermal heat generation between gold nanospheres and nanorods." *Scientific Reports* 6 (2016): 29836.

1.1 Gold Nanoparticles

Gold nanoparticles (GNPs) in engineering and medical applications are usually 1 to 200 nm in size with well-controlled geometries and properties. GNPs are generally prepared by reduction of gold salts with stabilizing agents preventing agglomeration varied by targeting particle size and shape.[1] GNPs also enjoy easy surface modification since the amine and thiol groups bind strongly to them with good biocompatibility.[2] The plasmonic heating capability of GNPs relays comes from their optical properties, which are tunable to a wide range by varying size, shape, and suspension conditions.

1.2 Gold Nanoparticle Plasmonic Heating

Advances in material synthesis have produced a library of plasmonic nanomaterials with varying size, shape and composition[3–6]. These nanostructures are used in many biomedical

applications including disease diagnosis[7–9] and treatment based on their optical properties[10,11]. For instance, in diagnostics, nanoparticles have been used for visual labels for colorimetric bioassays including aggregation assays[12] and lateral flow dipstick tests[13]. For therapeutics, nanomaterials have been studied to serve as drug nano-carriers[14], and photothermal agents for tumor ablation once delivered to the tumor,[15] and agents for warming of cryopreserved bio-systems. For all of these applications, it is increasingly important to precisely characterize the heat generation of GNPs in real systems to ensure reproducible bio-sensing and effective therapies[16].

For GNP alone, nanoparticle size, shape and composition determine the heat generation. For instance, given a nanomaterial, the size and shape determine the optical properties and interactions with a biological system. In the case of gold nanospheres (GNS), the plasmon resonance and hence color can be tuned within the visible spectrum from clear pink to dark red by changing the diameter (30–100 nm), and in the case of gold nanorods (GNR), the plasmon resonance can be tuned to the visible to near-infrared (NIR) spectrum from 600 nm to 1400 nm by changing their aspect ratios[5,17].

The biological responses, including cellular uptake[18], internationalization pathway[19], peri-vascular distribution in tumor[20] and cytotoxicity[21], are also size- and shape-dependen. Although there have been both theoretical[22–26] and experimental[27–30] approaches to quantitatively account for photothermal heat generation from plasmonic nanostructures, there are no studies that integrate the experimental and theoretical approaches to quantify the heat generation, often leading to discrepancies[31]. This in turns leads to difficulties in predicting the therapeutic and diagnostic

outcomes and comparing the heat generating capability of new plasmonic nanostructures in biomedical applications.

As theoretical approaches, Mie theory and Discrete Dipole Approximation (DDA) are

$$Q_{\text{ext}} = \frac{2}{x^2}\sum_{n=1}^{\infty}(2n+1)\text{Re}(a_n + b_n) \tag{1.1}$$

$$Q_{\text{sca}} = \frac{2}{x^2}\sum_{n=1}^{\infty}(2n+1)[|a_n|^2 + |b_n|^2] \tag{1.2}$$

$$Q_{\text{abs}} = Q_{\text{ext}} - Q_{\text{sca}} \tag{1.3}$$

$$g = \frac{4}{x^2 Q_{sca}}\sum_{n=1}^{\infty}\left[\frac{n(n+2)}{n+1}\ \text{Re}\ (a_n a_{n+1}^* + b_n b_{n+1}^*) + \frac{2n+1}{n(n+1)}\ \text{Re}\ (a_n b_n^*)\right] \tag{1.4}$$

$$a_n = \frac{\psi'_n(mx)\psi_n(x) - m\psi_n(mx)\psi'_n(x)}{\psi'_n(mx)\zeta_n(x) - m\psi_n(mx)\zeta'_n(x)} \tag{1.5}$$

$$b_n = \frac{m\psi'_n(mx)\psi_n(x) - \psi_n(mx)\psi'_n(x)}{m\psi'_n(mx)\zeta_n(x) - \psi_n(mx)\zeta'_n(x)} \tag{1.6}$$

powerful tools to understand the optical properties of GNPs. The Mie theory provides exact values of the far-field extinction, absorption and scattering efficiency and asymmetry factors for a spherical particle suspended in a non-absorbing host medium illuminated by an incident plane wave.[32]

where x is the particle size parameter (=2πa/λ), m is the ratio of complex refractive index ($n_S = \sqrt{\varepsilon_S}$) of the sphere to that of the surrounding medium (n_m), ψ_n and ζ_n are spherical Bessel functions, and the asterisk (*) and prime ($'$) indicate complex conjugate and derivative with respect to the argument x or mx, respectively. DDA is a discrete solution method for the integral

form of Maxwell's equations and allows the prediction of nanostructure optical properties with complex geometries beyond Mie theory. [29] Basically, the target structure is discretized into a finite array of dipoles (N) with each one located at position r_j (j = 1, N). After solving 3 N complex linear equations with unknown dipole moments[33], the extinction, absorption and scattering cross sections and asymmetry factor can by calculated by

$$C_{\text{ext}} = \frac{4\pi\eta}{E_{\text{inc}}^2}\sum_{i=1}^{N}\text{Im}(\mathbf{E}_{\text{inc,i}}^{*}\mathbf{P_i}) \tag{1.7}$$

$$C_{\text{abs}} = \frac{4\pi\eta}{E_{\text{inc}}^2}\sum_{i=1}^{N}\{\text{Im}[\mathbf{P_i}\cdot(\alpha_{\mathbf{i}}{}^{-1})^{*}\mathbf{P_i}^{*}] - \frac{2}{3}\eta^3|\mathbf{P_i}|^2\} \tag{1.8}$$

$$C_{\text{sca}} = C_{\text{ext}} - C_{\text{abs}} \tag{1.9}$$

$$g = \frac{\eta^3}{E_{\text{inc}}^2 C_{\text{sca}}}\int_{4\pi}\mathbf{n}\cdot\mathbf{z}\left|\sum_{i=1}^{N}[\mathbf{P_i} - \mathbf{n}(\mathbf{n}\cdot\mathbf{P_i})]\exp(-i\eta\mathbf{n}\cdot\mathbf{r_i})\right|^2 d\Omega \tag{1.10}$$

where z is the direction of the incident plane wave of amplitude $E_{inc,\,\mathbf{n}}$ is a unit vector of the scattering direction, $d\Omega$ is the differential solid angle around of n, $E_{inc,\,\mathbf{I}}$ is the incident electric field vector on the dipole **i, Pi** is the dipole moment vector, η (=$2\pi/\lambda$) is the wave number, and α_i is the polarizability of the dipole **i**. The predicted photothermal conversion efficiency is defined as:

$$\eta_{theory} = \frac{C_{abs}}{C_{ext}} = \frac{Q_{abs}}{Q_{ext}} \tag{1.11}$$

Moreover, all of the GNP plasmonic heating applications rely on geometry, concentration, distribution, aggregation state and interaction with media to create bulk heat generation. This heat generation is relatively well understood for idealized conditions. However, under real conditions, the GNP distribution is polydisperse and inhomogeneous and the media is absorbing and scattering.

In addition, optical properties such as the dielectric constant that determines the absorption cross section (C_{abs}) are hydration- and temperature-dependent and thus change during heating. These non-ideal factors result in different optical properties from the idealized conditions and thus require further study in real GNP-laden systems (i.e., solutions, gels, biological systems, or lateral flow assays, and many others) for better predicting the therapeutic and diagnostic outcomes (Table 1.1):

Table 1.1. Heat generation from GNP-laden systems.

Heat Generation Parameters	Idealized System	Real System
GNP Concentration	Homogeneous & Monodisperse	Non-homogeneous and possibly Aggregated
Medium	Transparent	Scattering and Absorbing medium
Optical Properties (μ_a, μ_s')	Constant	Variable
Laser Intensity (I)	Constant	Variable
Specific Absorption Rate (SAR) of Heat	Predictable	Un-predictable*

*Based on available information

Currently, we are unaware of any standard method that reconciles nanoscale optical properties with heat generation in real systems. Previous studies have reported a variety of different methods for GNP solutions which fall in to either direct or indirect measurement methods. With indirect methods, the temperature within the sample is tested and the heat generation is approximately calculated by Eq. 1.12:

$$SAR = \rho C_p \left(\frac{dT}{dt} \right)_{initial} \tag{1.12}$$

Since the heat generation (*SAR*) is derived from the initial temperature rising rate in the sample, the results are case specific, and highly limited by temperature measurement. Thus, errors are very likely to be introduced by equipment and measurement. For example, thermocouples measure temperature precisely at a certain spot, but their effects on an original temperature field could be significant based on the geometry of the sample and numbers of thermocouples used in the measurement. On the other hand, non-invasive methods such as magnetic resonance temperature imaging (MRTI) or IR cameras map the 3D or 2D temperature distribution, but also have spatial and temporal resolution problems.[15] Direct measurement methods apply the optical properties and the laser beam parameters to find the heating:

$$u''' = SAR = \mu_a I = NC_{abs} I \quad \left(W / m^3\right) \tag{1.13}$$

where u''' or *SAR* (specific absorption rate) refers to the plasmonic heat generation in the system, μ_a is the absorption coefficient, I is the laser intensity, N is the number concentration of GNPs, and C_{abs} is the absorption cross section of GNP. The direct method is advantageous in studying the principle of the heat generation that could inspire optimization of the system or may be used on similar applications. Reported GNP-laden system heating measurements include laser heating in a water droplet[28], a cuvette in vacuum (isolating heat convection losses)[34], and a cuvette in an environment with standard room temperature and pressure[27]. The results from these studies vary significantly,[28,34] and a relative heat generation was frequently reported due to the lack of known heat generation[27,28,34]. Indirect measurement using photoacoustic imaging offers some insight into

the photothermal absorption[31].

To precisely characterize and improve the heat generation in CW laser heated GNP laden systems, we present two approaches. First, the optical properties of a common paper-based diagnostic (i.e. lateral flow assay) will be measured by a spectrophotometer, and a Monte Carlo and thermal model will be built to evaluate the heat generation during laser irradiation to improve the diagnostic sensitivity. Second, we present a new measurement of heat generation in laser irradiated GNP solutions using a cuvette approach. Here, a central insight is to use a resistive heater as a standard to understand the heat generation within a stirred cuvette where thermocouples record the temperature rise. Further, both methods can be extended to other non-idealized conditions such as aggregation or more complicated systems, such as gel, and cell solutions for the cuvette heating and GNP-laden tissues or tumor for the optical measurement-thermal modeling method[16]. These the two measurements introduced in the following sections will be applied to characterize the heating of real systems that promise to improve thermal contrast amplification (TCA) of lateral flow assay signals and characterize the heating of colloidal gold nanosphere systems.

1.3 Research Goals

In order to characterize and apply GNP heating in biomedicine, the following hypothesis and aims have been proposed.

Hypothesis: Good measurement techniques lead to more precise characterization of GNP-laden system's optical properties and photothermal heating thereby improving the related biomedical application.

Aim 1: Characterize the heating of GNP-laden paper-based systems to construct a thermal reader device for increased diagnostic sensitivity of lateral flow assays at the point of care.

Aim 2: Investigate the effect of GNP aggregation on the photothermal heating to improve the heating of GNPs in a liquid system.

For both aims, optimized heating measurement techniques and numerical modeling will be applied for characterization. With the thermal reader developed in Aim 1, further studies such as clinical cohort study and a new generation of instrumentation and algorithms will also be covered in the following chapters.

1.4 Overview of PhD Dissertation

This dissertation is organized into six chapters that together carry out the aims outlined above. Summaries of the contents and conclusions of each chapter are described below.

Chapter 2. Measurement techniques to quantitatively characterize and predict gold nanoparticle photothermal heating in biomedicine.

This chapter introduces the details of two techniques applied to the applications in this dissertation. The integrating sphere spectrophotometer system provides the optical properties of

GNP-laden paper-based systems that contains lateral flow assays of the thermal contrast amplification technology. And the resister heater calibrated cuvette calorimetry precisely characterized GNP solution heating.

Chapter 3. Apply GNP photothermal heating in a thermal contrast amplification reader yielding 8-fold analytical improvement for disease detection with lateral flow assays.

This chapter describes the thermal contrast amplification reader, an application of GNP heating in *in vitro* diagnostics. The development of the reader's instrumentation, algorithm and data interpretation is introduced in detail. With the reader, validations were done with control samples of three critical infectious diseases: malaria, flu, and *C. difficile* infection. Comparing to human eye and colorimetric commercial reader evaluation, the TCA reader showed improved performance in terms of higher sensitivity and the ability to provide quantitative readouts.

Chapter 4. Improve clinical group a streptococcus detection on rapid diagnostic test assays with thermal contrast amplification reader

The TCA reader's ability to improve clinical infectious diseases diagnosis was examined in this chapter. Instead of the control samples tested in the previous chapter, real clinical positive and negative strep throat patient samples were applied. We show here that a simple add-on thermal contrast reader device can help dramatically improve sensitivity and identify over 50% of the clinically (visual) false negative results. It is a significant step to demonstrate the feasibility and

utility of using our thermal contrast reader device on clinical strep samples vs. research samples. We expect these results to stimulate a larger clinical trial to improve the point-of-care diagnosis of strep throat and other infectious diseases.

Chapter 5. Characterize and Improve Thermal Contrast Amplification Reader for Parameters, Components and Algorithm

The quantitative thermal measurement for GNP heating in a paper method is applied to characterize the TCA of an LFA. To validate the method, we first measured the GNP-laden nitrocellulose membrane of LFA and matched the experimental results. Then the full LFA (membrane with backing layer) was characterized. Key parameters such as laser beam size, laser output power, and backing material thermal properties were studied and optimized with the modeling results. Finally, a high-throughput new reading algorithm was developed, and better-performance new components were selected for the next generation TCA reader.

Chapter 6. Aggregation affects optical properties and photothermal heating of gold nanospheres

The quantitative measurement for GNP heating in solution method was applied to study the effect of aggregation on the laser heating of gold nanosphere solutions. GNP properties estimated by nominal morphology under idealized dilute and mono-disperse conditions can vary dramatically from real situations in biological solutions where the GNPs may be aggregated thereby impacting

GNP heating. We studied the effect of GNP aggregation within a wide range of particle and aggregation sizes. The results show that controlling and/or avoiding aggregation will be necessary for precise dosing of GNP laser heating in biomedical applications. These studies also provide a framework for understanding the impact of aggregation on laser heating of nanostructures.

Chapter 7. Conclusions and future directions

This chapter describes overall conclusions of this dissertation and presents future directions for this field of research.

Chapter 2 Measurement Techniques to Quantitatively Characterize and Predict Gold Nanoparticle Photothermal Heating in Biomedicine

The cuvette laser calorimetry work in this chapter was published in the following citation:

- Qin, Z., **Wang, Y.**, Randrianalisoa, J., Raeesi, V., Chan, W. C. W., Lipiński, W., & Bischof, J. C. "Quantitative comparison of photothermal heat generation between gold nanospheres and nanorods." *Scientific Reports* 6 (2016): 29836. © 2016 Springer Nature Publishing AG

2.1 Quantitative Thermal Measurement for GNP Heating in Paper

The method described in this chapter measures the optical properties of GNP-laden nitrocellulose LFA membrane ('paper'-like porous structure) by a spectrometer with integrating spheres. Monte Carlo ray tracing is applied to directly evaluate the photon transport and interaction in the membrane for the heat generation. Then a finite element model by COMSOL is used to provide with the temperature field in the membrane which is very important information for thermal contrast amplification system. The method scheme is shown in Fig. 2.1:

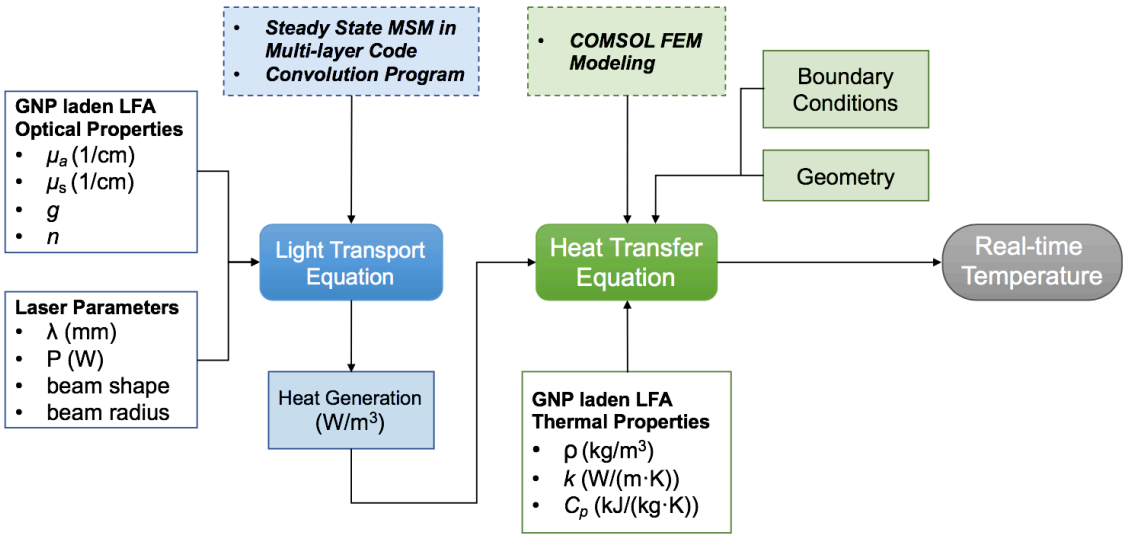

Figure 2.1. Optical-thermal modeling to quantitatively study the heating in a GNP-laden nitrocellulose membrane system.

In simplified cases, the optical properties of GNP-laden material could be obtained by superposition of particles and the properties of the medium linearly under an assumption of uniform distribution.[35,36] However, in our case, the interaction between the GNPs and the medium cannot be neglected. The structure of the membrane, confirmed by SEM scanning, shows that the nitrocellulose frame is highly porous with relatively few GNPs attached (Fig. 2.2). To precisely evaluate the optical properties of our system, an integrating sphere spectrophotometer is applied (Fig.2.2). The spectrophotometer needs to be calibrated according to the manual prior to the measurements. The light source in the system provides a wide spectra range. Only the range around the TCA laser is of interest in this study (450-650 nm). The transmittance of a sample is measured and calculated by: $T=(T'-T_b)/(T_{tot}-T_b)$, where T' is the measured transmitted signal with the sample, T_b is the signal without light source (background noise) and T_{tot} is the signal of total transmittance (nothing between the light and integrating sphere). Similarly, the reflectance is $R=(R'-R_b)/(R_{tot}-R_b)$. The scheme of the spectrophotometer measurements is shown in Figs.2.3 and 2.4. Every sample is measured three times. The fundamental coefficients (μ_a and μ'_s) are calculated by solving an 'inverse problem' based on the light propagation in the material. [37]

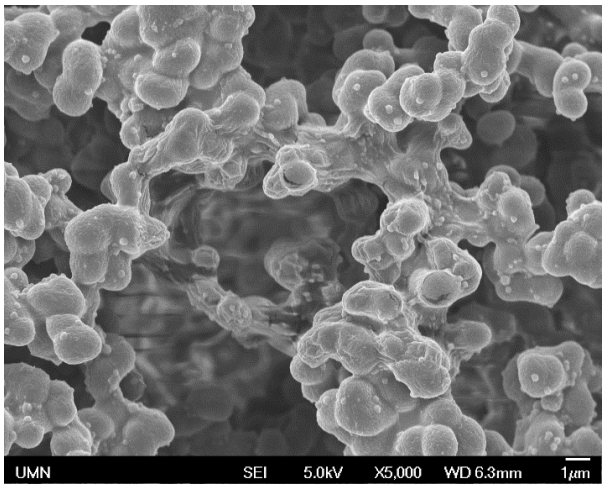

Figure 2.2. SEM picture of GNP-laden nitrocellulose membrane.

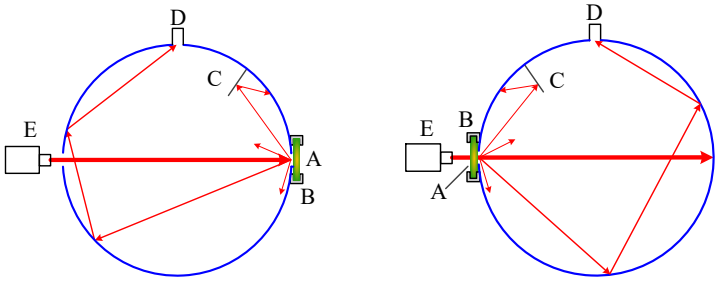

Figure 2.3. Spectrophotometer principle

A: sample, B: sample holder, C: light baffle, D: detector, E: light source.

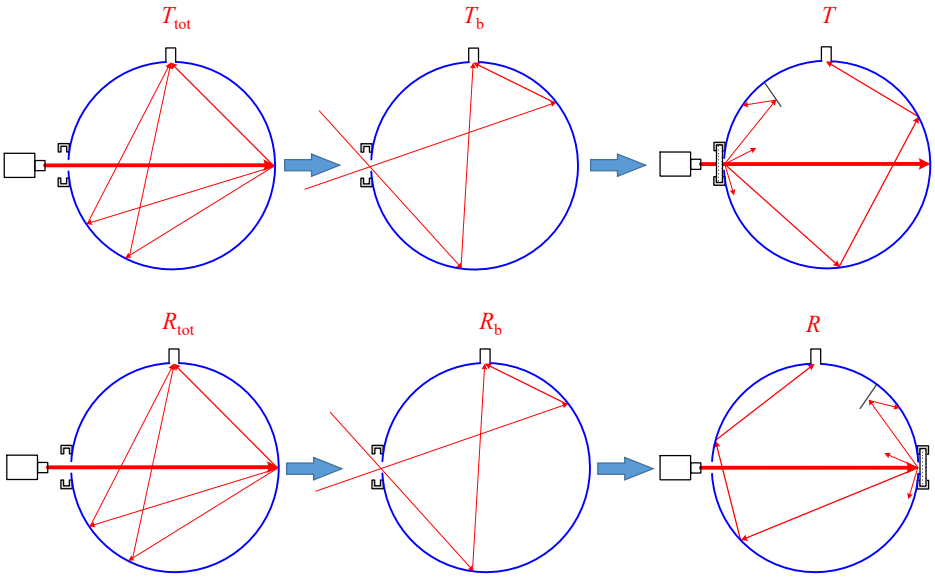

Figure 2.4. Schemes of the spectrophotometer measurements for T and R.

With the optical properties, the heat generation distribution (*SAR*) could be calculated with a Monte Carlo simulation. Since the material of interest in our study is a multi-layer membrane system (nitrocellulose membrane + transparent polyester backing + opaque polystyrene backing), a multi-layered tissue Monte Carlo package by Lihong Wang et al. is applied (Release 5: MCML 1.2.2 & CONV 1.1). [38–41] The inputs of the first MCML program are the geometry parameters (layer thickness) and optical properties of each layer (n, μ_a, μ_s and g). With the laser's parameter (beam shape, beam size and output power) as the input for the CONV program, the heat source profile is obtained as the heat source in put for a COMSOL finite element method thermal model. Since the LFA's characteristic length significantly larger than the laser beam size, 2-D cylindrical geometry is applied to both MCML and COMSOL models.

2.2 Quantitative Thermal Measurement for GNP Heating in Solution

A calibrated, novel and precise cuvette heating system to measure heat generation of GNP solution has been developed (Fig. 2.5). The heat generation calibration mitigates previous difficulties and is a key factor in obtaining accurate thermal measurement. In short, a known amount of energy by resistive heating is delivered using a small resistor in a cuvette.[42] The equilibrium temperature change will be then linearly correlated with the energy input. This linear calibration curve will then be used to quantify the heat generation from laser GNP heating, leading to reproducible and accurate results within the test cuvette.

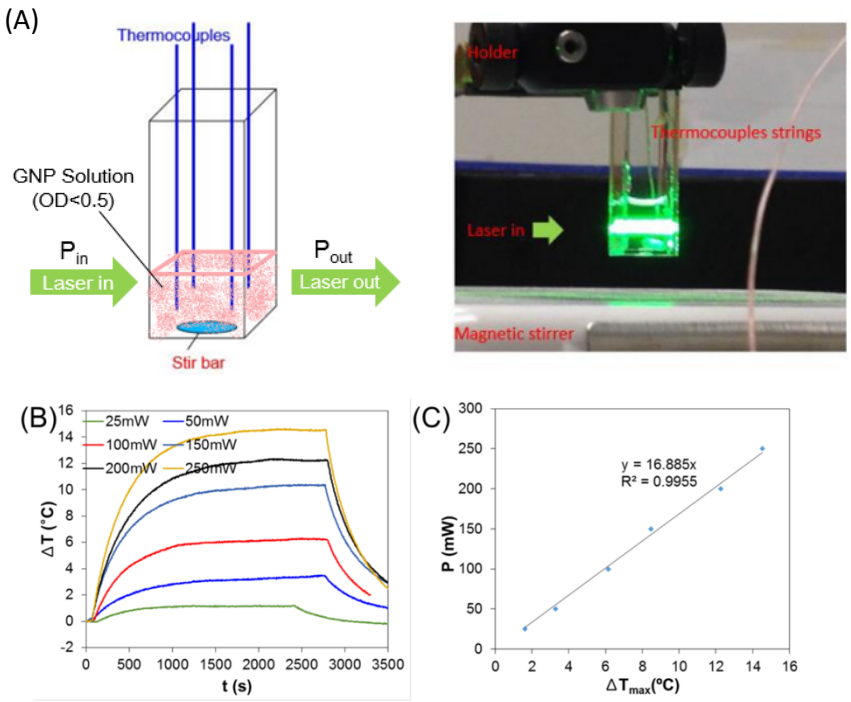

Figure 2.5. Photothermal cuvette bulk heating experimental setup.
(A) Schematic and image of experimental setup; (B-C) Heating experiment calibration by resistor heating.

Specifically, 1 mL of gold nanoparticle solution is loaded in a polystyrene cuvette. The solution is heated with a beam of laser at the wavelength of interest (532 nm for GNS, 700 to 850 nm or 1064 nm for GNR, ~200mW output power) from the side and the temperature is recorded by T-type thermocouples located in the corner of the cuvette while a small magnetic stirrer is placed inside the cuvette to obtain a uniform temperature reading. The solution is heated from room temperature until it reaches steady state (i.e. balanced heat gain with loss to environment) which requires roughly 45 min (Fig.2.5B). To accurately determine the amount of absorption and heat generation, we obtained a calibration curve by heating up a 100 Ω resistor with known voltage in the same settings (Fig. 2.5C). The amount of heat generation shows a linear relationship with the

temperature change between the steady temperature and the room temperature of our lab (Q = 16.855ΔT, mW), a condition that heat generation equilibrates with heat loss to the environment. The amount of heat generation from the laser heating is then determined from this calibrated linear relationship. The laser power entering and exiting the sample is measured by a power meter to determine the total laser power loss (P_{laser}). After accounting for the refractive index mismatch, the photothermal efficiency is calculated by

$$\eta_{measure} = \frac{Q}{P_{laser}} \tag{2.1}$$

The measured absorption cross section of the nanoparticle is calculated by

$$C_{abs} = \frac{1}{V}\frac{Q}{NI} = \frac{Q}{NIAd} = \frac{Q}{NP_{avg}d} \tag{2.2}$$

where N is the number density of gold nanoparticles (1/m^3), V is the volume of the solution (1 mL), I is the laser intensity (W/m^2), P_{avg} is the average laser power (W) at which the sample is irradiated, and d is the depth of the solution that laser travels through (i.e. 1 cm for the cuvette). Here the average laser power is taken in the form of the logarithmic mean of the incident and transmitting laser power (P_{avg}=(P_{in}- P_{out})/(ln P_{in}-ln P_{out})) to accurately account for the exponentially decaying laser intensity in the sample.

This cuvette heating system has been validated by reconciling the DDA-predicted and experimentally measured optical properties for GNS and GNR. We systematically compared the measurement and theoretical prediction (DDA by DDSCAT 7.2) for the optical extinction spectrum (UV–Vis), photothermal absorption efficiency (cuvette bulk heating) and absorption cross section

(cuvette bulk heating). For GNS, the mean diameter was used to calculate the optical properties and good agreement with experimental measurement was observed. However, for GNR, particle orientation and the polydispersity (instead of nominal size) are necessary to reconcile the experimental measurement to DDA results (Fig. 2.6). While previous studies have focused on matching the plasmon peak (λ_{max}) between experiment and theory[33,43], the magnitude of absorption, and thus the associated optical properties, is critical to determine the amount of heat generation.

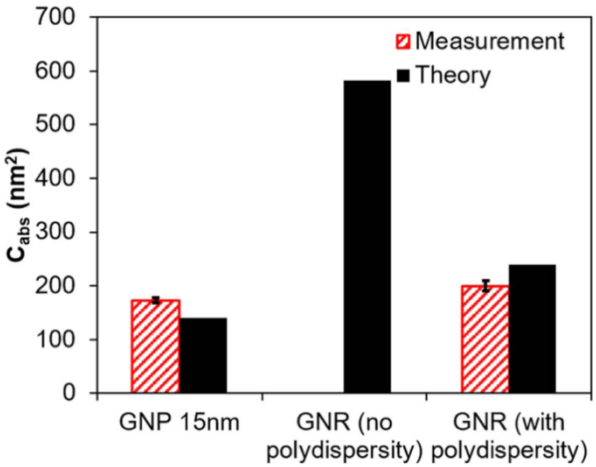

Figure 2.6. Cuvette bulk heating experiment reconcile with DDA prediction for GNS and GNR (when taken polydispersity into consideration). The absorption cross section of a GNS (15 nm) is comparable to a GNR (nominal size D=10.6 nm and L=40 nm).

This work has important implications especially for biomedical applications requiring an accurate estimation of heat generation from laser-gold nanomaterial interactions such as photothermal therapy for cancer[15], nanowarming of cryopreserved biomaterial, and thermal contrast biosensing diagnostics[44]. While previous studies have focused on matching the plasmon peak (λ_{max}) between experiment and theory[33,43], the magnitude of absorption, and thus the associated optical properties, is critical to determine the amount of heat generation. As shown in this work,

the absorption efficiency of GNR can degrade significantly with polydispersity, in contrast to GNS. This is important since GNR are often advocated as more efficient light absorbers than GNS at their tuned plasmon resonances. For instance, it has been suggested that a GNR can absorb 3~5 times more light energy at the plasmon resonance than GNS with the same gold mass (i.e. only changing morphology)[25]; however, based on the present work this enhancement diminishes dramatically when taking into account the effect of polydispersity (ca. 10~20%, Fig. 2.7). Our study speaks to the need for reporting polydispersity along with size and shape in order to accurately estimate the optical properties or the C_{abs} need to be measured and hence heating potential under laser irradiation for GNR. It can be anticipated that polydispersity will also play an important role in photothermal conversion for other increasingly complicated gold nanomaterials (such as shell, cube, stars, horns etc.).[15,45]

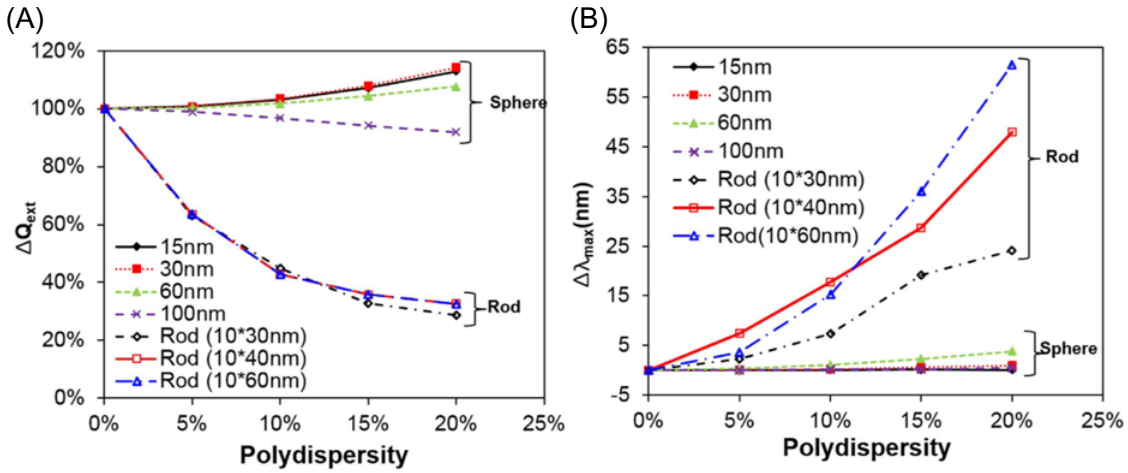

Figure 2.7. (A) Summary of the impact of polydispersity on the optical properties (peak extinction efficiency) of GNS and GNR. Here polydispersity is defined as the standard deviation by the mean. (B) Impact of polydispersity on peak wavelength shift.

Chapter 3 Apply GNP Photothermal Heating in Thermal Contrast Amplification Reader Development Yielding 8-fold Analytical Improvement for Disease Detection with Lateral Flow Assays

The results from this chapter were published in the following citation. The article is reproduced with permission.

- **Wang, Y.**, Qin, Z., Boulware, D. R., Pritt, B. S., Sloan, L. M., González, I. J., Bell, D., Rees-Channer, R.R., Chiodini, P., Chan, W.C. and Bischof, J.C. (2016). "Thermal contrast amplification reader yielding 8-fold analytical improvement for disease detection with lateral flow assays". *Analytical chemistry*, *88*(23), 11774-11782. © 2016 American Chemical Society

ABSTRACT

There is an increasing need for highly sensitive and quantitative diagnostics at the point-of-care. The lateral flow immunoassay (LFA) is one of the most widely used point-of-care diagnostic tests; however, LFAs generally suffers from low sensitivity and lack of quantification. To overcome these limitations, thermal contrast amplification (TCA) is a new method that is based on the laser excitation of gold nanoparticles (GNP), the most commonly used visual signature, to evoke a thermal signature. To facilitate the clinical translation of the TCA technology, we present the development of a TCA reader, a platform technology that significantly improves the limit of detection and provides quantification of disease anti-gens in LFAs. This TCA reader provides enhanced sensitivity over visual detection by human eye or by a colorimetric reader (e.g. BD

VeritorTM System Reader). More specifically, the TCA reader demonstrated up to an 8-fold enhanced analytical sensitivity and quantification among LFAs for: influenza, malaria, and Clostridium difficile. Systematic characterization of the laser, infrared camera, and other components of the reader and their integration into a working reader instrument are de-scribed. The development of the TCA reader enables simple, highly sensitive quantification of LFAs at the point-of-care.

3.1 Introduction

Detecting pathogens rapidly and precisely throughout the globe could control epidemics, eradicate endemic disease, and diagnose patients requiring immediate treatment at the point-of-care (POC), both in resource-rich and resource-limited settings [46–48]. Current technologies allow sensitive and accurate infectious disease detection in a laboratory facility given sufficient time, well trained personnel, and state-of-the-art equipment. For instance, detection through microscopy visualizes organisms *in situ*, making the counting and discrimination of parasites possible, although the variability in skill and time tends to yield a wide variation in the limit of detection [49]. Molecular based diagnostics typically require a contrast agent that is triggered by a specific chemical reaction to a target molecule, such as polymerase chain reaction (PCR) for nucleic acid targets or enzyme linked immunosorbent assays (ELISA) for protein targets. While these methods generally give high sensitivity and specificity, they are often unsuitable for resource-limited POC settings in many developing countries or even in the physician's office in developed countries. This has led to

extensive research efforts to develop molecular tests for POC including the integration of the assays in digital format and microfluidic platforms [8,50,51]. However, further work is warranted to improve the speed and robustness or reduce the complexity of these methods [8,50].

Lateral flow immunoassays (LFAs) are one of the most widely used POC rapid diagnostic tests (RDTs) due to the speed, low cost, and ease-of-use [13,52]. Most LFAs use antibody-labelled gold nanoparticles (GNP) as a contrast agent to provide a red color as an indication of positivity on the test line within 15 min. However, LFAs generally suffer from low sensitivity and lack of quantification [13,52]. Specifically, a low target molecule concentration will lead to insufficient gold to show this color change, resulting in a false negative result. This performance drawback, especially when compared to laboratory-based assays, limit the LFAs ability to be used for infections with low antigen burdens such as early detection (e.g. influenza), and/or efficient triage (e.g. *C. difficile*). Further, even well designed malaria LFAs which can detect at WHO thresholds of 200 parasites/μL, are insufficient for malaria eradication efforts [52,53].

To address the need to improve LFA diagnostic performance one can either focus on LFA design and/or use an LFA reader. In the case of the LFA, one approach is to improve or maximize the contrast physics of the bound analyte in the test line. This can be approached through improved traditional contrast particles (e.g. GNPs) [13,54] or development of non-traditional contrast agents (e.g. fluorescence, magnetic, electrochemical and Raman) as shown in Table 1.1. While promising, these approaches have not yet been translated to clinical use and can come at the expense of speed, cost,

and/or ease of use [55–57] (See Table 1.1). Another way to improve performance is by integration of the LFA with a reader system that leverages contrast such as with fluorescent (QUIDEL® Sofia®) and magnetic LFA platforms. In the case of traditional colorimetric LFAs (i.e. visual) the readers can simplify the readout, reduce human error, and standardize the reading protocol but they unfortunately do not lead to improvement in the analytical sensitivity. The prospect of a new amplification method and the corresponding reader system can lead to improved performance of a wide range of clinically used LFAs with GNP as visual labels.

In this report, we present a single step add-on reader approach based on thermal contrast amplification (TCA) that improves the sensitivity of traditional colorimetric (i.e. gold nanoparticle based) LFAs without any additional modification. This reader is able to amplify the gold colorimetric (i.e. visual) signal by taking advantage of gold nanoparticle (GNP) surface plasmon resonance under laser irradiation [11]. Specifically, the TCA reader matches the laser wavelength to the GNP plasmon resonance peak, thereby generating heat and a temperature rise that can be detected by an infrared detector within the TCA reader. This heat generation is related to the GNP geometry, laser wavelength, and is proportional to GNP concentration and laser intensity [44]. This allows us to sensitively detect and quantify the GNP signal for a known LFA [44,67]

Table 3.1. Samples of LFA Improvement Technologies with Different Contrast Physics and Chemistry

	Detection Method	Contrast Agents	Limit-of-Detection (ng/mL)	Target	Manipulated Particles	Additional Procedure	Readout Device
Commercial LFAs (Current Paper)	**Colorimetric (Visual)**	GNP	1/32*	Influenza A virus	No	No	Optional
		GNP	1	Malaria HRP2	No	No	No
		GNP	1.0625	*C. difficile* GDH	No	No	Optional
	Thermal	GNP	1/256*	Influenza A virus	No	No	Yes
		GNP	0.125	Malaria HRP2	No	No	Yes
		GNP	0.1328	*C. difficile* GDH	No	No	Yes
Other Improvement Technologies (Research LFAs)	**Electrochemical**	Redox e-[58]	0.0001	Troponin I	Yes	No	Yes
	Fluorescence	GNP[59]	2.07	8-Oxo-2'-deoxyguanosine	No	No	Yes
		Quantum dots[60]	0.02	Prostate specific antigen	No	Yes	Yes
		Quantum dots[55]	0.00042	Aflatoxin B1	Yes	No	Yes
		Quantum dots[61]	2	Alpha-fetoprotein	Yes	No	Yes
	Magnetic	MNP[62]	46	Allergen Pa	No	No	Yes
		Platelet MP[63]	0.8	Prostate specific antigen	No	No	Yes
		MNP[64]	15-30	HIV p24 Antigen	No	No	Yes
	Colorimetric (Visual)	GNP[65]	0.2	Human IgG	Yes	Yes	No
		GNP-SiNR[56]	0.01	Rabbit IgG	Yes	No	No
		MNP[66]	1.7	Paraxon Methyl	Yes	No	No
	Raman (SERS)	Au@Ag NP[57]	0.00032	Phenylethanolamine A	Yes	No	Yes

*Dilution rates from positive control swabs; GNP = gold nanoparticle; MNP = magnetic nanoparticle; SiNR = silicon nanorod

To demonstrate the benefits and broad applicability of the TCA reader, we have selected influenza, malaria and *C. difficile* for testing. Importantly, laboratory tests such as microscopy or molecular assays do exist and perform well for these diseases, however they cannot be deployed at the POC[47–49,53]. Additionally, all three of these diseases also have existing GNP based LFAs that, with improved sensitivity of detection at POC, may eventually compete with the more complex, costly or labor-intensive laboratory-based methods. For instance, a recent study on multiple GNP-based influenza LFAs tests showed only 40-69% sensitivity [68]. As influenza occurs yearly in the United States false negative detection places children and older adults at particular risk for substantial morbidity and mortality. Further, malaria LFAs, also known as malaria rapid diagnostic tests (RDTs), are one of the only low-cost assays that can detect malaria at the point-of-care. However, they suffer from low sensitivity (i.e. false negatives) at low *P. falciparum* parasite densities (<100/μL) and poor detection of non-falciparum species[69]. It is an important disease for Africa and part of southeast Asia and can be treated if diagnosed early. In the context of malaria eradication, RDTs need further improvement to detect low-level parasitemia and/or early infection (5-20/μL) [70]. Finally, *C. difficile* is a bacteria that has been reported to infect up to 57% of patients in long-term care facilities [47]. It causes gastrointestinal illness from mild diarrhea to colitis that elongates hospital stays, placing a heavy burden on the health care system estimated at $3.2 billion annually [47]. Here again, a more sensitive LFA to screen the bacteria is urgently needed to efficiently detect and triage patients suffering from *C. difficile*. In summary, improving commercial LFA

sensitivity and performance has the potential to greatly improve the detection and quantification of these diseases at the point-of-care.

3.2 Experimental Section

LFA Samples Preparation. To characterize the TCA reader's ability to detect and quantify the antigen load, 1:2 serial dilutions were prepared with the LFA products.

BD Veritor™ System (two positive control swabs of Flu A and B are included each kit) and a BD Veritor™ System Reader (Becton, Dickinson and Company, Sparks, MD) were purchased. Two flu A positive control swabs were extracted respectively in one RV reagent C vial. The extraction was used as positive control stock. 2100 µL RV Reagent C was added into 700 µL positive control stock solution to make 2800 µL 1:4 control master mix. Six independent 1:2 serial dilution sets were made by adding 430 µL high concentration solution to an unused tube of RV Reagent C (which contained same volume by measurement). LFA samples were prepared by adding 3 drops of the combination through the original tube. BD Veritor™ System Reader and TCA reader tests were made after 10 min. Six negative control samples were prepared by the RV Reagent C alone.

For malaria, First Response® Malaria Ag. pLDH/HRP2 Combo Card Test (Premier Medical Corporation Ltd., Watchung, New Jersey) were purchased from the manufacturer. All malaria LFA samples were prepared by FIND and the London School of Hygiene and Tropical Medicine in several different dilution sets (HRP2 protein – *P. falciparum*. parasite detection target, PvLDH

protein – *P. vivax*. parasite detection target with fresh blood, frozen blood and buffer, and cultured parasites) and sent blind to the University of Minnesota. Lysed blood was used to prepare the dilution set. Lyophilized recombinant HRP2 (Microcoat Biotechnology GmbH, Germany) were re-suspended by distilled water in a glass bottle. The solution was thoroughly mixed by pipetting up and down several times. Long-term stock was made by pipetting HRP2 solution into single-use aliquots (stable polypropylene cryovials) and storing at -80˚C. Further dilutions were made by the following buffer: 2% (w/v) human serum albumin, 7.5% (w/v) trehalose dihydrate, 1mM EDTA, 0.05% Tween 20, and 0.005% sodium azide in 1x PBS (pH=7.4). Malaria negative whole blood was first lysed by freezing at -80˚C for 24 hours and used in the final dilution step. Each dilution was tested by ≥ 3 LFAs. Negative controls (without malaria antigen) were tested 6 times for fresh and frozen blood and 3 times for buffer. Two human evaluators independently interpreted these LFAs in London prior to sending them to Minnesota. The visual reading results and true dilution values were only made available after TCA testing was completed.

RIDA®QUICK Clostridium *difficile* GDH LFAs and RIDA®QUICK Clostridium *difficile* GDH Control were provided by R-Biopharm AG (Eppelheim, Germany). 1:2 serial dilutions were made with 34 ng/mL GDH control and simple saline (0.9% NaCl). Independent dilution sets were made directly from the control solution and tested in the same day since GDH control may lose activity at low concentrations. Intermediate concentrations were made by 1:1 mixture of two adjacent 1:2 serial dilutions. Negative controls used 0.9% NaCl alone. LFAs were interpreted by

one human evaluator and immediately by the TCA reader after the waiting time. Six dilution sets and eight negative controls were tested. A later spot checking with RIDA®QUICK SCAN reader was performed at the visual threshold and one dilution above the visual threshold.

Table 3.2. Comparison of TCA reader and colorimetric readers used in this study. The two commercial readers are optional for the LFA products. The TCA reader has the advantage of providing both quantitative and more sensitive readouts.

Reader	LFA Tested	Contrast	Reads Different LFAs	Result Display	Improved Sensitivity	Quantification	Self-Calibration
BD Veritor™ System Reader	Influenza A	Colorimetric (visual)	Yes	Stand-alone	No	No	Yes
RIDA® QUICK Reader	*C. difficile*	Colorimetric (visual)	Yes	Stand-alone / Computer	No	Yes	Yes
TCA Reader	Influenza A, *C. difficile*, Malaria	Thermal	Yes	Computer	Yes (8-fold)	Yes	Under Development

Limit-of-Detection Calculation Methods. To obtain analytical sensitivity, we assessed limit-of-detection, which is defined by the American Chemical Society as the lowest reliably detectable concentration. There are two common limit-of-detection calculation methods when a calibration curve is already available:

IUPAC method:

$$x_L = \bar{x}_B + ks_B,\ c_L = \frac{ks_B}{m} \tag{3.1}$$

Here, x_L is the smallest measure (signal at limit-of-detection), $\bar{x}_B$ is the mean blank signal, k is a numerical factor chosen in accordance with the confidence level (k=3 for 99.86%, k=2 for 97.7% with normal distribution), s_B is the mean blank sample standard deviation, and m is the slope of the calibration curve and c_L is the limit of detection. In this method, no requirement of sample

size is specified. It is only mentioned that for less than 20 samples, sample standard deviation should be used instead of population standard deviation [71].

CLSI method:

$$x_{LB} = \bar{x}_B + 1.645 s_B,\ x_L = x_{LB} + 1.645 s_L,$$

$$c_L = \frac{1.645\left(s_B + s_L\right)}{m} \tag{3.2}$$

Here, x_{LB} is the signal at limit of blank, s_L is the standard deviation at low concentration. Again, assuming a normal distribution, this calculation will give 95% confidence. The recommended practical number to establish limit-of-detection is 60 samples [72].

Other limit-of-detection calculation methods such as the *modified IUPAC method* introduced by Loock and et al are also available but less used in practice. [73]

$$x_L = \bar{x}_B + t_{\alpha,k-1} s_y,\ c_L = \frac{t_{\alpha,k-1} s_y}{m} \tag{3.3}$$

Here, $\boldsymbol{t_{\alpha,k-1}}$ is the $\boldsymbol{\alpha}$-quantile of Student's *t*-function with *k*-1 degrees of freedom (e.g. $\boldsymbol{\alpha}$=0.01 for 99% confidence and, *k*=2 for 3 repeats), s_y is the standard deviation of the tests 1-5 times higher than the expected limit-of-detection. With the Student's *t*-function, finite numbers of tests are involved in the calculation to get a more conservative result. Namely, a smaller sample size will greatly increase the limit-of-detection (i.e. $t_{0.01,5}$=4.032, $t_{0.01,2}$=9.925). Blank tests and low concentration tests are recommended to be measured at least 7 times, and samples should be prepared independently with different stock solutions [73]. This method is highly sensitive to the

sample size. Since we only have 3 repeats for malaria and 6 for other two LFAs, the calculated limit-of-detections could be problematic. For 99% confidence level, the results for flu A, malaria and *C. diff* GDH are 1:162, 2.535 ng/mL and 0.4369 ng/mL. The benefit of TCA reader is greatly underestimated by this method. The malaria TCA reader limit-of-detection is even higher than the visual threshold (1.0 ng/mL), which does not make sense and hence was not pursued further.

In the case of limit-of-detection calculation, most LFA publications reviewed for this project (see Table 3.1) apply the *IUPAC method* [55,56,58,59,62]. Various other methods are used as well, such as 1) a relaxed *IUPAC* (with the confidence level factor k=2 instead of 3) [63], 2) lowest detectable concentration [74], and 3) other methods where a reference is unspecified (i.e. self-designed methods) [60,66,75]. Importantly, it is also not clear in some of these publications show the dilution tests were designed. For instance, many studies did not mention the number of repeats for dilution and blank samples [60,65,66,74,76,77]. Further, some studies suggested 3 repeats were performed, but it is not clear if these repeats were: 1) independent dilution sets, 2) the same dilution set but applied to multiple LFA tests, or 3) one LFA test with multiple measurements [58,59,63,78]. Other reports made multiple readouts on a single sample [57,79]. Thus, there is a chance of assigning a lower limit-of-detection which may not be completely founded. Finally, while we have done our best to design a fair comparison, the issues noted are a challenge that require acknowledgement.

3.3 Result and Discussion

TCA Reader Development.

A unique advantage of our reader is that it can be easily used for current GNP based LFAs. When inserted into the reader and excited with a laser beam, GNPs on the LFA generate heat to give a thermal signal as shown in Fig. 3.1(A).

$$Q = N \cdot I \cdot C_{abs} \tag{3.4}$$

This heat generation (Q, W/m^3) is the product of GNP concentration (N, GNPs/m^3), GNP absorption cross-section (C_{abs}, m^2), and laser intensity (I, W/m^2). The thermal signal (temperature rise) is collected as the laser passes along the nitrocellulose membrane [44]. As the absorption cross-section and laser intensity remain the same, the thermal signal varies with the amount of GNP present on the test line, which in turn is proportional to the amount of antigen detected.

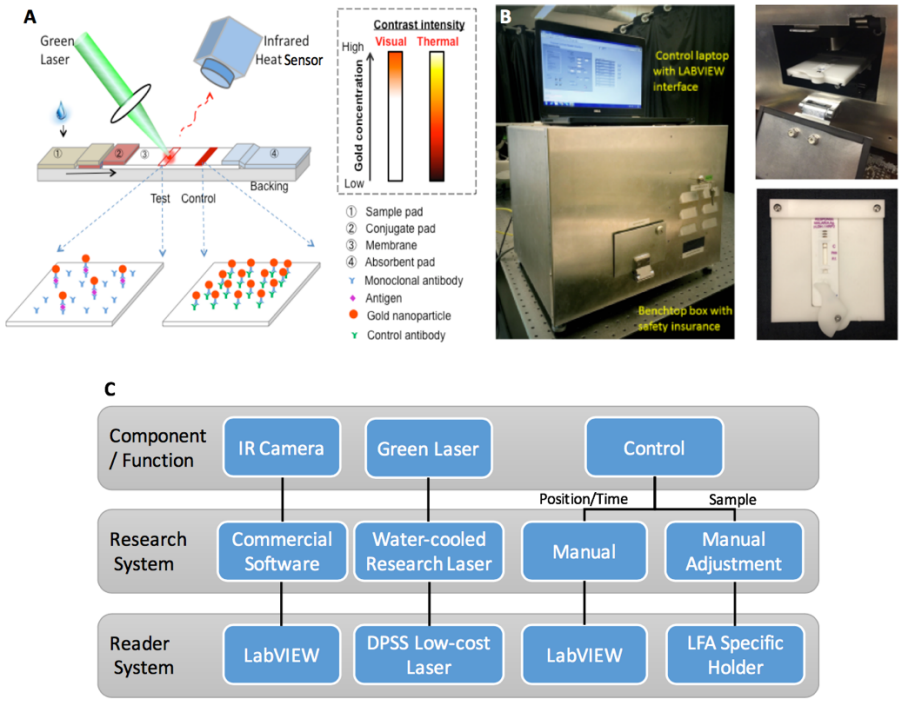

Figure 3.1. TCA reader development. (A) Thermal contrast amplification (TCA) principle and system. Reproduced with permission from ref [44]. Copyright 2012 Wiley. (B) Safety tested, compact TCA reader system (46 cm×34 cm×34 cm size, 11.7 kg weight). (C) Schematic comparison of TCA research system and reader system.

The main components of the TCA technology include an infrared camera and a laser as shown in Fig. 3.1(A). Previously, we used a larger research laser (Spectra-Physics, Millennia Vs), requiring a water-cooling system that is not feasible in many clinical or point-of-care settings. The control of the IR camera, sample feeding/positioning, laser irradiation and timing were manual, subjecting results to human error and repeatability issues [44]. As for the algorithm, three positions were randomly chosen on the LFA test line and the average temperature rise was taken as the thermal signal. Furthermore, in blood samples, hemoglobin occasionally stains the background on such LFAs and absorbs laser energy at 532 nm, thereby creating a background heat signature that

needs to be subtracted. To address these issues, we built a low-cost TCA reader with automatic compact instrumentation, data acquisition and reduction (i.e. algorithm) to increase the reliability, efficiency and portability of this technology for eventual use at point-of-care. This reader is described below.

Instrumentation. For the light source, we require an emitter at 532 nm to excite GNPs in existing LFAs (D~30-40 nm) [44]. This can be achieved by many forms of light sources such as laser or light-emitting diodes (LED) that emit at this wavelength (See Supplemental Information). We carefully characterized the green light sources to select one for the TCA reader. For instance, we studied: 1) 175 mW Aries Series 532 nm Green Portable Laser (Laserglow Technologies, Toronto, Canada); 2) 100 mW 532 nm Laser Pointer Pen (Lazerpoint.com, ShenZhen City Chiang Tech Company, Ltd, China); 3) M530L2-C1 - Green (530 nm) Collimated LED (Thorlabs, Newton, New Jersey, USA); and 4) a low-cost, diode-pumped solid-state (DPSS) laser (LRS-0532-PFM-00200-03, LaserGlow). We compared the beam profile, focused beam size, and output power stability on all light sources (See Fig. 3.8&3.9). The selection criteria included: performance; cost; consistency; and robustness for a laboratory-based working environment. For instance, a smaller beam size may heat more efficiently, but may be harder to reproducibly read within the spatial resolution of the IR camera. Further, a more stable laser gives less background noise, but with a significant rise in cost. We selected the DPSS laser (LRS-0532-PFM-00200-03, LaserGlow) based on these factors (Fig. 3.2&3.9). Additionally, the DPSS laser is air-cooled, providing further versatility. As a final test,

we compared the DPSS laser performance against the original Spectra-Physics, Millennia Vs research laser and were able to verify the equivalency of reading the originally published cohort of cryptococcal LFAs [44]. The results obtained by the two lasers did not differ according to a paired *t*-test (p=0.098) (Fig. 3.2(B)).

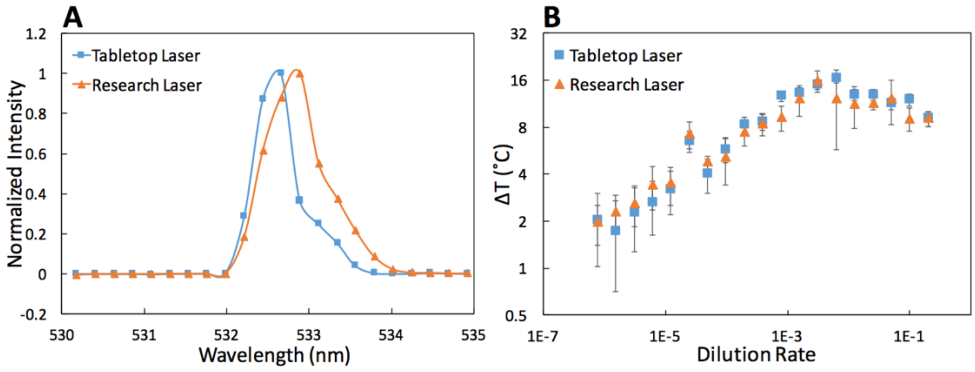

Figure 3.2. The TCA reader low-cost laser is proven equivalent in TCA test outcome to the research laser in previous studies. (A) The spectrum of the reader (tabletop) and the research laser. (B) The TCA thermal results for the *Cryptococcus* antigen LFAs did not differ for the two lasers under the same 10mW output power (paired t-test p=0.098).

Next, we required a component that could read the heat generation from the LFAs. We achieved this through use of an infrared (IR) camera as it provides a non-invasive temperature measurement without compromising the optical excitation and heating of the GNPs within the LFA at 532 nm. After comparing the sensitivity, resolution, stability and interface for data acquisition and analysis of various IR measurement devices. we selected a FLIR ThermoVision™ A325sc camera with 45˚ lens (FLIR, Wilsonville, OR). This camera allowed for full integration of the IR camera into LabVIEW for automatic control, customized real-time data acquisition and data analysis. This is a significant improvement over the previous research system whose data

acquisition and analysis were performed manually and separately in the FLIR ThermaCAM researcher 2.9 software. Using the new software interface, we were able to fully automate the reading and data analysis. Some lower-cost IR sensing products (FLIR E30 IR camera, Melexis 90620 IR sensor array, and Melexis 90614 5˚ FOV IR sensor) were considered undesirable mainly due to lack of spatial resolution or poor computer interface.

Other tabletop reader improvements over the research system include automatic control of a stepper motor and an optical shutter through LabVIEW (Fig. 3.1). Further, LFA-holding cassettes were designed to align LFAs of different size and geometry under the laser for fast and easy thermal reading. This new reader system was first prototyped on an optical breadboard and then integrated into a "box" (Fig. 3.1(B)), for portability and safety (IEC 61010-1, IEC 61326, and ANSI Z136.8-2012), thereby facilitating further field testing in clinics and labs (including use of one box in our Univ. of Minnesota lab, and one box at the Mayo Clinic in Rochester, MN). A set of malaria LFAs with known antigen burden spanning the positive and negative range of both visual and thermal contrast were used to demonstrate equivalency of operation between the prototype and each of the two TCA reader boxes.

Algorithm. The development of the algorithm had two stages: 1) data acquisition and 2) data reduction and display (i.e. result). The data acquisition algorithm is shown in Fig. 3.3. Instead of the temperature rise of a single point on the LFA test line [44], we now use the temperature rise subtracted from background temperature rise to account for noise (e.g. GNP non-specific binding

or blood staining) if present. One complete reading of an LFA interrogates the control line, background, and test line regions, which are reproducibly separated by fixed distances for each manufacturer. Further, by taking more points within the test line, we can obtain a more reproducible measurement than the previous single point method [44]. This becomes particularly important in cases where stronger GNP binding, and therefore signal, is found on the downstream flow direction (i.e. temperature rise curve slightly goes downward from left to right as Fig. 3.3 shows).

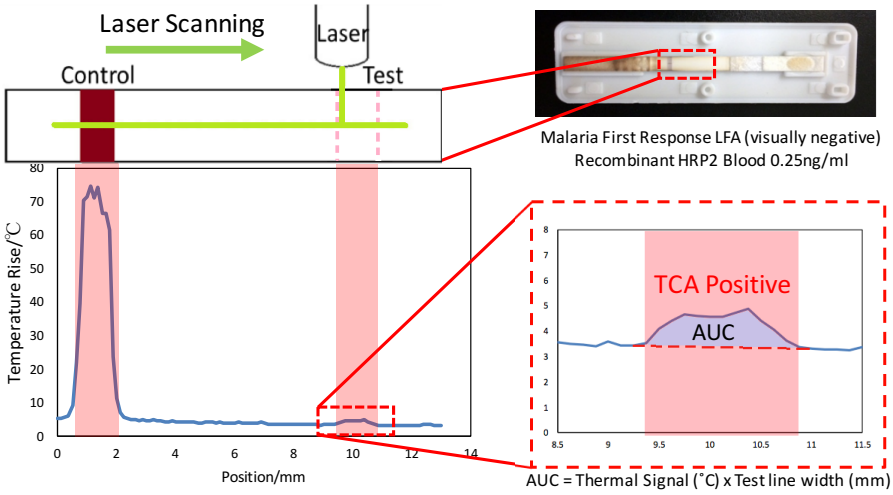

Figure 3.3. TCA reader algorithm for detection and quantification of temperature rise in an LFA. The thermal signal is acquired by an area under the curve (AUC) analysis on the test line position of the LFA. In this proof of principle, a visually-negative malaria First Response® LFA was shown to be a true positive by the TCA reader. The thermal signal score of this LFA is 1.144 ºC compared to 0.179 ˚C (SD=0.053) as the negative control average.

For the data reduction, data plotted as shown in Fig. 3.3 (inset) is subjected to both human evaluators of TCA signal pattern and quantitative area under the curve (AUC) analysis. By trying both methods on the three validation LFAs, we decided the AUC analysis worked better in identifying low target burden signal while giving quantitative results.

TCA Reader Validation.

High quality commercial LFAs for three diseases were selected to perform the validation. We used the BD Veritor™ System (Becton, Dickinson and Company, Sparks, MD) LFAs (5000 $TCID_{50}$/mL limit-of-detection, 78.7% sensitivity and 97.8% specificity by the manufacturer) and influenza A positive control swabs in the package. For malaria, we chose the First Response® Malaria Ag. pLDH/HRP2 Combo Card Test (Premier Medical Corporation Ltd., Watchung, New Jersey), which is among the highest performance malaria LFAs by WHO tests (>200 parasites/μL limit-of-detection, 85% sensitivity and 99.7% specificity) [52]. Two other LFAs were also tested: SD BIOLINE Malaria AG Pf/ Pan (Standard Diagnostics Inc., Gyeonggi-do, South Korea) and ParaHIT – Total Ver. 1.0 (Dipstick) (Span Diagnostics Ltd., Surat, India) (Fig. 3.7 and Table 3.6). Finally, for *C. difficile.* we chose the RIDA®QUICK *Clostridium Difficile* Glutamate Dehydrogenase LFA, which is a high-performance product (R-Biopharm AG, Darmstadt, Germany) (4.6 ng/mL limit-of-detection, 100% sensitivity and 95% specificity by the manufacturer). All LFAs were applied to our TCA reader either right after the test (for influenza and *C. difficile*) or externally prepared and shipped to us by collaborators (for malaria). Both the BD Veritor™ System and RIDA®QUICK come with a portable colorimetric reader for comparison to our TCA reader (Table 3.2).

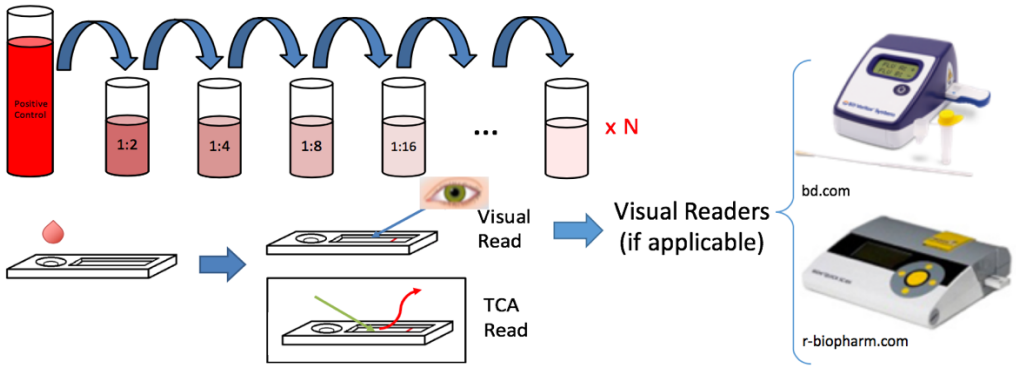

Figure 3.4. Dilution study principle. Commercial LFAs are evaluated with a 1:2 serial dilution of the positive control samples. The LFA is read by eye (visual reader if applicable) and TCA reader. Independent dilution sets are created by the positive control stock solution. Each dilution only applies to one LFA.

Table 3.3. Qualitative (±) Results of TCA Reader vs. Visual Reading (Reader) of Serial Dilution Studies of: (A) BD Veritor Influenza A Control; (B) Malaria Recombinant HRP2 in Blood with First Response LFAs; (C) RIDAQUICK C. difficile Glutamate Dehydrogenase LFAs[a]

A

Influenza A Positive Control Dilution	1:8	1:16	1:32	1:64	1:128	1:256	1:512	1:1024
Visual Reading	+	+	+	1/6[b]	-	-	-	-
BD Veritor Reader	+	+	+	1/6	-	-	-	-
TCA Reader	+	+	+	+	+	+	2/6	-

B

Rec HRP2 (FCQ79) ng/mL	8	4	2	1	0.5	0.25	0.125	0.0625	0.03125	0.0156	0.0078
Visual Reading 1	+	+	+	+	1/3	-	-	-	-	-	-
Visual Reading 2	+	+	+	+	2/3	-	-	-	-	-	-
TCA Reader	+	+	+	+	+	+	+	1/2	1/4	-	-

C

C. difficile Glutamate Dehydrogenase ng/mL	2.125	1.0625	0.5312	0.2656	0.1992[c]	0.1328	0.0996[c]	0.0664
Visual Reading	+	+	-	-	-	-	-	-
RIDA Quick Reader	+	+	-	-	-	-	-	-
TCA Reader	+	+	+	+	+	+	4/6	-

[a] The RIDAQUICK reader showed a detection threshold equal to visual reading on a subset tested. [b] One out of six samples was correctly detected as positive. Same for all the ratios in the following tables. [c] Intermediate dilutions between the 1:2 serial ones.

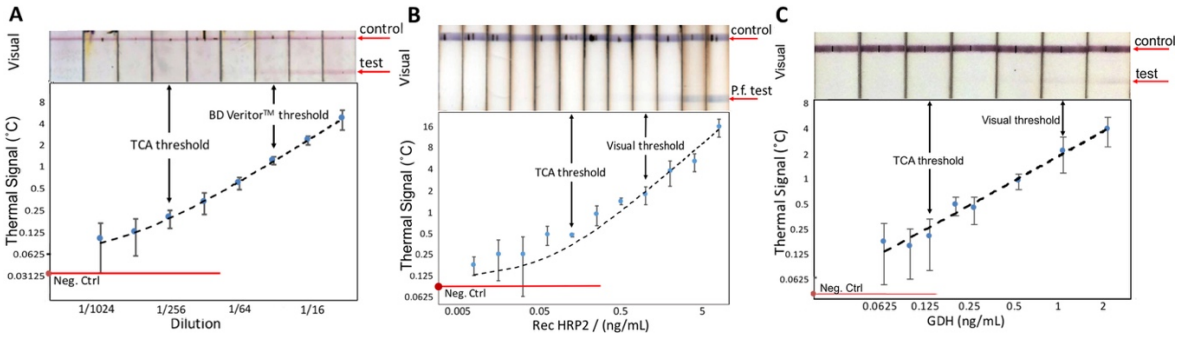

Figure 3.5. Quantitative results of TCA reader vs. visual reading (or reader) of dilution studies of: (A) influenza A positive swabs extraction and LFAs by BD Veritor^{TM}; (B) malaria recombinant HRP2 in blood with First Response® LFAs; (C) *Clostridium difficile* GDH RIDA®QUICK LFAs. The dashed line represents the linear fit of thermal signal to pathogen antigen concentration.

The TCA test results can be interpreted by both qualitative (i.e. human eye evaluation of TCA data) and quantitative (i.e. AUC analysis) methods. The relative position between control line and test line is first measured with visually positive LFAs. Thereafter, the temperature rise curve on the test line can be reproducibly read (i.e. position is fixed) and can be measured and displayed as shown in Fig. 3.3. Here, we directly evaluate the temperature rise at the test line by a graphical readout for a thermal signal peak. Importantly, the actual dilution (i.e. positive at a low dilution or true negative) LFAs are blinded to the thermal contrast reader operators. Next, to evaluate the quantitative performance of TCA, we calculate the thermal signal based on the AUC at the test line position with a MATLAB code (Fig. 3.3). The data close to the test line position are used to fit a base line. AUC is the area integration of the region between the temperature curve and the base line. The thermal signal is then calculated by the AUC divided by test line width. Therefore, the

quantitative thermal signal is related to the total amount of GNPs, and thus the antigen bound to the them, on the test line.

Qualitative Interpretation: The qualitative TCA reader and visual reading results for influenza A, recombinant HRP2 in blood, and *C. difficile* are shown in Table 2 as positive (+) or negative (-). A further 5 groups of malaria qualitative results and similar analyses as HRP2 in blood are available in supporting information (Table 3.5 and Fig. 3.12). For influenza there are 3 visually positive LFA dilutions demonstrating that the BD Veritor™ System reader has the same sensitivity performance as the human eye. Similarly, the RIDA®QUICK reader demonstrated the same detection threshold as visual for *C. difficile*. For all the LFAs, the detection threshold was defined as the lowest concentration that a method could correctly identify all positive results. In this case, the TCA reader showed 8-fold improvement over visual for all 3 studies. Importantly, no false positives were noted in visual or TCA readings for influenza (6 negative controls) or *C. difficile* (8 negative controls), but 2 false positives were noted in the group of 19 negative controls for malaria (Fig. 3.6).

Quantitative Interpretation: The quantitative results for all three LFAs are plotted in Fig. 3.5. Further, representative scanned LFAs are shown above the plots for visualization. The fits show a prominent linear trend (R^2 = 0.999, 0.968, and 0.996 respectively) indicating that the signal correlates to the antigen burden in the sample. Negative control signals are marked with red dots and lines. The qualitative results are noted with arrows.

By comparing the quantified thermal signal with the true dilution concentrations, we were able

to determine the TCA limit-of-detection (LOD). This was achieved by using the two most recognized methods: *IUPAC* and the *CLSI method* for LOD calculation (Table 3.3) [71,72]. Although the results are slightly different, they are both close to the qualitative TCA threshold. These LOD calculations suggest the quantitative analysis of thermal signal is equivalent to human eye thermal peak recognition or even better in identifying low concentration positives (i.e. it distinguishes small fluctuation at thermal test line from blank noise). However, a larger study will be necessary to establish a final quantitative standard for a given LFA [72].

Table 3.4 Calculated Limit-of-Detection (LOD) of Thermal Contrast Amplification (TCA) Results by 3 Methods [a]

Lateral Flow Assay	**Visual Threshold**	**Qualitative TCA Threshold**	**IUPAC Method** (99.86%)	**CLSI Method** (95%)
Influenza A, dilution titer	1:32	1:256	1:441	1:196
Malaria HRP2 in blood, ng/mL	1.0	0.125	0.1210	0.1641
C. difficile GDH, ng/mL	1.0625	0.1328125	0.0395	0.1476

[a]Numbers in brackets are the confidence levels. IUPAC method is broadly applied in other LFA studies.[30] A larger population of independent samples is needed to establish the definitive limit-of- detection.

Independent Validation: One copy of the two tabletop TCA readers was transferred to the Clinical Parasitology laboratory within the Division of Clinical Microbiology at Mayo Clinic. The malaria HRP2 blood dilution study was repeated by Mayo Clinic personnel using exactly the same protocol as described above by the London School. Samples are prepared with the same protocol as FIND. The HRP2 protein was purchased from the same company (Microcoat Biotechnologie GmbH, Bernried am Starnberg See, Germany). 6 repeats were conducted at each concentration while invalid results were excluded. Each sample was tested once with the reader (we tested up to twice in the previous study). One human reader evaluated each LFA. With multiple replicates and

one read for each LFA sample (up to two reads in U of M), a 4- to 8-fold improvement of analytical sensitivity was confirmed (Table 3.5, 6/6 at 4-fold and 4/5 at 8-fold).

Table 3.5 Qualitative results of TCA reader external validation in Mayo Clinic.

HRP2 (ng/mL)	3.2	1.6	0.8	0.4	0.2	0.1
Visual	+	+	2/6	-	-	-
TCA Reader	+	+	+	+	4/5	1/2

Discussion

We present the development and validation of a new TCA reader as a simple add-on for GNP-based LFAs to improve the sensitivity and quantification of disease at point-of-care. We previously reported an order of magnitude improvement in sensitivity of an FDA-approved LFA detecting Cryptococcal antigen (Immy, Inc. Norman, OK), using dilutions of patient derived cerebrospinal fluid [44,67]. However, the previous work was carried out on a research platform (i.e. one that required a large laser on an optical table) with manual control and a simple reading algorithm. This made the operation of the system slow and less repeatable. In addition, the system was expensive and lacked portability and ease-of-use for eventual point-of-care. These issues stimulated the current work in which we developed a compact TCA reader with well-characterized components, alignment, and improved automation and reader algorithm that can be readily manufactured and translated for use in other labs or clinics.

Importantly, we found the cost and performance of the laser and the resolution for the IR detector (camera) to be the most influential parameters for reader functionality and development.

We then added a fully automatic, more efficient control system and algorithm and assembled all of these components into a working prototype for IEC, ANSI and laser safety testing. Proof-of-principle studies with the reader were able to match the earlier *Cryptococcus* LFA results (Fig. 3.2(B)) and demonstrate new 8-fold improvements in the detection threshold for dilutions in influenza A, malaria HRP2, and *C. difficile* commercial LFAs with possibly lower limit-of-detection in other malaria sets with the same LFA (Table 3.6). In short, the TCA reader shows a lower limit-of-detection with quantification than is currently available by visual detection or from colorimetric visual LFA readers. The current cost of the TCA reader is roughly $18,000.- due to the compilation of the components, especially IR camera and laser, into a unified prototype reader system with an industrial partner. These costs are expected to reduce to several thousand dollars when the device is mass produced with reliable, but cheaper components. Once this reader is available for POC use, the only other cost will be the LFA itself. Performance of the reader can be influenced at POC by the environmental temperature. In this study, all tests were conducted in a constant temperature laboratory environment (23°C for both U of M and Mayo Clinic). As the TCA signal is based on the difference of temperature rise between the test line and the background of nitrocellulose membrane, we believe this temperature rise will persist despite environmental change. Nevertheless, careful calibration of the TCA signal change in different environments will be carried out for non-laboratory-based deployments in the future. All reader components are specified to operate in the temperature range of 10-35°C.

To evaluate the ability of the TCA reader to quantify a target molecule, a careful definition of "sensitivity" and "specificity" in the context of limit-of-detection for analytical and clinical use is needed. "Analytical sensitivity" is sometimes used at the assay level as an alternative to limit-of-detection [80]. However, the term also refers to the slope of the calibration curve [71]. "Specificity" for an assay (i.e. analytical specificity) usually refers to the ability to exclusively identify a target molecule rather than similar substances [80]. On the other hand, clinical tests report "diagnostic sensitivity" and "diagnostic specificity" as percentage ratios that correctly detect (true positives detected/ total positives, true negatives detected/ total negatives) samples tested with the target molecule when applied to a population of samples [80]. Importantly, a high-quality assay with high analytical sensitivity and specificity does not guarantee high clinical performance (high diagnostic sensitivity and specificity) [81]. For instance, if the target molecule is at a very low concentration it can be missed in the sampled volume, or if the sample was slightly contaminated, the diagnostic sensitivity or specificity might be poor while the true analytical sensitivity and specificity is still very good [80]. In the case of PCR, both false positives and false negatives remain problematic due to "carry-over" DNA contamination and the relatively small volume permissible for reactions [82]. On the other hand, an assay of lower sensitivity but high specificity can still be of value in "ruling in" or "ruling out" disease in various cases [81].

Although the TCA reader enhances sensitivity and limit-of-detection of LFAs, it is important to evaluate how this improvement affects the diagnostic specificity. Indeed, we recorded several

false positives with thermal contrast that did not occur with visual contrast using the malaria First Response® LFA. In one of the two false positive cases, the blood (i.e. hemoglobin) staining on the nitrocellulose membrane was so dark (Fig. 3.6) that this signal overwhelmed the intrinsic background of the membrane leading to a false positive. The other false positives may have been non-specific binding of GNP in the test line. For malaria LFAs, the poor clearance of hemoglobin is a major source of noise because, like gold, hemoglobin absorbs strongly in the visible range of the laser irradiation (i.e. 532 nm) [11]. If the blood remains on the test line (i.e. is not washed off or otherwise removed) at the end of the test, it can contribute to false positives and even mask the thermal signal of GNPs. This was indeed the case with two other malaria LFAs (SD BIOLINE and ParaHIT – Fig. 3.7, Table 3.7.). With both of these LFAs, the blood staining was so extensive it was not possible to obtain a reproducible signal over background, let alone improvement with TCA. Thus, it is likely that improvement in analytical/ diagnostic sensitivity by a reader may come at the expense of (i.e. decrease in) the diagnostic specificity [83]. As for the TCA reader, the non-specific binding of GNPs on the test line would also be amplified and show a thermal signal (TCA false positive) which was originally invisible by color (visual true negative). Importantly, loss of diagnostic specificity is not automatic and will depend on the LFA design. For instance, we only noted false positives in malaria LFAs and not in Influenza and *C. difficile* likely due to the low intrinsic background (i.e. low non-specific binding and complete lack of blood staining in those LFA membranes).

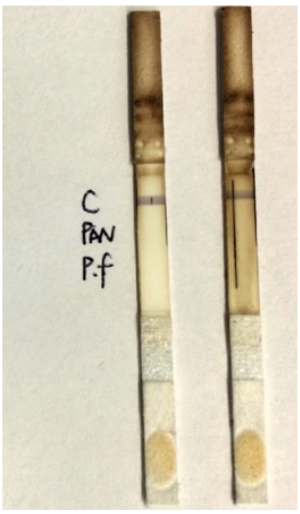

Figure 3.6. Malaria First Response® TCA false positive LFAs. Both of the false positives were tested with blood samples. The LFA on the right has a very dark membrane background. The dark line on the right sample is the burn mark by the laser trace.

Two other malaria LFAs with poor TCA results

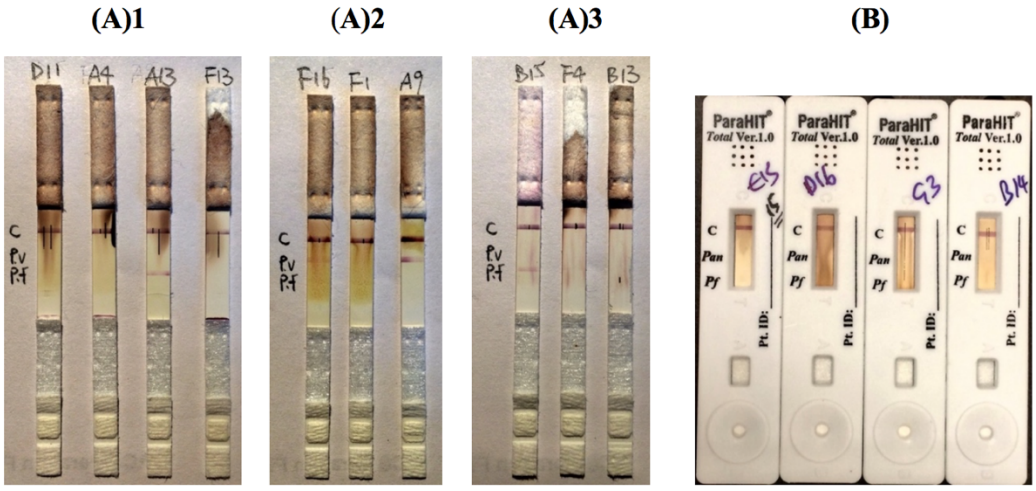

Figure 3.7. Malaria LFAs with poor TCA results.

(A1) SD BIOLINE (Standard Diagnostics Inc.) with blood stain; (A2) appearance changes; (A3) uncleaned GNP traces on the membrane; (B) and Malaria ParaHIT (Span Diagnostics Ltd.). If the nitrocellulose membrane of the LFA is unable to give a thermal clear result after the test, the test line thermal signal will very likely to be masked by blood or gold trace. TCA benefit will be

greatly impaired in such cases. The TCA results seem related to LFA quality. For the three malaria products tested, First Response® showed the most prominent improvement, the SD BIOLINE showed no noticeable improvement, and the background noise covered the signal in ParaHIT.

It is not yet clear what the ultimate limit-of-detection for TCA to detect GNPs on the test line of an LFA will be. Thus, further studies on heat transfer physics, optics, and chemical binding are underway to find this ultimate limit and exploit it in future TCA work. For instance, further opportunities to improve the LFA based on GNP design specifically for TCA reading also exist. Specifically, by switching to a near IR absorbing GNP (i.e. gold nanoshell or gold nanorod), one can enhance the heat signature per GNP at a given laser intensity while simultaneously avoiding excessive background heating at other wavelengths (i.e. hemoglobin). By selecting substrates upon which to perform the LFA antibody-antigen binding that are low absorbing (i.e transparent), the intensity of the laser can be further increased and background noise can be reduced, yielding even more signal-noise ratio (SNR) and enhanced sensitivity. Moreover, any benefits in sensitivity for colorimetric gold-based LFAs that improve the gold-nanoparticle concentration on the LFA test line could be further amplified with our TCA reader. By applying these principles to LFAs and enhancing the stability of TCA reader components, data analysis and reading (i.e. algorithm) methods, we expect a further one order of magnitude improvement over existing TCA LFA reading (already one order of magnitude better than visual) in the future.

In summary, these results have clinical implications for the TCA reader with other LFAs for detection of infectious diseases. As mentioned previously, LFAs are widely used in point-of-care

settings and clinical laboratories for detection of a diverse array of bacterial, viral, fungal and parasitic pathogens. Use of these LFAs has been shown to have a positive impact on patient care by allowing for easily-assessable testing options, encouraging rapid treatment, decreasing unnecessary antibiotic use and facilitating patient triage, particularly for influenza A[84,85], Group A streptococcus[86]. The TCA reader offers additional improvements to this model by increasing the sensitivity of available LFAs, while maintaining a low cost to the patients.

3.4 Additional Characterization and Validation of the TCA Reader

Characterization of TCA reader components

The spectrum width of all the lasers (Full width at half maximum – FWHM~1nm) is narrower than the LED (FWHM~50 nm) (Fig. 3.2 and Fig. 3.8(A)). The spectrum of the laser pointer in Fig. 3.8(B), however, changes over time from green (532 nm) to near infrared peak (from the pump laser) at 810 nm. This is probably due to thermal management issues (i.e. over-heating). Thus, the

spectrum is too broad for the LED, and too unstable for the laser pointer making both choices unsuitable for the TCA reader.

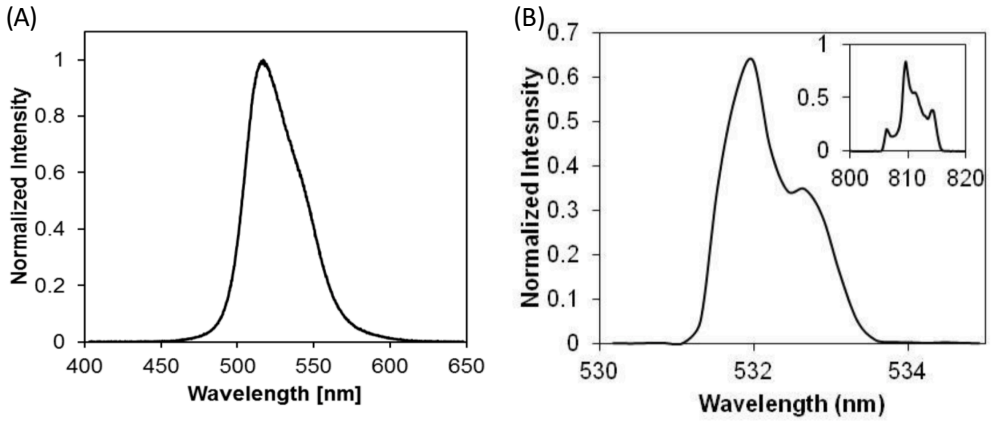

Figure 3.8. Spectrum measurements of the LED and the green laser pointer [87]. (A) The LED is not suitable for TCA because the spectrum width of ~100nm is too wide. (B) The laser pointer's spectrum becomes unstable after continuous running for hours and then yielded an ~810 nm infrared peak (inset) of larger intensity which will reduce the intensity at 532 nm.

Further examining the beam size, the DPSS laser (final choice for TCA reader) can be focused with a plano-convex lens to a size smaller than 100 μm as shown in Fig. 3.8(C). The shape of the beam is close to a Gaussian beam as shown in Fig. 3.8(B). On the other hand, the LED has a large beam size that cannot be focused down to a very small spot (ca. 100 μm). We adapt the knife edge method described in Khosrofian, et al. to obtain the Gaussian beam diameter [88]. A BASIC code (rewritten in MATLAB) was provided by Dr. Bruce Garez for a least square fit. We have further tested the use of LED for thermal contrast and it does not give enough temperature change due to the large beam size (results not shown). The result of this characterization suggests that the DPSS laser satisfies the criteria of our investigation and will be used for the TCA reader.

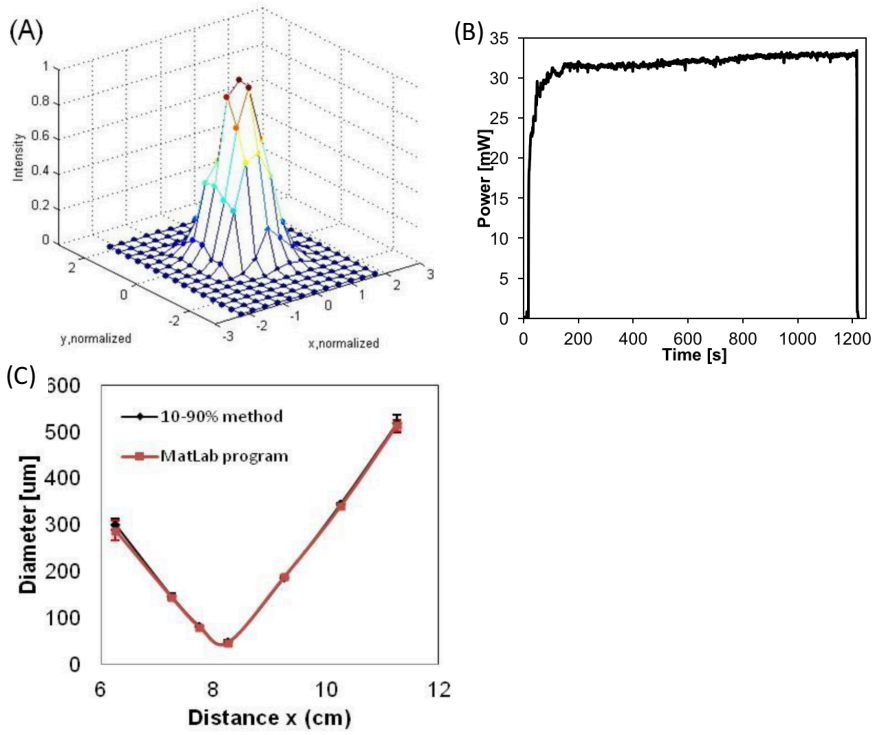

Figure 3.9. Characterization of the TCA reader laser [87]. (A) Beam profile with pinhole setup (diameter = 10 µm). (B) Output power stability in 20 min. (C) Focused beam sized by the knife-edge method (black line for estimated calculation based on Khosrofian's and Garetz's study [89]. The correlation between the curves is $R^2 = 99{,}92\%$ R^2 =99.92%, (N=3).

We also tested some lower-cost IR sensing products (FLIR E30 IR camera, Melexis 90620 IR sensor array, and Melexis 90614 5˚ FOV IR sensor). These tests include a room temperature to 100˚C calibration curve, and a direct comparison to the A325sc camera in a 1 min mimic to the TCA test (Fig. 3.9). However, these items suffered from poor computer interface or lack of spatial resolution and were not deemed appropriate for the TCA reader system.

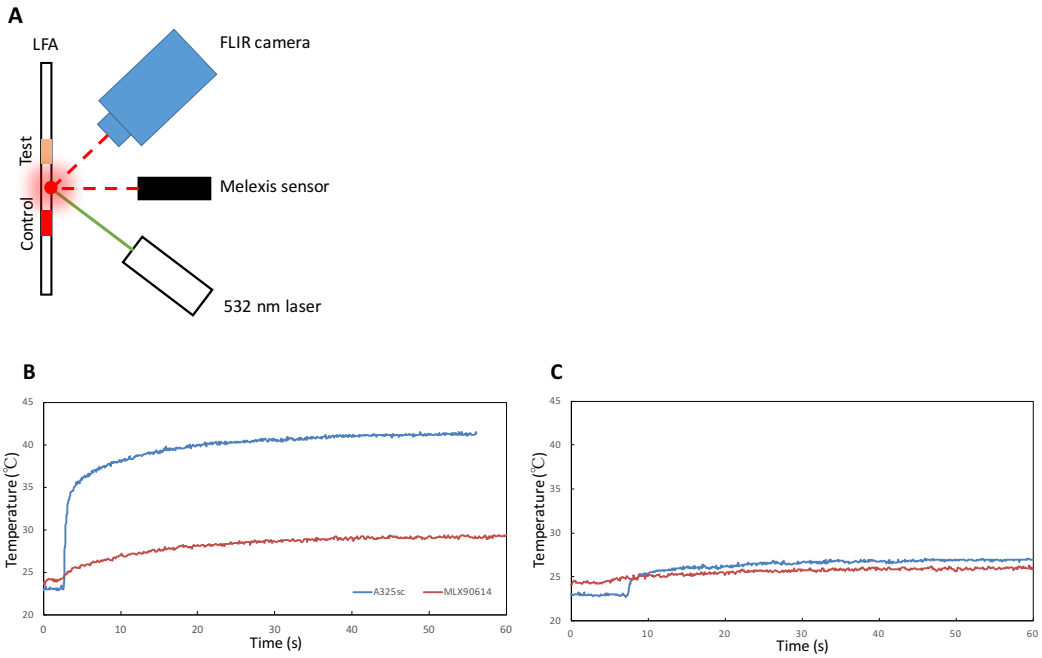

Figure 3.10. Melexis 90614 sensor comparison test results. (A) The sensor was set to minimum focusing size. The laser heated the LFA continuously with 20 mW output power. The sensor and the IR camera recorded at the same time and compared in (B) for LFA control line (maximum TCA signal) and (C) background (minimum) signal. Thus, the Melexis sensor is not appropriate for the TCA reader due to lack of resolution.

Temperature distribution of TCA test

The focused laser beam (about 0.1 mm in diameter) gives a very localized heating for the LFA. This localized heating minimizes the total heat generated during the test. The surroundings of the laser beam are heated by dissipation. We only take the highest temperature rise as the TCA signal. Therefore, it is critical to apply an IR detector of high space resolution since the temperature gradient is large at the laser heating spot (Figure 3.10).

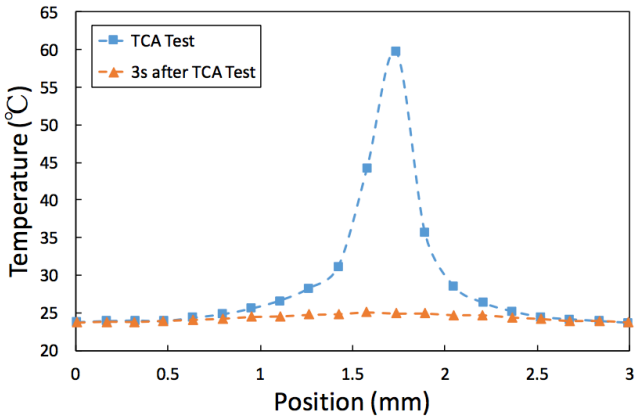

Figure 3.11. The temperature distribution of TCA test on the control line of a *C. Diff* GDH LFA.

Malaria First Response® data in other dilution studies

Four other malaria dilution results are summarized in Table 3.6. The background signals in buffer dilution sets were lower than blood dilution sets because of no hemoglobin non-specific binding. The LFAs showed very large error bars and inconsistent performance in *P. vivax* lactate dehydrogenase (PvLDH) blood study. Also, the linear agreement was relatively poor for this group. In PvLDH buffer dilution, visual threshold was higher than the range tested.

A

Malaria HRP2 (FCQ79), ng/mL	4	1	0.125
Visual reading 1	+	+	-
Visual reading 2	+	+	-
Thermal contrast	+	+	+

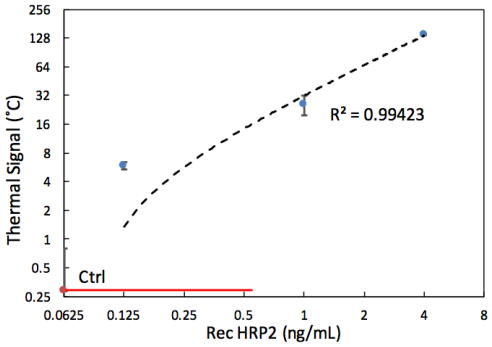

B

P. falciparum culture, parasites/µL	400	200	100	50	30	25	20	10	5	2	1
Visual reading 1	2/3	+	1/3	-	-	-	-	-	-	-	-
Visual reading 2	2/3	2/3	1/3	-	-	-	-	-	-	-	-
Thermal contrast	+	+	+	1/3	+	+	1/3	-	-	-	-

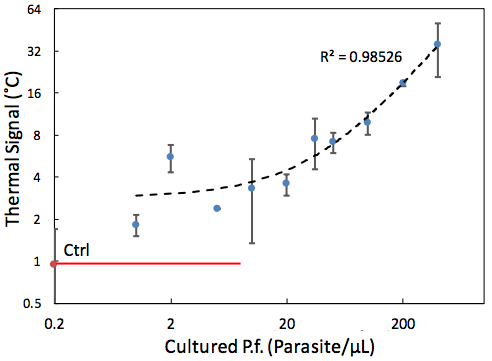

C

PvLDH, ng/mL	360	180	100	50	25	12.5	6.25	3.125	1.5625	0.78125	0.3096
Visual reading 1	1/3	-	-	-	-	-	-	-	-	-	-
Visual reading 2	-	-	-	-	-	-	-	-	-	-	-
Thermal contrast	+	+	+	1/3	1/3	1/3	-	-	1/3	-	1/2

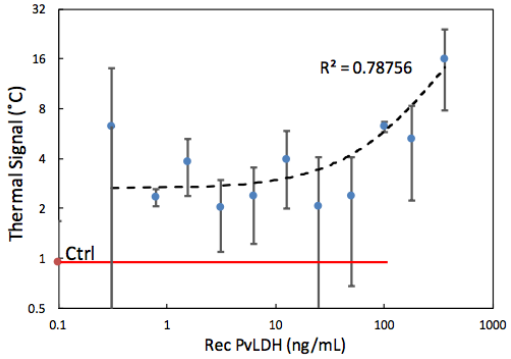

D

PvLDH, ng/mL	180	50	6.25
Visual reading 1	-	-	-
Visual reading 2	-	-	-
Thermal contrast	+	-	-

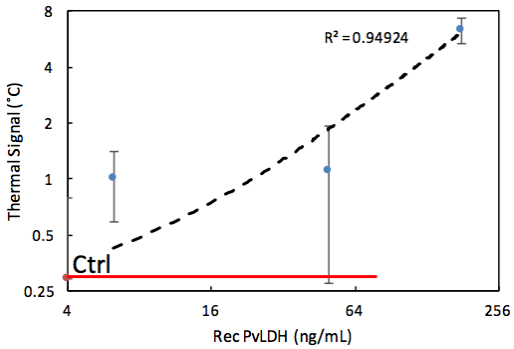

Figure 3.12. Other dilution studies of Malaria First Response® by qualitative and quantitative analyses. (A) recombinant HRP2 in buffer, (B) cultured *P. falciparum* qualitative in parasites/µL, (C) recombinant *P. vivax* lactate dehydrogenase (PvLDH) in blood (D) recombinant PvLDH in buffer.

Table 3.6. Summary of qualitative results of the TCA reader vs. human readers in malaria dilution studies with different targets and solvents with First Response® malaria LFAs. For the last three groups, the visual thresholds are above the highest concentration. In the cultured *P. falciparum* group, TCA showed a ≥16-fold improvement. In PvLDH in blood group, some low concentrations were detected by TCA, possibly due to the inconsistent performance of the LFA.

Malaria Specimen Type	**Visual Threshold** (ng/mL)	**TCA Threshold** (ng/mL)	**Improvement** (fold-change)
HRP2 in blood	1	0.125	8
HRP2 in buffer	1	0.125	8
Cultured *P. falciparum*	>400	25	≥16
PvLDH in blood	>360	100	≥3.6
PvLDH in buffer	>180	180	≥1

Table 3.7 WHO malaria RDT product testing Round 1-5 results of the three malaria LFAs in tested this study.

Product	Manufacturer	Panel detection score				False-positive rates (%)				Total false-positive rate (%)	
		200 parasites/µL		2000 or 5000 parasites/µL		200 parasites/µL		2000 or 5000 parasites/µL		Clean-negative samples	Invalid Rate (%)
		Pf	Pv	Pf	Pv	Pf Non-Pf	Pv Pf	Pf Non-Pf	Pv Pf	False-positive Plasmodium spp. infection	
First Response® Malaria Ag.pLDH/HRP2 Combo Card Test	Premier Medical Corporation Ltd.	85.0	74.3	100.0	100.0	0.3	0.0	0.0	0.0	0.0	0.0
SD BIOLINE Malaria AG Pf/ Pan	Standard Diagnostics Inc.	90.8	94.1	100.0	100.0	1.0 (385)	0.0 (130)	0.0 (195)	0.0 (67)	1.3 (226)	2.8
ParaHIT – Total Ver. 1.0 (Dipstick)	Span Diagnostics Ltd.	76.5	61.8	100.0	94.1	0.8	0.0	0.0	1.5	0.0	0.0

Chapter 4 Improve Clinical Group A *Streptococcus* Detection on Rapid Diagnostic Test Assays with Thermal Contrast Amplification Reader

This study has been prepared as a journal article and been submitted as:

- **Wang. Y.**, Louwagie. E., Larkin. D., Sankey. S., Boulware. D. R., & Bischof. J. C., "Improve Clinical Group A *Streptococcus* Detection on Rapid Diagnostic Test Assays with Thermal Contrast Amplification Reader". *Analytical Method.* (In review)

ABSTRACT

Group A *streptococcus* causes significant health care costs and burdens. In the form of a mild infection, streptococcal pharyngitis is difficult to diagnose and manage while having the potential to progress to life-threatening invasive infections. Though this calls for timely and accurate diagnosis, the unsatisfactory performance of the rapid diagnostic tests frequently requires follow-up high-sensitivity confirmatory testing causing additional time and cost. Improving rapid detection sensitivity will lead to more timely and accurate diagnosis. As shown in previous work, the robust, easy-to-use thermal contrast amplification reader improves traditional rapid diagnostic test strip sensitivity 8-fold. We present here a clinical study to demonstrate the impact of thermal contrast amplification reader on clinical strep throat detection. The result shows that the TCA reader identifies over 50% clinical false negative samples. In application, the reader could significantly reduce the need for confirmatory strep throat tests in a primary care setting.

4.1 Introduction

Group A *streptococcus* (*Streptococcus pyogenes*, GAS) is a severe health threat in the US and worldwide. Currently, at least 18.1 million people worldwide experience the consequences of serious GAS diseases (e.g. invasive GAS, acute rheumatic fever, and acute glomerulonephritis, among many others) along with another 1.7 million new cases and 500,000 deaths globally each year.[90] The number of mild GAS diseases (e.g. streptococcal pharyngitis or "strep throat" and impetigo) is 700 million each year with 650,000 that progress to severe invasive infections.[91] GAS is responsible for 5-36% of pharyngitis in the US[92] and is remarkably difficult to manage due to its highly contagious nature and nonspecific clinical features[93], leading to significant health care costs (~$493 million annually).[94] Therefore, more timely and accurate diagnosis of GAS infection could significantly lower health care costs through prompter treatment, reduced transmission, and minimized complications.

The current strep throat rapid diagnostic test (RDT) used in clinical practice suffers from a lack of speed and accuracy. The RDT, which is usually performed with a throat swab in a point-of-care setting,[95] saves clinical staff time and allows for treatment to be prescribed at the point of care.[96] The strep throat RDTs are lateral flow immunoassays (LFA), which are commonly used in rapid detection tests because they are fast, inexpensive, and easy-to-use.[13,96] When the RDT is visually positive (Fig. 4.1&4.2(A)), the health care provider can then quickly and reliably provide the patient with appropriate antibiotics or other treatment. Unfortunately, due to low RDT

sensitivity (only 70%-90%), there are often patients whose RDT is a visually false negative, [97–99] The RDTs for these patients lead to delayed or missed treatment, added cost and possible unnecessary exposure of others to potential infection from these 10-30% of all GAS-positive patients.[97–99]

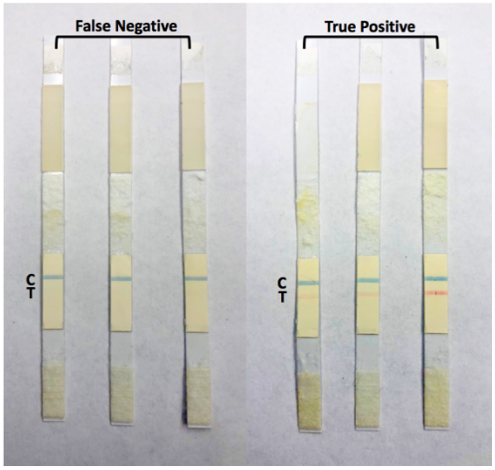

Figure 4.1. Randomly picked clinical Quidel QuickVue Strep A Dipstick Test LFAs from the sample stock. Parts of the LFA were removed except the membrane. Clinically, very faint color test lines are considered as positive. Only blank test lines are considered as negative.

Visually negative RDTs lead to a further confirmatory blood agar plate (BAP) culture or PCR testing, usually performed on a second separate throat swab collected at the time of initial testing.[100] Throat culture is considered the "gold standard" for diagnosing strep throat with clinical sensitivity ≥ 90% and a negligible false negative rate.[101] GAS DNA probe assay is another clinical confirmatory test method, considered to have similar performance as throat culture.[102,103] Nevertheless, confirmatory cultures require an 18 – 48 hour turn around, transport of patient samples, and extra labor from a skilled professional.[104] By improving the sensitivity of strep throat

RDTs to reduce false negatives, it may be possible to significantly reduce – or even obviate – the need for such confirmatory testing. Recently, some innovative strep throat detection methods with higher sensitivity and semi-quantification have emerged, such as mass spectrometry-based lipid detection.[105] However, none of these approaches have been commercialized yet.

To improve the sensitivity of RDT strep throat detection, a novel thermal contrast amplification (TCA) reader is proposed here. The TCA reader is a single-step add-on to traditional LFAs that relies on a higher sensitivity thermal signature (Fig.4.2) instead of the traditional visual signal. In LFAs, antibody-labeled gold nanoparticles (GNPs) are typically used to provide a visual signal. These GNPs produce a red or purple test line to indicate a positive test result when bound to the biomarker. Under green laser (532nm) irradiation by the TCA reader, GNPs will generate heat due to surface plasmon resonance.[44,106] This heat can be detected by an IR camera and analyzed to give a thermal signature. In its use to date, the TCA reader has shown 8-fold improvement for disease detection with pure, laboratory prepared samples on LFAs for malaria, influenza A/B, and *C. difficile* along with demonstrating 92% accuracy in quantifying cryptococcal meningitis titers.[67,106]

To demonstrate the impact of this TCA reading of clinical strep throat RDTs, we report here on a collaboration with a local primary care clinic (HealthEast Grand Avenue Clinic, St. Paul, MN). We show that the TCA reader can identify over 50% of the clinical "false negative" strep throat RDTs (QuickVue Dipstick Strep A Test, 92% sensitivity by the company) in a clinical cohort of

178 LFAs. We also show that we improved the analytical sensitivity of strep throat RDT by 4- to 8-fold based on our positive control dilution study. Our results suggest that, if placed in a primary care setting, the TCA reader will provide rapid and more accurate detection results, thereby minimizing the need for confirmatory tests. In the future, confirmatory testing may possibly be eliminated with new TCA based LFAs under development.[107]

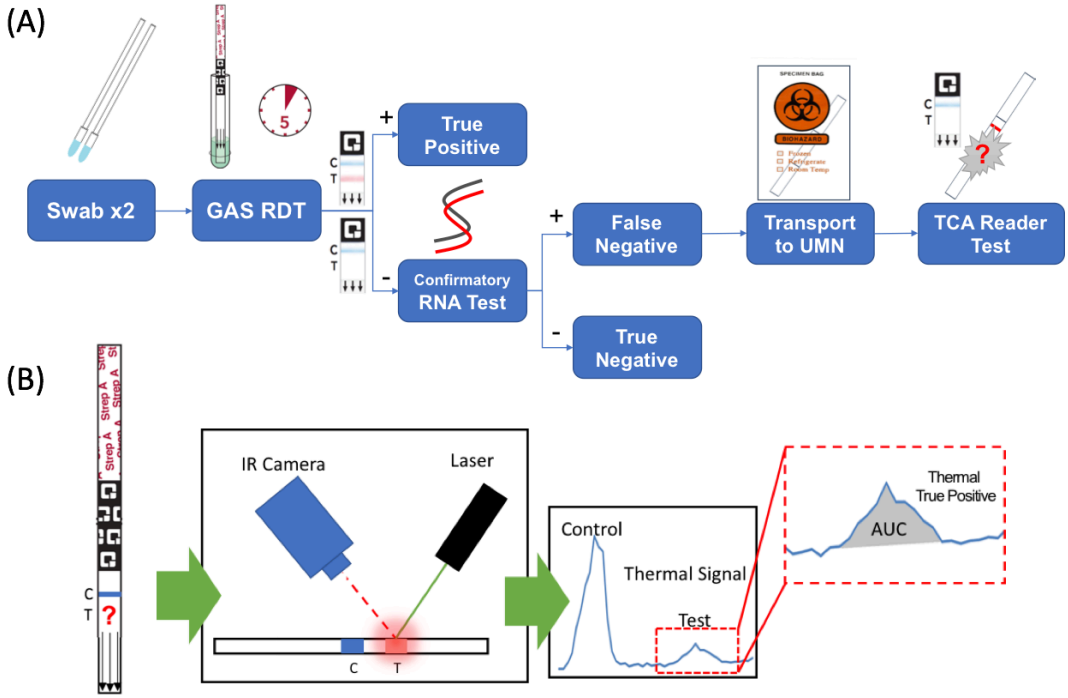

Figure 4.2. (A) Scheme flow chart of thermal contrast amplification reader clinical study on GAS RDT. RDT samples are collected and tested at a primary care clinic and transferred to our lab. (B) Thermal contrast amplification reader principle. In the reader, a thermal signal curve is generated with a peak revealing whether the test line is true positive.

4.2 Results and Discussion

GAS Clinical Study. During the 6-month study, in total 9335 strep RDTs and 6698 confirmatory tests were performed in our collaborator clinics. During this time, 268 false negative RDT results were identified. Of these, 88 were collected by a trained clinical assistant and transferred to the University of Minnesota for TCA testing. The thermal signal of all LFAs in this study (including true negatives and false negatives) are plotted in Fig. 4.3 where each point marks an individual sample. The dashed lines represent the detection threshold, with the false negatives above this line those that were detected by the TCA reader. The x-axis denotes the numerical identifier for each sample in the order of collection time. The TCA reader detected 45 (51.1%, 99.86% confidence level) of the known false negatives out of 88 samples tested. By looking at the statistical analysis from Table 4.1, we conclude that the TCA reader significantly improves the sensitivity of the RDT (TPR = 0.51, FPR = 0.06, compared to perfect detection TPR = 1, FPR = 0).

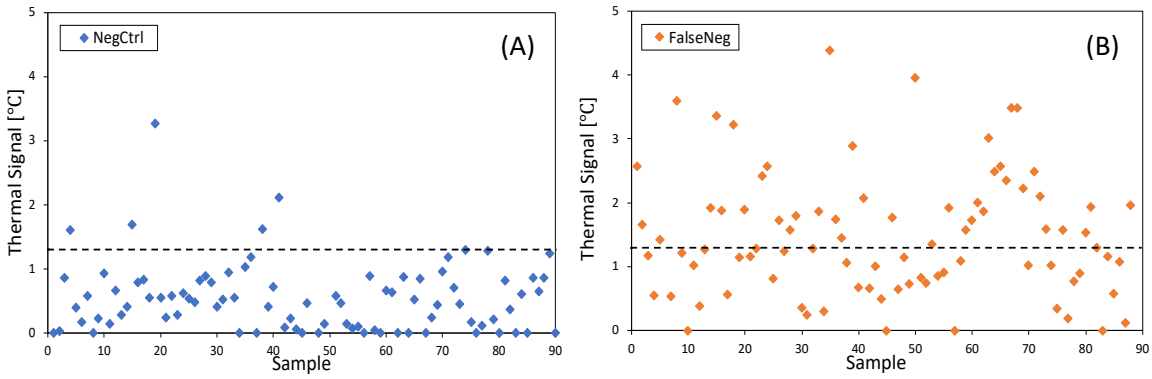

Figure 4.3. Clinical strep A LFAs are evaluated again by TCA reader. Pathogen culture results are taken as golden standard. (A) Thermal signal for 90 true negative clinical samples. 5 of them turn to false positive by TCA. (B) Thermal signal for 88 false negative clinical samples. TCA gets true positive results in 45 of them (51.1%).

Table 4.1. Clinical strep RDT data statistics

TP=45	FN=43	88	TPR = 0.51
FP=5	TN=85	90	FPR = 0.06
			PPV = 0.90
			F_1 = 0.65
50	128	178	ACC = 0.73

GAS Analytical Calibration. We then quantified how much the TCA reader improves the analytical sensitivity of strep throat RDT for the 51.1% benefits in clinical sensitivity. A calibration study was conducted with strep positive control solution in six independent dilution sets (Fig.4.4). The visual threshold in the calibration study is higher than 1/16 dilution positive control (5 positive results out of 6 dilution sets). The dry curve reflects the RDT condition of the clinical study (detection threshold 1/53). The wet curve reflects condition of real clinical use where RDT samples were read by the TCA reader directly after visual evaluation (detection threshold 1/66). The higher TCA improvement in wet over dry conditions is likely due to lower noise by the RDT when read immediately after visual evaluation. It can be concluded that the 51.1% improvement in clinical sensitivity is achieved by improving analytical sensitivity for 4- to 8-fold.

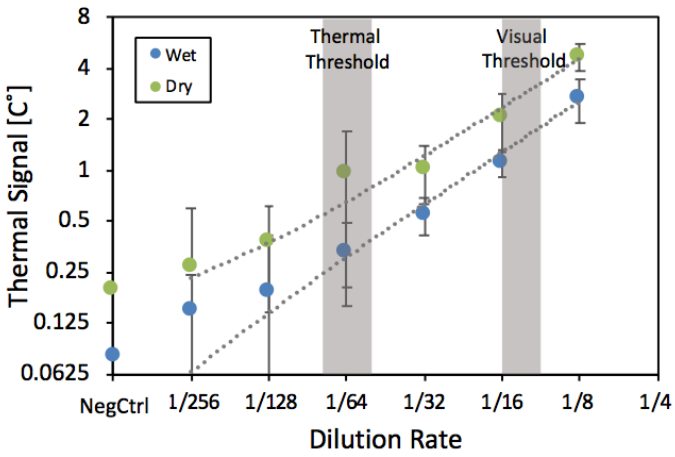

Figure 4.4. Dilution study shows that the TCA reader improves the analytical sensitivity of strep A LFA by 4- to 8-fold. Positive control solution in the LFA package was used as original stock.

Discussion. We have shown that the TCA reader improves the clinical sensitivity of strep throat in RDTs by detecting >50% of the clinically false negatives by visual reading. This was done by setting up a detection threshold with true negative samples and applying it to visually false negative samples. For this specific commercial RDT, we improved the sensitivity from 92% to 96% while only adding one reading step. This is quite close to the rate of agreement between DNA direct test and throat culture.[103] Although the device is highly automated and the detection threshold is made beforehand, we will note that the TCA reader operator knew the positive/negative status of the LFAs she handled. This is the only possible source of bias in the study.

The TCA reader has the potential to save time and cost and lower complications in strep throat diagnosis. However, we did observe some false positives during the testing of true negative samples, especially early in the study (Fig. 4.3(A)). We believe that this can be attributed to sample preparation. For example, GNPs can wick back to the test line after the test by the faster evaporation

occurring at the membrane. This then would artificially enrich the unbound GNP concentration, producing a visually red line during drying. A solution we implemented was the removal of all pads (sample, conjugation, and absorption) from the LFA, leaving only the membrane attached to the backing material after point-of-care visual evaluation by lab staff. We have verified this assumption by leaving all the pads intact, running LFAs with negative swabs, and testing LFAs fresh and 3 days later. Although the fresh TCA signal is quite faint, the signal of some samples increased remarkably during the second dry test and false positives were observed. We examined the effects of LFA pads on the TCA detection result by 20 GAS negative fresh swabs. QuickVue package insert protocols were applied. After the visual evaluation, all the components were kept attached unlike the clinical samples in our study. Back flow from the pads was expected due to faster evaporation on the membrane and capillary force. The wet TCA test was performed immediately after visual evaluation and the dry TCA test was done 3 days later like the calibration curve study. We can see from Fig. 4.5 that some of the thermal signals increased significantly, which was not observed in the calibration curve study. Two samples showed false positive TCA results. It can be concluded that backflow should be eliminated when running TCA reader and fresh study should be preferred.

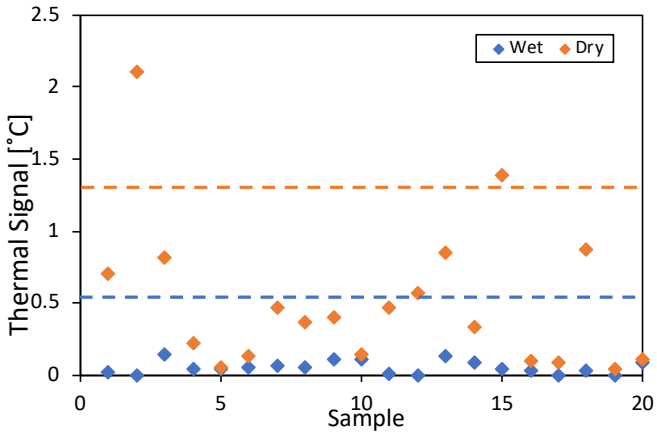

Figure 4.5. Wet and dry GAS RDTs with backflow shows significant change in TCA results. Dash lines are detection thresholds in both conditions.

In the future, further improvements on strep throat RDTs by the TCA reader are expected. We have shown that by modifying the flow pattern and GNP geometries in an LFA, the TCA reader could achieve up to 250 fold improvement in analytical sensitivity.[107] Also, we intend to field-test a TCA reader in a clinical setting, with point-of-care samples for strep throat and possibly other diseases.

4.3 Methods

Clinical RDT Samples. All clinical sample collection followed standard strep throat diagnosis practices (by Lippincot). In addition, no eligibility criteria applied to the patients who received a strep throat RDT test during the study period. All the samples handled by the trained clinical laboratory staff were included in the study. Two swabs were obtained simultaneously from each

patient. One swab was taken for a clinical strep RDT (QuickVue Dipstick Strep A Test, Quidel, San Diego, CA). When the RDT showed a negative result, the sample, conjugation and absorption pads were removed to stop any further reaction, thereby settling the result. The RDT was then placed in a biohazard bag (Fig. 4.6). A subsequent high-sensitivity confirmatory test (Hologic GasDirect test) was performed with culture swab (Port-A-Cul tube) to establish true positives. Finally, all patient-specific information was removed from the sample and bag, leaving only a numerical identifier. The false negative samples for further testing were collected by the lab staff at HealthEast's Grand Avenue and Maplewood Clinics and transferred for TCA reader testing in the Bischof lab at the University of Minnesota–Twin Cities roughly once a week in a rolling fashion. True negative RDT samples for algorithm training and building the TCA threshold showed in Fig.4.3(A) were randomly selected.

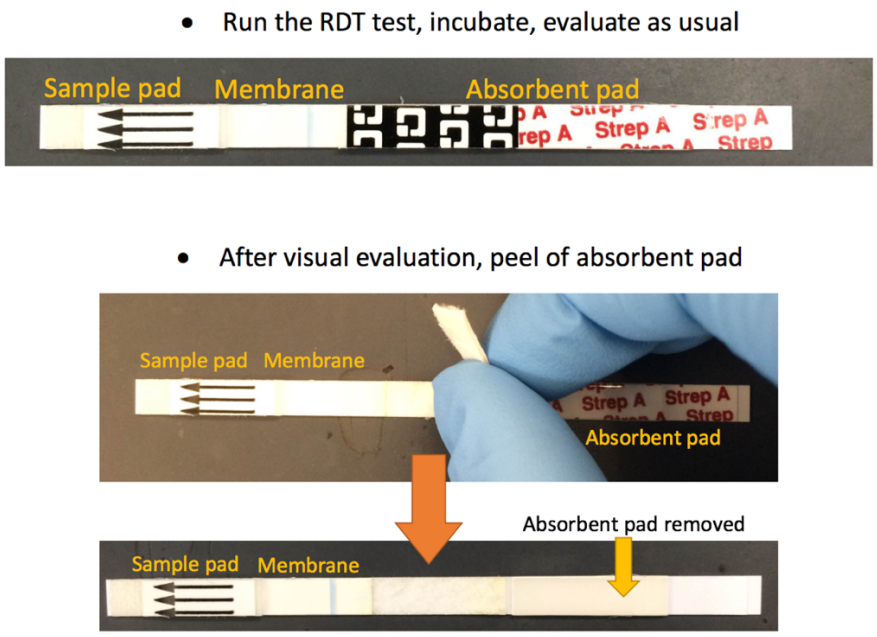

- Remove sample pad, including the top layer and conjugate pad (not visible from top)

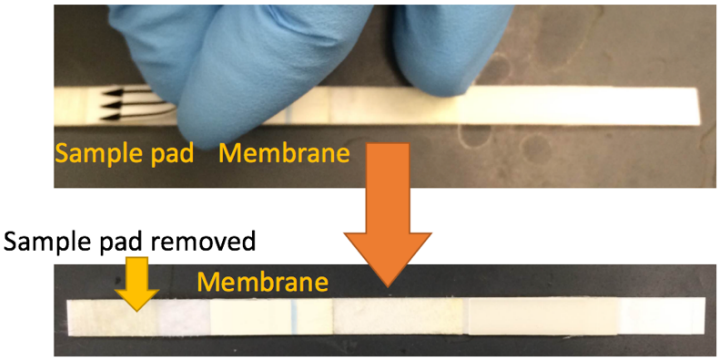

- Store in a plastic bag and document

Figure 4.6. Strep LFA TCA study sample handling steps.

Lab Control Sample Dilution Set. To characterize the TCA reader's ability to detect and quantify the strep antigen load, 1:2 serial dilutions were prepared with the QuickVue positive control liquid (heat-inactivated group A Streptococcus, diluted in a buffer solution containing 0.02% sodium azide) which is shipped as a control with the RDTs. Since the instructions suggest "one free falling droplet" of this control solution per LFA, we set the volume of each droplet to be 50 µL by pipette and used this volume during a control dilution test with the LFA. Specifically, 1 mL positive control liquid was taken as control stock solution. Six independent 1:2 serial dilution sets were then

made by diluting 100 µL stock with normal saline (CLSI requirement).[72] LFAs were prepared according to the QuickVue package insert procedure with 50 µL of the dilutions. TCA reader wet tests were made immediately after the 5 min incubation and visual evaluation. The TCA dry tests were made 3 days after the wet tests.

TCA Test. All the clinical strep throat LFA TCA tests were performed by a trained operator. The reader tested each sample once at the same position on the strip. The test line position was established by calibrating distance from the control line in all cases. The testing and data processing algorithms were the same for each sample. 20 clinical true negative samples were randomly selected by the clinical Lab staff and used to train the TCA algorithm to identify a thermal detection threshold. Details of the TCA reader, protocols and threshold have been described in detail in previously published work.[106] Briefly, the reader has a laser which scans across the whole testing area of the LFA membrane. The resulting thermal signature is then read by an infrared camera. This signature difference between the background and the test line is then subtracted and plotted as shown in Fig. 4.2. A reading is considered positive when above the detection threshold. This threshold is determined by the average signal plus three times the standard deviation of 20 negative control samples (99.86% confidence level).[71] All clinical strep throat RDT samples tested are compared to this threshold as shown in Fig. 4.3. All the clinical samples were tested within a week of arriving in the lab.

Chapter 5 Characterize and Improve Thermal Contrast Amplification Reader for Parameters, Components and Algorithm

GNP-laden lateral flow assay membranes, as the critical components in an LFA, were characterized for optical properties. Then their photothermal heating with a TCA reader predicted by the optical-thermal model was compared with experimental data for validation. This model was then applied to a real LFA. We were able to better understand the TCA technology and optimize the reader configuration, instrumentation, and algorithm for a future generation device.

5.1 Measure and Model of GNP-Laden LFA Membrane

GNP-laden LFA membrane sample preparation and characterization. The typical functioning part geometry of LFA products on the market is usually a small strip—5 to 10 mm wide and 50 to 100 mm long. The structure of an LFA is shown in Fig. 5.1. During a TCA test, the reader irradiates a laser beam on the test line of the membrane to generate a thermal signal for IR camera's capture. If we look closely on the LFA membrane, a three-layer format will be identified. The top layer of LFA is a nitrocellulose membrane, the most important part where capillary flow of samples and antibody-antigen reaction happen. Because the nitrocellulose membrane is highly porous, fragile and thin, a membrane backing layer is necessary to hold it in place. Additionally, a thicker assay

backing layer is beneath the membrane for the lay-up of all the different components. This LFA backing layer is thicker and more rigid polystyrene material for most products.

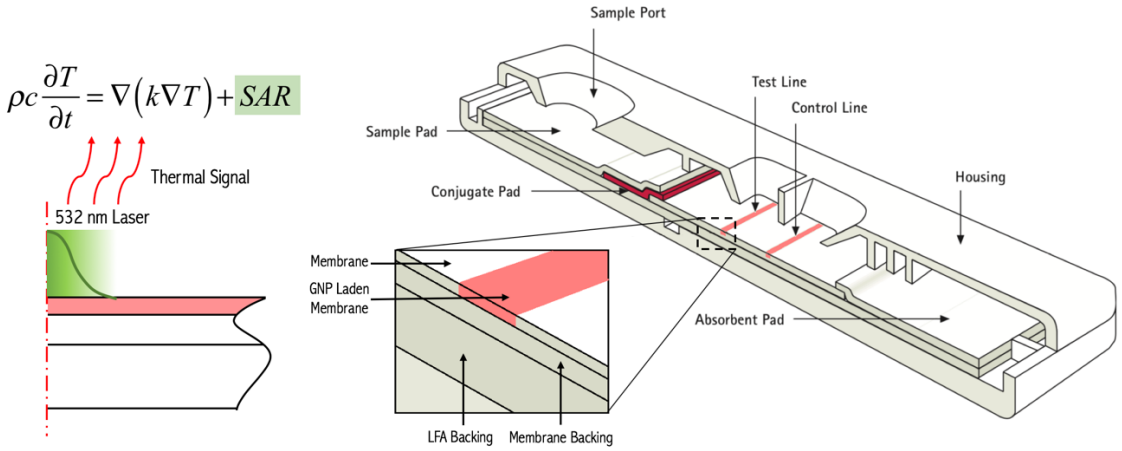

Figure 5.1. Schematic view of a commercial LFA structure and the effect of TCA on the layered structure.

Because of the small geometry of the GNP-laden test line (1 to 1.5 mm test line width), it cannot fit into an integrating sphere spectrophotometer. Therefore, we applied a modified jet ink printer to load the GNPs uniformly like a real test line. This printing method also controls the concentration of GNPs applied, enabling quantitative analysis of the photothermal effect. PVP was added to the GNP solution 'ink' adjusting the liquid viscosity and thus avoiding any non-uniformity caused during the evaporation drying process. 30 nm diameter gold nanospheres were fabricated and used in this study according to modified Frens method that had been described in detail in our previous study.[108] We selected this GNS for similar particles that are commonly used in commercial products, such as LFA for cryptococcal meningitis and human hCG detection. The printed sample geometry is shown in Fig. 5.2. As a commonly used component in research and commercial

products, Hi-Flow™ Plus HF135 membrane (EMD Millipore, Germany) was used. The assay backing layer is not included the sample. We printed 0.3 nM and 0.15 nM GNP (shown as 1x and 2x samples in Fig. 5.2(B)) that are similar to relatively high concentration target concentration results in a real LFA.

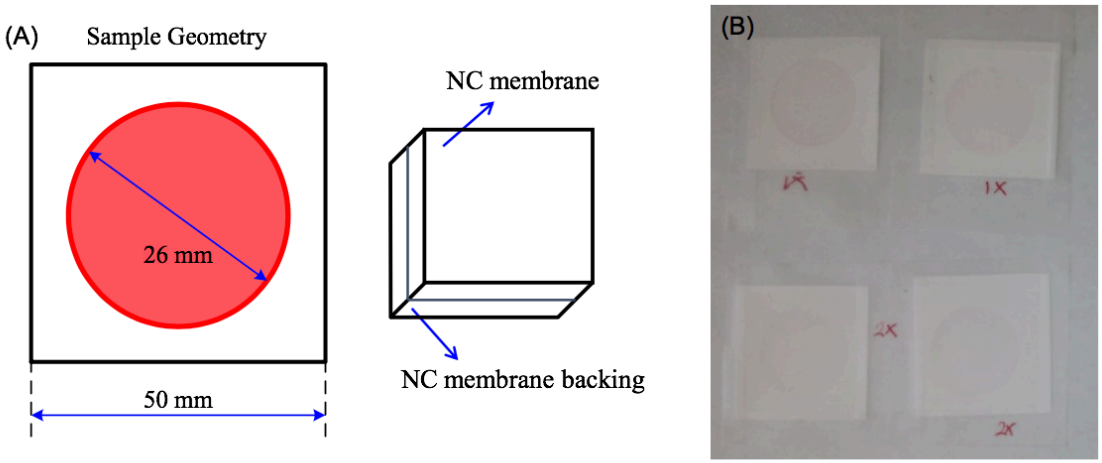

Figure 5.2. Printed GNP-laden membrane sample (A) geometries and (B) picture of real samples.

GNP-laden sample thickness measurement. We applied electronic calipers (Mitutoyo, Japan) to obtain the thickness of the samples for optical measurement and Monte Carlo modeling. Before the measurement, the calipers were calibrated by contact tests with the platform. And set that value to zero for the whole test. Three different positions on a sample was measured and averaged as the sample thickness (center, top right corner, bottom left corner). The whole membrane was first measured for the total thickness of nitrocellulose layer and membrane backing layer. Then the nitrocellulose was scraped off and washed by acetone to remove any residuals. The remaining membrane layer was measured again in the same way. The thickness of nitrocellulose layer was

calculated by subtracting the backing from the total thickness. We also measured the thick assay backing layer for the use in thermal model. The thickness data is shown in Table 5.1 together with other modeling input parameters.

Extract properties for GNP-laden membranes. The optical properties measurement method was introduced in detail in Ch. 2. Here, the integrating spheres spectrophotometer tests were done by our collaborator Dr. Scott Prahl from the Oregon Institute of Technology. Two copies of independently prepared 0.3 nM (1x), 0.15 nM (2x), and blank control samples were measured and averaged (Fig. 5.3). Detailed optical measurement data are available in Appendix B.

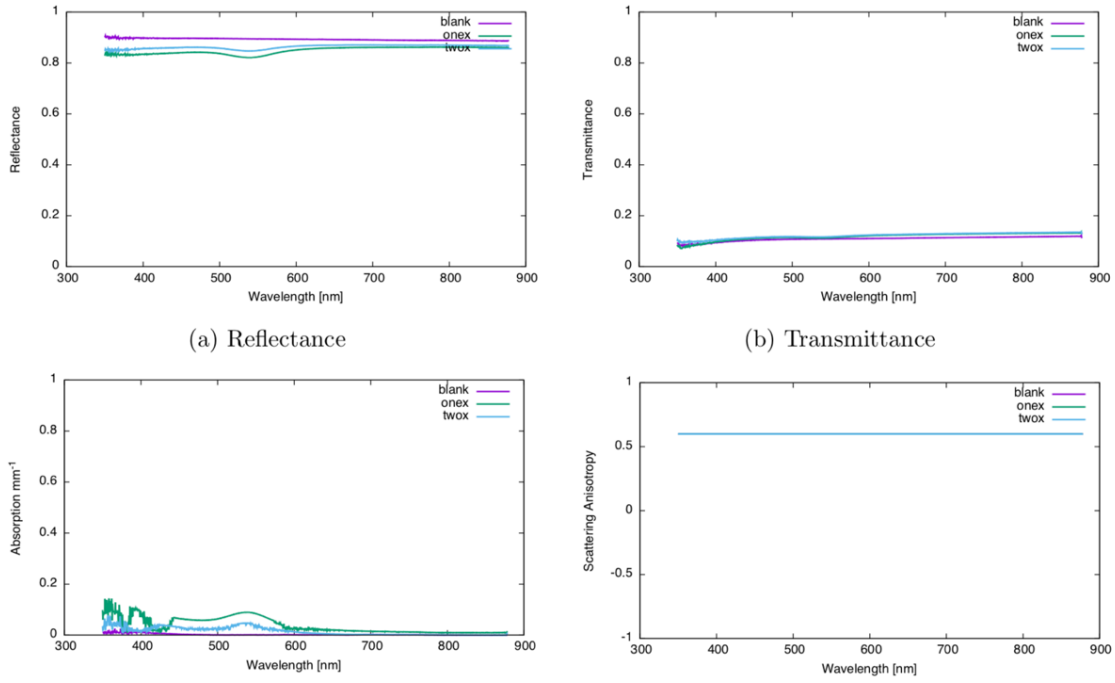

(a) Reflectance (b) Transmittance

(c) Absorption (d) Scattering Anisotropy

Figure 5.3. Integrating sphere spectrophotometer measurement summary plots.

We were able to get the necessary optical and thermal properties from our own measurements or published studies. Since the LFA membrane is a porous structure with 75% porosity, the nitrocellulose layer was weight averaged with nitrocellulose polymer and air thermal properties.[109] Here are the input parameters for the MCML and COMSOL models for the printed GNP-laden LFA membranes:

Table 5.1. Optical and thermal properties and input parameters for LFA optical-thermal modeling

Material	n	μ_a [cm^{-1}]	μ_s [cm^{-1}]	g
GNP Concentration 1 (0.3 nM)	1.45	0.88	2600	0.6
GNP Concentration 2 (0.15 nM)	1.45	0.46	2778.3	0.6
Blank Membrane	1.45	0.01	3446.8	0.6
Material	ρ [kg/m^3]	k [W/(m·K)]	C_p [kJ/(kg·K)]	Thickness [μm]
Membrane[110–112] (Air + Nitrocellulose)	344.61	0.078	1.174	50
Membrane backing[113] (Mylar film)	1390	0.181	1.172	90
LFA Backing[114,115] (Polystyrene)	1054	0.146	1.215	500

LFA optical-thermal modeling. To examine the MCML and COMSOL finite element model, they were first applied to the GNP-laden LFA membrane samples alone. With all the properties and COMSOL modeling, the temperature rises of 1x, 2x and blank control samples were modeled with the same boundary conditions and laser beam parameters (0.3 mm gaussian beam, 30 mW output power) as real TCA tests. By comparing to the TCA experiment, we can see the model agreed quite well with test data, though the trend of the deviation differs in each case (Fig. 5.4). For the 1x high

concentration sample, the model-predicted temperature curve was higher than the experimental results; for the 0.15 nM lower concentration, the difference was less prominent; while for the blank sample the prediction was lower than the experimental data. Multiple factors might contribute to this result: for example, the nitrocellulose layer was highly scattering, so the optical measurement error for the blank sample could be higher than the GNP-laden ones for the very little absorption photon amount. Errors in boundary heat flux could be another issue. The 2x heat source term will be used for whole LFA characterization and optimization modeling in the following sections for its better model-experiment agreement.

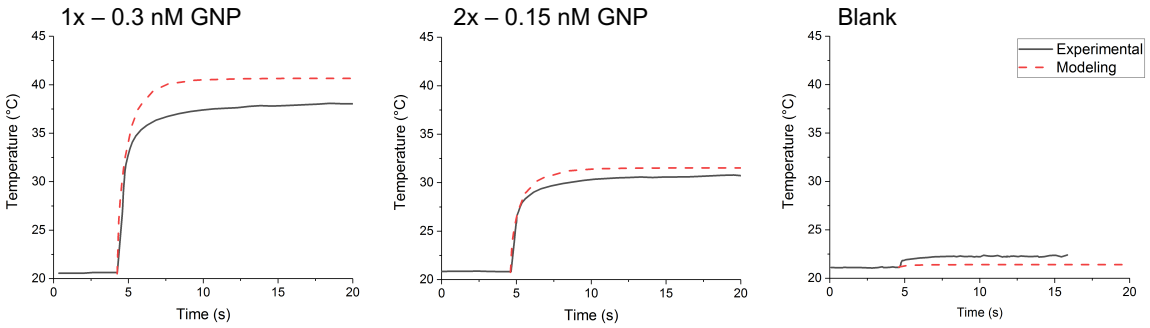

Figure 5.4. Optical-thermal model and experimental measurement of LFA membrane layer photothermal heating results comparison.

5.2 Characterization and Optimization of TCA

Modeling the TCA reading of the whole LFA. When we included the LFA assay backing layer to the FEM thermal model, the results would represent the real TCA measurement on LFAs (Fig. 5.5A). The LFA was modeled to heat to steady state (>30 s heating) and then cooled down to room temperature (>20 s cooling). A spatial resolved temperature distribution on the LFA surface was

also plotted in Fig. 5.5B&C which shows the radial temperature distribution from the center of the laser beam (r = 150 μm). We found the shape of the temperature distribution curve broadened with time, possibly due to heat dissipation increasing and the peak temperature rising speed kept decreasing. This indicates that the heat generated by the GNPs under laser irradiation conducted to the surrounding area. For a TCA test, the 'contrast' between heated GNPs and surroundings identifies the presence of detection targets. With the heating time increasing, the detected temperature increased but the raising rate decreased. It is due to more dissipated heat that also not favorable for elongating the cooling time. There should be a 'sweet spot' heating time for a certain LFA product that balances the TCA sensitivity (temperature rise) and efficiency (test time). Also, the IR detector in TCA need to be high-resolved to ensure the signal intensity, since the radial temperature gradient is very large even at steady state.

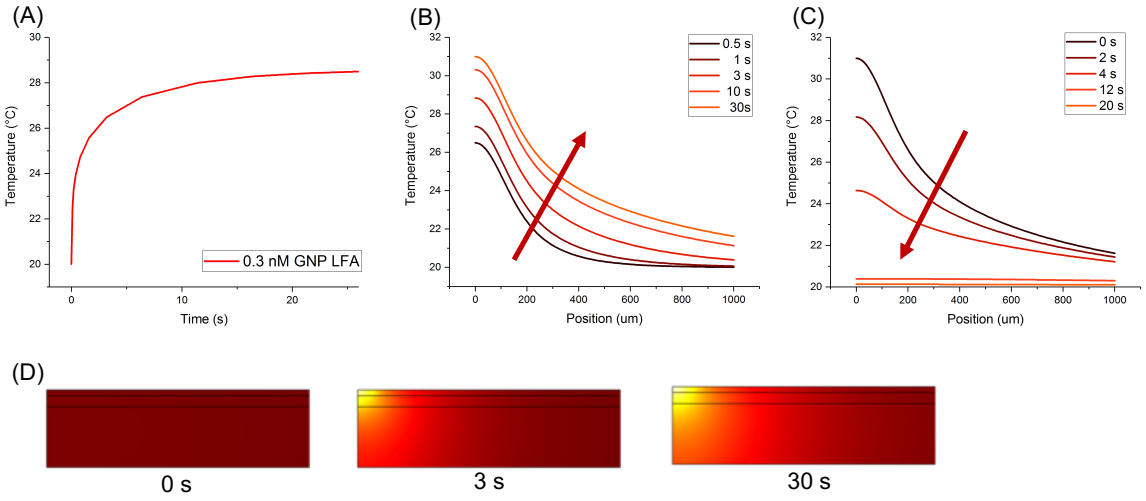

Figure 5.5. Model of TCA for real LFA. (A) Temperature rise by IR camera. (B) Temperature distribution curves during heating until steady state. (C) Temperature distribution curves during cooling from steady state. (D) Temperature distribution at cross-section during heating.

Characterizing the effect of laser beam on TCA. A better understanding of the laser beam parameters on the TCA could help identify and optimize the limiting factors for component alignment. Three conditions were chosen and studied: constant beam size (varying output power), constant output power (varying beam size), and constant laser intensity (varying beam size and power) (Fig. 5.7, red lines refer to the current TCA beam setting). The laser intensity changes in the case of constant beam size and constant output power, referring to the possible alignment errors in laser power and focusing length in the TCA reader. While both factors play important role for the final temperature rise by TCA, the beam size is the major issue for TCA measurement errors: 0.2 mm larger beam size would lead to about 5 ˚C drop in TCA steady state temperature rise. The laser and focusing lens position should be precisely controlled to maintain the beam size. To maximize the TCA signal strength, increase the laser beam size and output power together (i.e. keep laser intensity constant) will result the most signal rise. However, the dissipated heat in this case is also larger than changing one parameter alone.

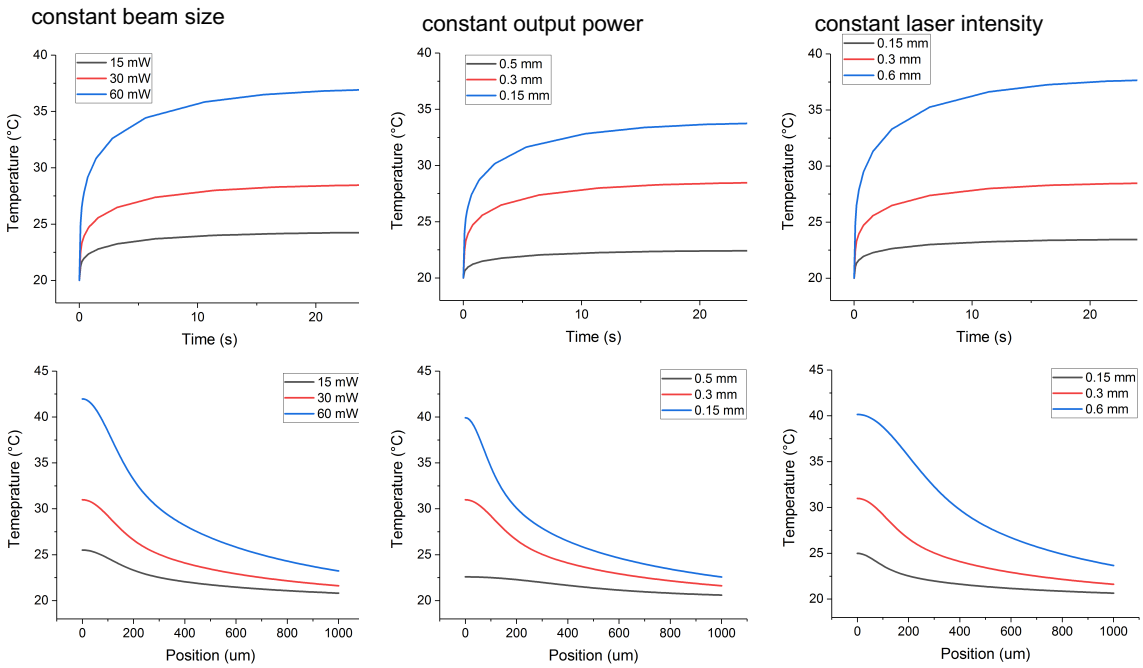

Figure 5.6. TCA laser beam parameters characterization. Temporal heating curves (up) and surface spatial temperature distribution at steady state (down) are plotted for three common conditions.

Characterizing the effect of LFA backing material on TCA. Comparing the temperature change curves of the LFA membrane alone in Fig. 5.4 and the whole LFA (with backing) in Fig. 5.5, we can find that the curve gradient is smaller and the steady state temperature is lower for the whole LFA case. Given the same laser and GNP distribution conditions, the reason for this difference could only be due to the heat sink effect of the LFA backing layer. We aimed to determine if the TCA results could be optimized for selecting the best backing material with the most suitable thermal properties. Two extreme cases were simulated and compared where copper backing (same thickness as LFA polystyrene backing) was taken as the most heat transferred and an insulated boundary below the membrane was taken as no heat transferred. Normal LFA backing and no

backing (air) results are also plotted in Fig. 5.7. It is interesting to find the temperature rising speed for air, the insulated boundary, and the copper backing cases are all faster than the LFA backing case. For the no backing and insulated boundary conditions, almost all the heat by TCA contributes to the membrane temperature rise; for the copper backing condition, with the low heat capacity and high conductivity of the backing layer, the membrane temperature rises faster but reaches a lower steady state. The copper backing ambient temperature is higher than the other cases for the same reason. The results indicate that the LFA strips should avoid direct contact to any structure when loading to the TCA reader; and, if possible, the LFA backing layer should be abandoned or changed to a thermal insulated material in LFAs specially designed for the TCA reader.

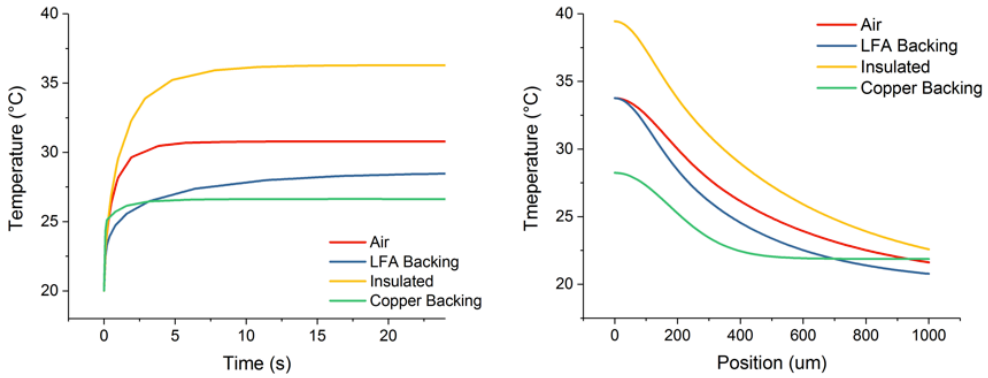

Figure 5.7. Characterizing LFA backing material for TCA. Temporal heating curves (left) and surface spatial temperature distribution at 30 s (right) are plotted for three common conditions.

TCA reader new algorithm development. We've come up with three data acquisition algorithms so far: 1) *Single point heating.* Three points on the test line are randomly chosen and heated until steady state. The average temperature rise is used as the TCA signal. There are several drawbacks to this algorithm including the need to collimate the test line manually and the

impossibility of distinguishing if the signal is from the GNP or some other nonspecific absorption (e.g. blood). No background measurement is compared to the TCA signal resulting in larger measurement errors. This algorithm was used to generate data for the proof of principle[44] but was replaced in the reader development paper[106].

2) *Discrete heating.* As described in the background section, this algorithm enables full automation of the TCA reader. The whole range between the control line and the test line is involved, so the test line is auto-located by the fixed distance to the control line. The laser performs a full working cycle on each position (i.e. 3s preparing, 3s heating and 3s cooling) and moves on to the next position (usually 0.125 mm apart). This algorithm has been validated by 3 commercial LFAs.[106] However, it suffers from a low throughput (e.g. >10 min to test a 1 cm region), while some commercial LFAs have even longer test regions (e.g. 13 mm for First Response malaria,) [106]. Optimally, we would like the test time to be shorter than 2 min for clinical applications.

3) *Continuous heating*. In this new algorithm, the laser will continuously scan across the same region as discrete heating (Fig. 5.8). By applying the continuous heating, the throughput of the TCA reader is expected to increase by 5 to 10-fold, thereby accessing times less than 2 min for one read. Since the laser is irradiating during the whole process, heat dissipation to surroundings should be controlled in a low level to avoid the TCA temperature rise being covered. Based on our COMSOL modeling, a smaller beam size should be applied. A higher laser output power may be helpful in the continuous algorithm. By adjusting the laser power and moving speed in the model, the new

algorithm matches the discrete algorithm results (Fig. 5.8A). Experimentally, we started testing with FirstResponse malaria LFAs for the new algorithm development. With 20 mW laser output power and 0.1 to 0.2 mm/s moving speed, we were able to achieve similar analytical sensitivity compared to the discrete algorithm on the LFA. Fig. 5.8B shows a typical result of a visually false negative FirstResponse LFA. It is clear that the continuous algorithm was able to catch the invisible test line with the same shape and S/N ratio as the discrete algorithm. Moreover, if a faster speed is applied, the similar signal showed but with slightly lower amplitude. The temperatures of the continuous algorithm are higher than the discrete algorithm because temperature was used instead of a temperature rise. It is worth mentioning that we only tested the test line and some background region before and after the test line on the malaria strips with the continuous algorithm. The control line was not included because the laser output power could generate too much heat, leaving a burn mark on the membrane. When applied in the next generation reader device, a lower power should be applied to the control line by adjusting the laser's voltage input or adding an ND filter.

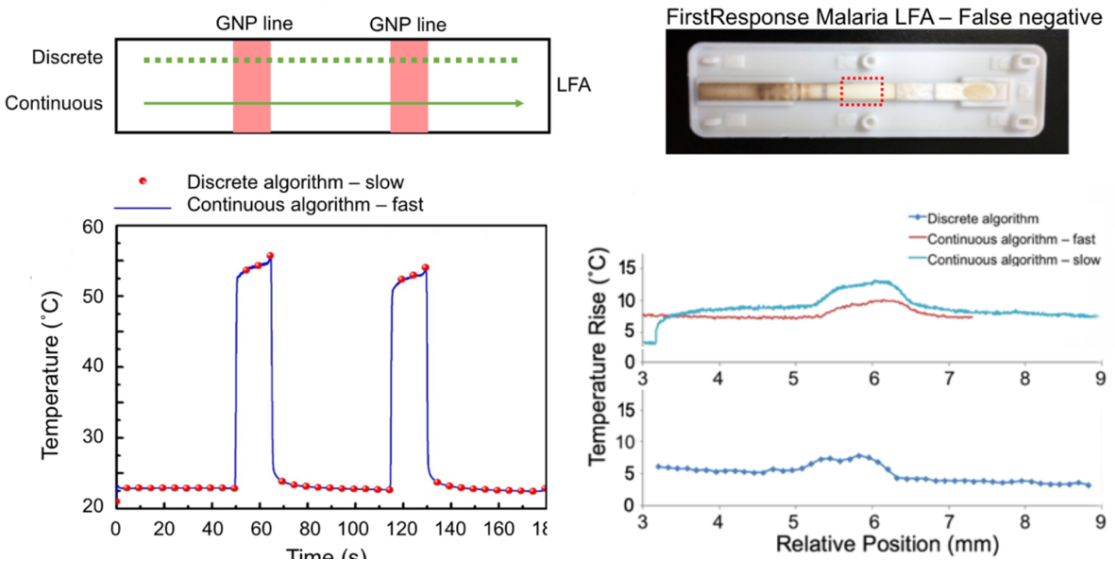

Figure 5.8. New TCA reader algorithm design. (A) Continuous reading algorithm matched the discrete reading algorithm results by modeling. (B) Experimental results of a FirstResponse malaria LFA showed the continuous reading algorithm.

Improve the TCA reader with new components. The existing desktop TCA reader is functional but heavy, expensive, and inefficient. The new key components (laser and IR detector) for the next generation compact and portable reader need to be smaller and cheaper. If the new components are proven to perform equivalently as the current reader components (with all other components kept the same), the new system will also be equivalent to the current reader. The scheme of the control system will remain while few changes need to be made for the new algorithm.

Among the laser light sources tested, the TECGL-30G-520 laser (WorldStar Inc.) was selected. The selection criteria included: performance; cost; consistency; and robustness for a laboratory-based working environment. All the characterization results were very close to or even better

than the desktop laser (1.9% output power stability, 0.1 mm focused beam size and narrow spectrum). The results of this characterization suggested that the new laser satisfied the criteria of

our investigation and could be used for the portable TCA reader. We also tested some lower-cost IR sensing products (FLIR E30 IR camera, Melexis 90620 IR sensor array, and Melexis 90614 5˚ FOV IR sensor). These tests include a room temperature to 100˚C calibration curve and a direct comparison to the A325sc camera in a 1 min mimic to the TCA test. However, these items suffered from poor computer interface or lack of spatial resolution, thus not fit the system. The Micro-Epsilon sensor was selected as the IR detector for the portable TCA reader. It has very good resolution (0.8 mm minimum focused size). When compared to the FLIR IR camera, though the temperature reading diverted at high temperature, the results under 20℃ temperature rise agreed quite well. This range is where the test line signal in TCA tests usually fall in.

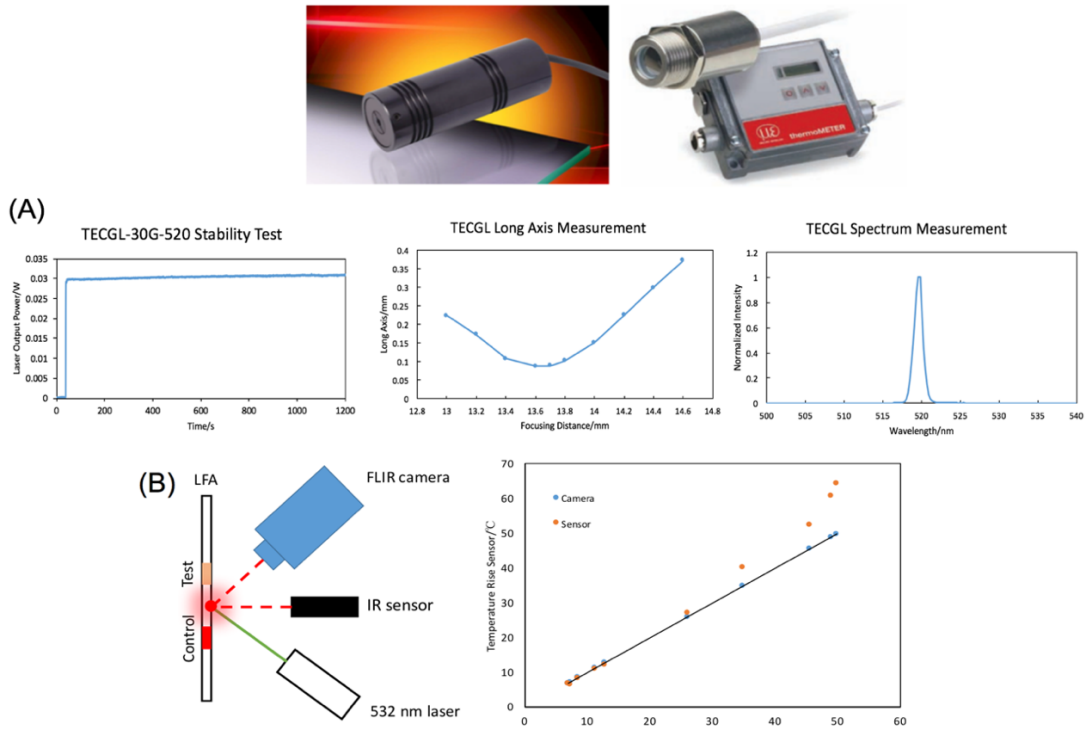

Figure 5.9. Characterization of the key components for the new portable TCA reader (A) laser and (B) IR sensor.

Summary. With the measured optical properties and modeling results for the TCA reader, we make the following suggestions for the next generation reader device:

a. Configure the laser parameters for each type of LFA tested with the reader
b. Find the best combination of laser beam size and output power for balanced signal intensity and cooling time
c. Change the LFA backing to a thermal insulated material or just air for less heat loss
d. Apply a continuous reading algorithm and adjust laser's configuration
e. Characterize any new laser or IR detector carefully to ensure the performance.

Chapter 6 Aggregation Affects Optical Properties and Photothermal Heating of Gold Nanospheres

Abstract

Laser heating of gold nanoparticles (GNP) are increasingly used in biomedical applications due to the ability to design precise optical properties and therefore heating of GNPs. Nevertheless, GNP properties estimated by nominal morphology under idealized dilute and mono-disperse conditions can vary dramatically from real situations in biological solutions where the GNPs may be aggregated thereby impacting GNP heating. To address this, we studied the effect of GNP aggregation within a wide range of particle sizes 5, 16, 30 nm gold nanospheres at aggregation size from 2 to 30 particles by both discrete dipole approximation (DDA) and an experimental calorimetry approach. Due to computing resources, we focused only on compact directly coupled aggregation geometries. Our comparative photothermal heating experiments were performed within a calibrated "laser GNP calorimetry" system where aggregation was controlled by NaCl in 16 and 30 nm size GNPs. Our numerical data shows that aggregation will affect the heating by 15-28% under conditions of compact direct coupled geometries. The laser calorimetry measurement shows similar trend as DDA modeling, although it can occasionally increase by up to 6% by the differences in geometries. These results show that GNP heating can be measured and predicted under aggregated conditions and that controlling and/or avoiding aggregation will be necessary for

precise dosing of GNP laser heating in biomedical applications. This work also provides a framework for understanding the impact of aggregation on laser heating of nanostructures.

6.1 Introduction

Laser heating of gold nanoparticles (GNP) are increasingly used in biomedical applications ranging from molecular to bulk tissue heating applications.[116] The advantages of laser GNP heating include excellent light to heat conversion, rapid heating rates. For instance, while iron oxide nanoparticles have been used for decades in cancer treatments, they typically have heating rates in the 100s of W/mg Fe vs. 100s of W/μg for GNP[116]. In addition, GNPs allow facile chemistry and coating for biological applications.[116,117] In addition to traditional plasmonic tumor ablation, the growing interest for GNP photothermal heating has been extended to other aspects in biomedicine (Table 6.1). A related application of GNP under laser irradiation includes photodynamic therapy.[118] All of these applications rely on GNPs to convert laser light energy to heat by surface plasmon resonance.[11] Ideally, this heat can be estimated from the absorption cross section of a single GNP multiplied by the laser fluence rate ($Q_{GNP} = I \bullet C_{abs}$). However, in real biological systems, the distribution of GNPs can be quite non-uniform and aggregation can occur.[18,119] Factors such as polydispersity alone can reduce the theoretical prediction of heating in a system by as much as 70% recently shown for gold nanorods.[16] Here we pursue a careful analysis of laser GNP heating under aggregated conditions to help control dose and impact of heating in biomedical applications and/or

inspire next generation particles that control aggregation.

Table 6.1. Emerging biomedical applications of laser GNP heating

Application	Gold Nanoparticle	Laser
Diagnostic assays[44,106]	30-100 nm GNS	CW, 532 nm
Cryopreserved biomaterial Re-warming[120,121]	1064 nm resonance GNR	ms pulsed, 1064 nm
Controlled drug release[122,123]	2-5 nm GNS 25 nm GNR 44-60 nm nanostars	250 or 514 nm 656 or 808 nm 803 or 850 nm
Tissue stimulation[124]	Cardiac, 200 nm GNS Neuron, 750–810 nm GNR Skin, 8-10 nm GNS	ps pulsed, 532 nm CW, 780 nm & pulsed 800 nm CW, 532 nm
Antibacterial biofilm treatment[125–127]	10-15, 40 nm GNS 785 nm resonance GNR	CW, 665 nm & ns pulsed & 420-570 nm CW, 785 nm
Selective virus inactivation[128]	805 nm resonance GNR	fs pulsed, 805 nm
Selective protein inactivation[129]	15, 30 nm GNS	ns pulsed, 532 nm

Typical tools used studying GNP photothermal conversions include theoretical methods (e.g. Mie theory, discrete dipole approximation, and finite difference time-domain), spectrum optical properties characterization (e.g. UV-Vis spectrometry, small-angle X ray scattering) and GNP solution photothermal conversion experiments (e.g. in a droplet, in a cuvette in vacuum or standard room temperature and pressure).[16,22,27,28,34,130] Among the many non-ideal factors in real photothermal application, GNP size polydispersity and aggregation are only related to the particles themselves thus relatively easier to characterize. Size polydispersity of GNPs, determined by fabrication accuracy (difference to nominal size), has been relatively well studied.[16] It has been confirmed gold nanospheres are not sensitive to polydispersity while gold nanorods heating drops remarkably. Particle aggregation phenomenon is even more complicated. The aggregations of

GNPs in biomaterials are quite common with even the most well-fabricated and characterized particle samples. Indeed aggregation can be induced in ionic or protein based solutions.[119,131,132] This can lead to a dramatic drop in heating of nanoparticles, for instance highly aggregated IONP in radiofrequency fields.[132,133] There are also numerical studies showing gold nanosphere (GNS) optical extinction spectrum shifts under aggregation.[134–136] While many parameters were studied including aggregation geometry (e.g. GNS dimers, GNS chains, GNS coated hollow spheres and cubes by eight GNSs), gap distance in assembly, GNS distribution pattern, incident light polarization, incident light angle and etc. No specific conclusions with regard to how GNP aggregation will affect heating were offered, and we are unaware of any study that has yet carefully assessed this.

Here we chose a typical size range of GNS (5, 16 and 30 nm) and aggregation sizes (2 to 30 particles) for both numerical and experimental study. Due to computational cost we focused on the densest assembly geometries of GNS and focused only briefly on other different geometries of aggregates. Discrete dipole approximation (DDA) simulations showed a clear trend of optical properties change under aggregation for all GNS sizes. These theoretical results were then compared to cuvette “laser GNP calorimetry” and shown to be consistent. Interestingly, DDA suggests that isolated single GNS will heat better than any size of clusters, although we are unable to achieve completely mono-disperse aggregation solutions to test this. In general, GNS aggregation assemblies show a shifted, broader spectrum by UV-VIS. Although their optical

extinction at the original plasmonic peak is lower, the higher near infrared extinction may inspire new applications for aggregated GNS.

6.2 Materials & Methods

Numerical Methods

*Geometry Generation***.** The earliest stages of aggregation proceed through monomer (primary particle) addition to a growing aggregate, as the number concentration of monomers greatly exceeds the aggregate concentration. While both diffusion limited and reaction limited aggregate mechanisms suggest that such early-stage "cluster-monomer" formed aggregates are relatively dense,[137] here we attempt to examine the influence of aggregate morphology on photothermal heating. For this purpose it is convenient to describe aggregate morphology as statistically fractal, with each aggregate approximately obeying the scaling law:

$$N = k_f \left(\frac{R_g}{a} \right)^{D_f} \tag{6.1}$$

where N is the number of primary particles in the aggregate, a is the radii of the primary particle, k_f is the fractal prefactor, D_f is the fractal dimension. Following the statistical fractal model, the GNS aggregate geometries used in all the present calculations were generated using a Sequential Algorithm (SA) which has been described in detail previously.[138,139] Though the SA approach has difficultly reproducing the features of large (N > 100) aggregates, it is a rather robust algorithm capable of generating both relatively spare and relatively dense aggregates. The SA

enables random generating of an aggregate with prescribed k_f and D_f; identical primary particles are added to the aggregate one by one, satisfying equation (1) at each step. In the present study, we set $k_f = 1.6$, and the number of the primary particles in the aggregates studied was 5, 10, 15, 20, 25, and 30. To study whether aggregate morphology had any influence, the fractal dimension was adjusted to control the assemble state (dense or sparse) with $D_f = 1.4$ (sparse and chainlike), and 2.4 (dense).

Discrete Dipole Approximation Calculation. DDA solves Maxwell's equations by discretize the target, either regular or irregular shaped, into a finite array of dipoles. DDSCAT 7.3 was used to perform DDA simulations.[140] Validation of parameter configuration was made by matching our results of single 30 nm GNS to previous work.[16] We also set 4 dipole/nm which provided extra accuracy while still computationally reasonable. To mimic the most common photothermal conversion application, an unpolarized single wavelength light source is used and water set as surrounding medium. Although the isotropy of isolated GNSs makes the optical properties independent of incident light direction, GNS aggregation is usually anisotropic thus requiring an average of the calculation results by several orientations. We tried various orientations and ultimately settled on 5 to be a sufficient number (Fig. 6.1). Table 6.2 shows the calculation matrix in this study. We did a calculation with coarse wavelength step sizes first to find the overall shape of spectrum curves and then refined the step size close to the plasmonic peaks for accuracy. In order to compare the photothermal conversion of various size GNS aggregations, the optical properties

(i.e. cross-sections) were averaged by GNS numbers in an aggregation cluster with the equation:

$$C_{ext,average} = \frac{Q_{ext} A_{eff}}{N} \tag{6.2}$$

where $C_{ext,\ average}$ is the number-averaged extinction cross-section of GNSs in an aggregation cluster, Q_{ext} is the extinction coefficient of the whole cluster and the direct output by DDSCAT, A_{eff} is the effective geometric cross-section area, N is the number of GNSs of the aggregation. The numerator is the extinction cross-section of the aggregation.

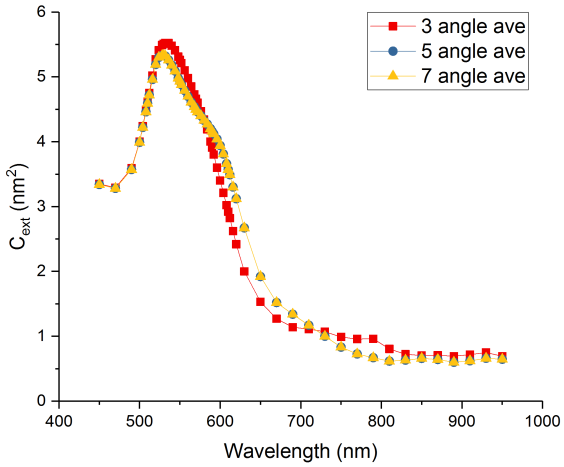

Figure 6.1. Incident light direction average for DDA simulation. A sufficient number of incident light directions need to be calculated and averaged in order to simulate the real condition of GNSs in solution.

Table 6.2. DDA simulation matrix of aggregated GNSs

Parameters	**Values**	
Geometry Type	Dense	Sparse
GNS Aggregate size	2, 3, 4, 5, 10, 20, 30	5, 10, 20
GNS Diameter (nm)	5, 16, 30	5, 16
Wavelength (nm)	450 - 950	
Wavelength Step Size (nm)	20 for bulk; 4 for range of resonance peak (±50)	

Experimental Methods

GNS Synthesis. GNS were synthesized following published methods.[107,108] All the glass wares and stir bars were cleaned by Aqua Regia prior to the synthesis. All chemicals were purchase from Sigma-Aldrich without further purification. The 16 nm GNS were produced by adding 0.5 mL 3% (W/V) sodium citrate into boiled 50 mL 0.25 mM HAuCl4 under vigorous stirring. The resulting 16 nm GNS were used both for the following aggregation study and as seed for 30 nm GNS. The 30 nm GNS were synthesized by adding 0.875 mL 25 mM HAuCl4, 15 mM sodium citrate, 12.5 mL as-made 16 nm GNS and 25 mM hydroquinone successively into vigorous stirred MilliQ water and continue stirred for 30 min at room temperature. The resulting GNS were characterized by dynamic light scattering (DLS, Brookhaven Zeta PALS instrument), transmission electron microscopy (FEI Tecnai T12) and UV-visible spectroscopy (Ocean Optics, Dunedin).

Induce and Stabilize Aggregation in GNS Solution. 16 nm GNS aggregation was induced by a modified published method.[119] A series 50 mL NaCl+ transferrin (TF) stock solutions were made as instructed here: 25NaCl+TF: 0.5844g NaCl+0.0040g TF; 100 NaCl+TF: 2.3376g NaCl+0.004g TF; 400NaCl+TF: 0.3504g NaCl+0.004gTF. The number on the NaCl+TF stock solution indicated the final concentration of NaCl in the aggregation solutions. For example: 25NaCl+TF resulted in 25 mM NaCl in the final GNS solution. A TF stock solution was made by dissolving 0.0064g TF in 20 mL MilliQ water. To induce the aggregation, 0.4 mL NaCl+TF stock solution was added to 2.4 mL GNS solution and vigorously vortexed for 1 min then 0.4 mL TF stock solution was added

to stabilize the aggregations.

TF was not sufficient to stabilize 30 nm GNS aggregations, and we observed enlarge aggregation after TF was added. We used polyvinyl pyrrolidine (MW=10,000 g/mol) to stabilize 30 nm GNS aggregates that also induced by NaCl addition. The protocol was optimized by both varying NaCl and PVP additions to generate small aggregates. Similar to 16 nm GNS, A series 10 mL NaCl stock solution was made: 100 NaCl: 0.46752g NaCl, 200 NaCl: 0.93504g NaCl; 400 NaCl: 1.87008g NaCl. A PVP10 stock solution was made by dissolving 25 mg PVP10 in 10 mL H2O. The aggregation was induced by adding 0.4 mL stock NaCl to 2.4 mL GNS solution and vigorously vortexed for 1 min, then 0.4 mL PVP10 stock solution was added to stop further aggregation.

Calibrated Cuvette Laser GNP Calorimetry Measurement. This system has been used previously to assess laser heating of a series of GNSs and GNRs.[16,121] Briefly, GNS solutions are loaded into a four-side plastic optical cuvette and heated with a 532 nm CW laser (190 mW). To minimize measurement errors, four temperature thermocouples and a magnetic stirrer were applied. The GNS solution was photoheated to steady state (>0.1 ˚C temperature change in 1 min) and a maximum temperature rise was measured (ΔT, ˚C). A known-power resister heater was placed in the cuvette system and used to calibrate the *SAR* assuming the laser GNP heat source of the same power produced the same temperature rise. The resister heater calibrations were performed multiple times over a wide power range (25-250 mW). By measuring the temperature rise, we found a linear

correlation between ΔT and the experimental photothermal heat generation (P_{exp}, mW) with a fitting coefficient (Eq. 6.3):

$$SAR = P_{exp} = 16.855\Delta T \tag{6.3}$$

Cuvette calorimetry measurement was conducted three times for each GNS aggregation sample under the same conditions. In this experiment, P_{exp} equals the specific absorption rate (*SAR*) from the laser GNP heating.

6.3 Results & Discussion

Numerical Results

In this study, we seek the simple trend or rule to govern the optical properties change of aggregated GNSs and hope it could help explain and optimize biomedical applications. We applied a random collision algorithm to generate the most compact aggregation geometry that happens naturally for aggregations of equals or exceeds 5 GNSs. For smaller aggregation, we take the mathematic close-packed assemblies (Table 6.3). The gap distance effect is not considered in our model. We assume that the aggregation effect will be more prominent for dense, compact geometries, since GNSs will behave as isolated particles when separated at a long enough distance. Each adjacent GNS is single-point contacted with its neighbors. The optical response of 5, 16, and 30 nm diameter GNSs were chosen to be studied to cover a relatively large size range while saving computing resources. They are widely applied, and the fabrication methods are well-established.

Calculating GNSs larger than 30 nm in large aggregation was beyond our computing capability and therefore not included in this study (i.e. 60 nm GNS aggregations sizes 4 times larger than the 30 nm ones; and our computing capability could only finish a 5-particle aggregation of 60 nm GNS for a coarse step calculation in 1 week).

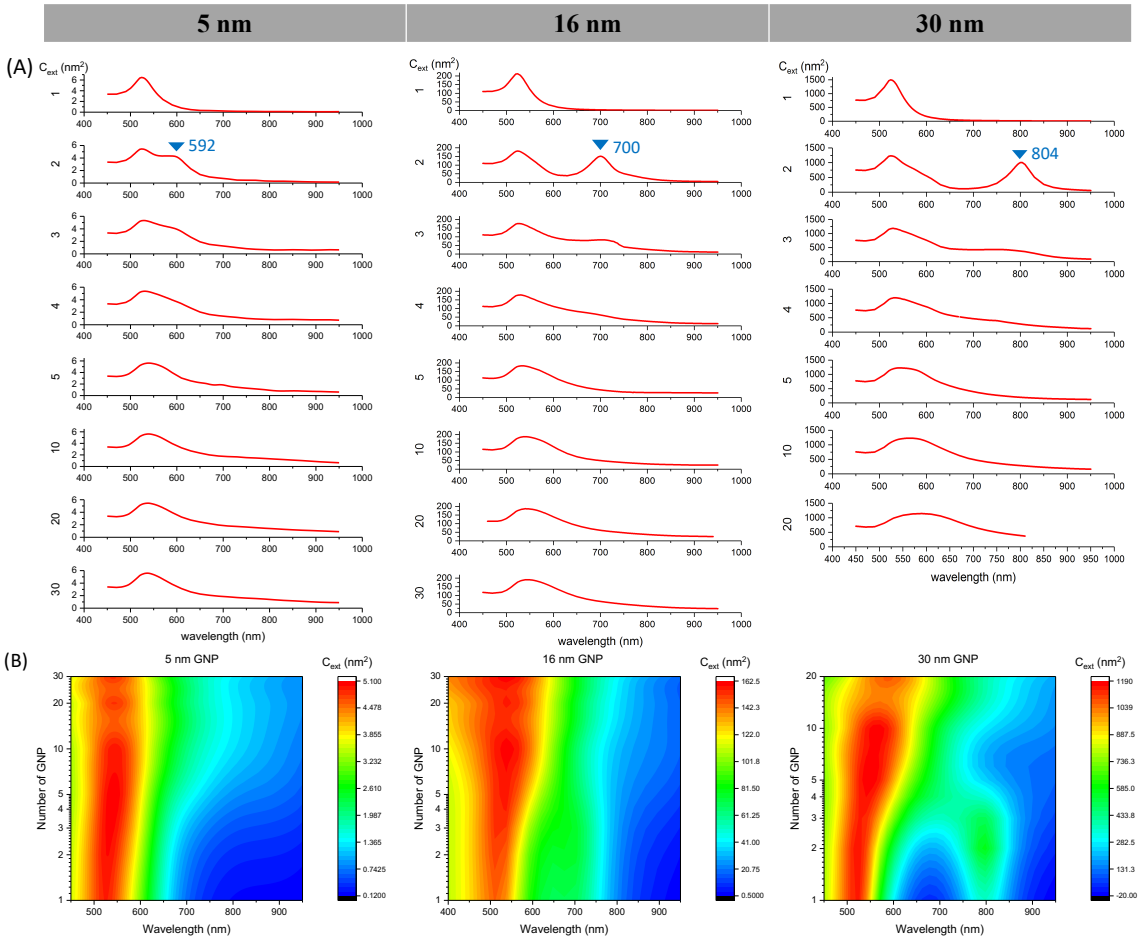

Figure 6.2. Averaged extinction cross-section of aggregated 5, 16, and 30 nm GNSs by spectra plots (A) and contour plots produced with fitting and smoothing algorithms (B).

Table 6.3. GNS aggregation calculated by DDA of 2-30 particles

Size	Single	2 GNPs	3 GNPs	4 GNPs	5 GNPs	10 GNPs	20 GNPs	30 GNPs
Geometry (Dense)	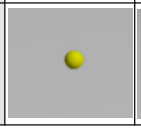	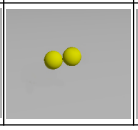	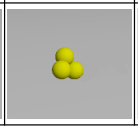	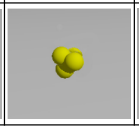			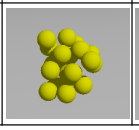	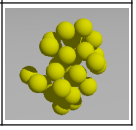

The DDA results for optical cross-sections are plotted for every case in SI. To study the trend of optical properties change with aggregation, we take the extinction cross-sections here for analysis (Fig. 6.2). The primary plasmonic peak showed broadening and red shifting for all three sizes of GNS while larger GNS has more prominent changes (Fig. 6.3). A prominent secondary plasmonic resonance peak showed up at 2-4 particle aggregations. As GNS diameters increase, the secondary peak is red shifted rapidly and diminishes faster with aggregation size. It became almost invisible for 30 nm GNSs at 3 particle aggregation while still slightly visible for 5 nm GNSs at 4 particle aggregation. This secondary peak is in some sense the inverse of the weaker VIS and stronger NIR peaks from gold nanorods. At the resonance peak, the photothermal conversion drops significantly (17-28%) and gradually recovers (partially). This could be induced by the 'shape effect' at smaller aggregation sizes, especially for dimers and trimers. However, GNS diameter also plays a role in the trend where 5 nm GNS aggregations tend to plateau, 16 nm tend to increase slightly, and 30 nm tend to descend. During laser heating applications a constant laser wavelength is usually applied instead of matching the GNSs resonance peak. For instance, 532 and 808 nm are commonly used photothermal laser wavelengths in biomedicine. The optical extinction of GNS aggregations differs by particle size because of the different plasmon resonance peak wavelengths.

For the extinction at 532 nm, the extinction of 5 nm GNS is very close to the resonance peak; the extinction of 16 nm GNS at lager extinction sizes is higher than the peak; and the extinction of 30 nm GNS keeps decreasing with aggregation size (Fig. 6.4). Therefore, heating of 5 and 16 nm GNSs compact aggregations of 2-4 particles at 532 nm is unfavorable for leaser heating; for 30 nm GNS, 2-5 particle aggregations are almost the same in heating at 532 nm but the heating decreases rapidly with larger aggregations. At 808 nm, the extinction cross-section increases rapidly by aggregation size for all GNS diameters. The spike of 30 nm GNS at small aggregation sizes is caused by the secondary resonance peak (804 nm).

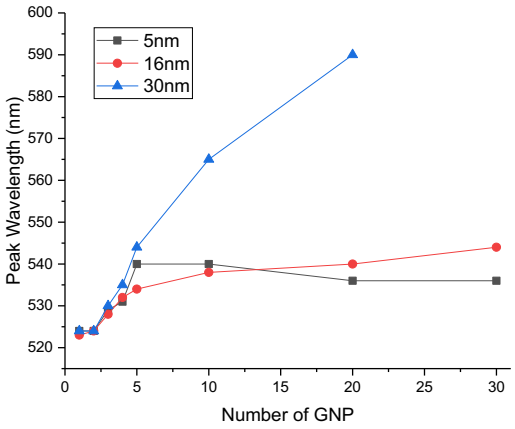

Figure 6.3. Plasmon resonance peak of aggregated GNSs. The larger the aggregation size is, and the larger the GNS diameter is, the redder-more shifted the aggregated cluster will have.

To explore how to use gold more efficiently in photothermal heating, we assume we have fixed total mass of gold. We then compared the heating by making the gold single large GNS, three particle aggregation, and 20 particle aggregation. Since the gold volumes are same (<1% difference

in effective radius) for the three cases, the extinction coefficient (Q_{ext}) shows the heating ability. We found the single particle is far better than aggregation clusters (Fig. 6.5). It is useful advice to use single larger particle and avoid aggregation when designing or optimizing a GNS heating system.

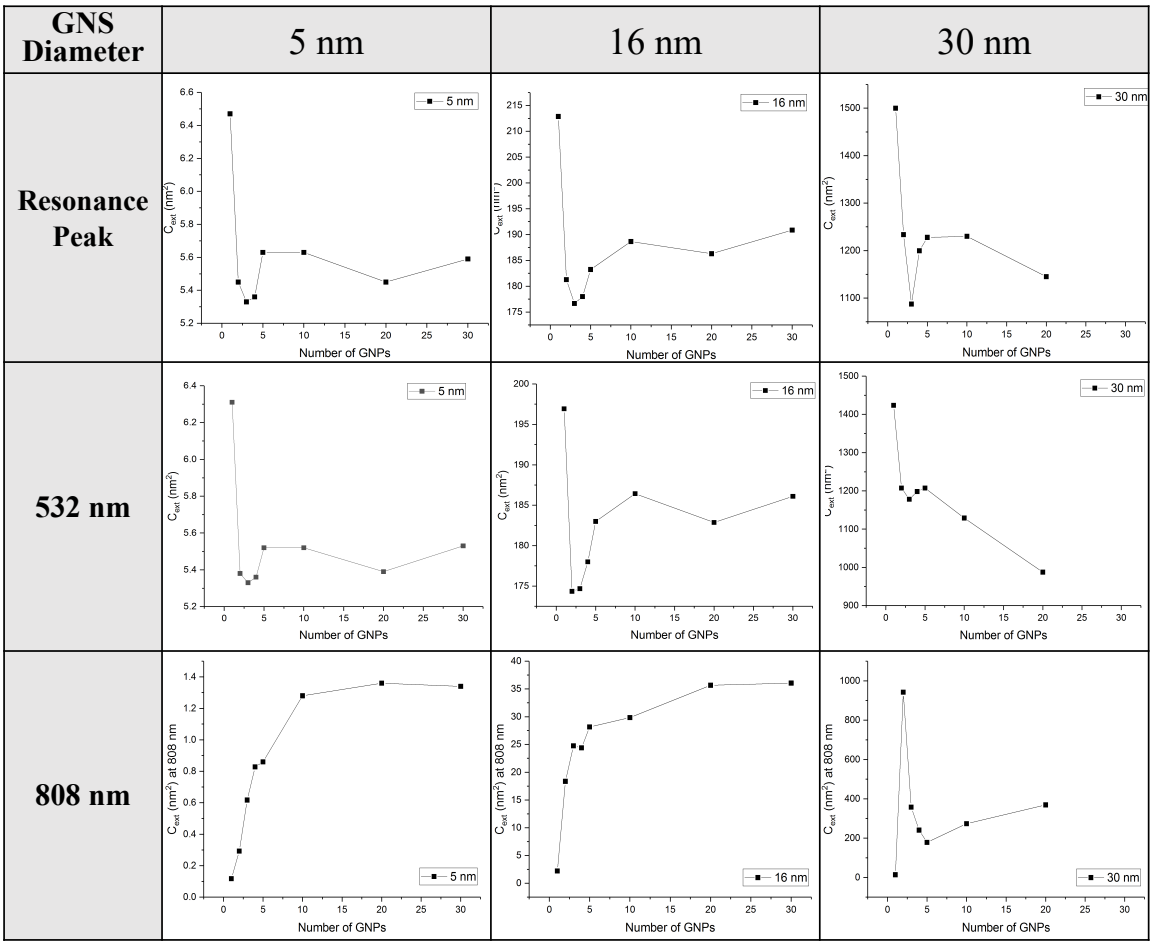

Figure 6.4. Average Extinction cross-section plots of 5, 16, and 30 nm diameter GNS aggregations at the resonance peak, 532 nm (green laser heating) and 808 nm (NIR laser heating).

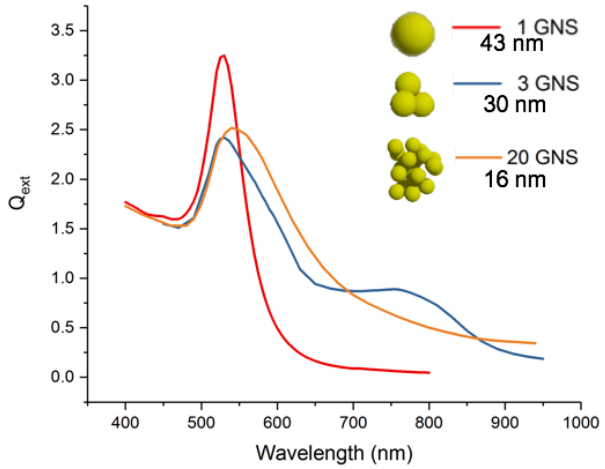

Figure 6.5. To explore the way to generate the most heat by the same amount of gold, the extinction coefficient (Q_{ext}) of 1, 3, and 20 particle clusters with very close effective radius (<1% difference) are compared. We can see the single GNS has the highest extinction at resonance peak, while an aggregation cluster with larger number of GNSs is slightly better than the small cluster.

Experimental Results

Characterization and photothermal conversion experiments were also conducted to compare to our numerical results Fig. 6.5(A). We selected 16 and 30 nm GNS for the experiment for the well-established fabrication methods and stable fixed aggregation states. After inducing aggregation with NaCl, transferrin was used to fix 16 nm GNS aggregates. For 30 nm, with the larger particle and cluster sizes, transferrin no longer worked and PVP was used instead to stabilize the aggregates. For GNSs larger than 30 nm (e.g. 60 nm), we didn't find any methods to maintain stable aggregates and sediments were shown to form directly after adding NaCl. The GNS aggregation samples and controls were pictured and characterized (Fig. 6.5(B)(C)). The color change and size distribution of 16 nm GNS were very similar to previous study[119], indicating good

aggregation results. For 30 nm GNS, though the color change is not as obvious as 16 nm samples, size distributions were clearly separated for each aggregation level based on the DLS results (Fig. 6.6(B)). The absorption spectrum of all the solution samples tested in this study showed no noticeable change one week after preparation or after heating experiment. Though the aggregation sizes and shapes were not uniform in each sample by TEM examination (Fig. 6.6(C)), clear trend of growing aggregation size was confirmed. The aggregation geometry here is not as compact as the numerical model, resulting in less interaction between GNSs. The experiment should be good to show the trend but could no reconcile numerical results quantitatively.

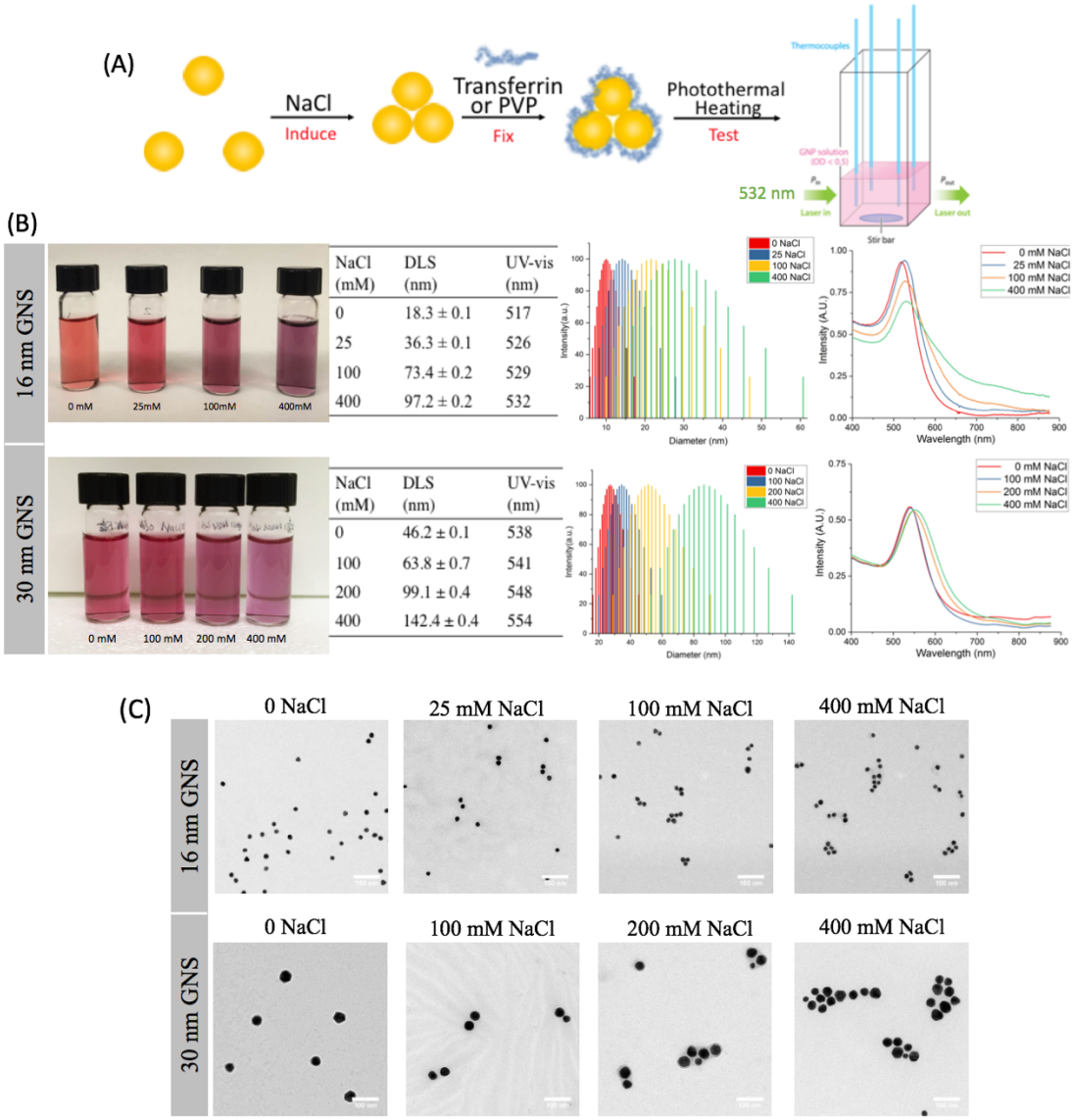

Figure 6.6. GNS aggregation photothermal conversion experiment preparation. (A) Experiment scheme: induce and fix controlled size GNS aggregation in solution and test by cuvette settings. (B) Visual picture, DLS and UV-Vis characterization of GNS aggregation solutions. (C) TEM Characterization of GNS aggregation solution samples in (B), 100 nm scale bar.

Once we carefully characterized the GNS aggregation samples, we measured their photothermal heating outcomes with the calibrated laser calorimetry as pictured in Fig. 6.6(A). Same volume of solutions was heated by same power of 532 nm laser until steady state.

Interestingly, different trends of photothermal heating were observed for 16 and 30 nm GNS aggregations (Fig. 6.7). For 16 nm GNSs, the heating increased at small aggregation sizes and decreased as the aggregation size continued to increase; for 30 nm GNSs, the heating decreased monotonically as the aggregation size went up. The result that GNS aggregation benefited the heating above any monodispersed control solution is surprising. When compared to DDA results of optical extinctions at 532 nm irradiation (Fig. 6.4, second row), the heating results agree with the trends of larger aggregations (i.e. more than three particles). The largest aggregation groups showed about 10% decrease in heating than control, while the heating of smallest aggregation of 16 nm GNS increased by 6.3%.

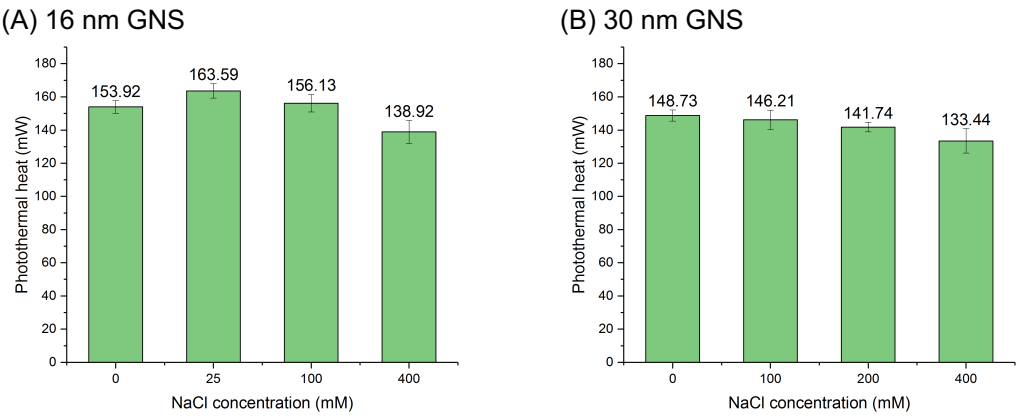

Figure 6.7. Photothermal conversion experiment result of aggregated GNSs under 190 mW 532 nm wavelength CW laser. The 16 nm result (A) shows a rise and decline trend and the same concentration aggregation solution with 25 mM NaCl heats better than monodispersed control solution. The 30 nm result (B) constantly declines, indicating different aggregated GNS photothermal conversion outcomes for different GNS size.

Discussion

To understand the photothermal heating of aggregated GNSs, DDA numerical simulations of optical properties were performed on a large set of GNSs of various sizes (5, 16 and 30 nm) and aggregation states (2–30 particles). Very compact geometries of GNS aggregation with direct particle contact were numerically calculated to represent the extreme case where the interparticle effect was maximized. For other GNS aggregation geometries, the optical properties should fall between isolated GNS and our extreme case. The change of optical properties with aggregation size was then analyzed. Though differences were observed for different size of GNSs, all the aggregations in our DDA simulation show a rapid decrease and then gradual partial recovery of optical extinction with increase in aggregation size. The GNS trimers of all three particle sizes has the lowest optical extinction at plasmonic resonance peak comparing to all other aggregation states, and then followed by the dimers. Based on Maxwell Garnett effect, the electromagnetic coupling between GNSs in colloidal solution becomes increasingly important when the center to center distance is smaller than 5 times the particle radius.[141,142] Besides the surface plasmon resonance of single isolated GNS, the inter-particle dipole coupling together induced the unique extinction spectra of an aggregation cluster. The cluster geometry of smaller aggregation cluster is more regular; therefore, the inter-particle resonance is more anisotropic by the non-uniform electron distribution. [141] This effect is supposed to count for the lowest primary extinction peak for dimers and the rapid secondary peak. On the contrary, the collective effect shares more equally to the whole

spectra for larger aggregations thus showing some recovery at the primary peak comparing to smaller clusters. Despite the aggregation size, different sized GNSs respond to aggregation differently. Interestingly, 30 nm GNS has more prominent resonance peak shift than smaller ones, which aggress with their better performance in aggregation colorimetric assays.[12,143]

We were only able to be focused on compact aggregation geometries in this study. For GNP aggregation happens in biosystem, the shape of aggregation clusters could be irregular, and the particles could be gapped (no direct contact) (Fig. 6.6C). To understand how aggregation shapes affect the optical properties, we also tried to generate some sparse geometries and performed DDA on them (Fig. 6.8A). Our results show the compact aggregations heat better than sparse ones in all GNP and aggregation cluster sizes (Fig. 6.8B). This could be explained by the more randomized dipole coupling in compact geometries than the relatively more linear shaped sparse geometries. On the other hand, the gap distances effect has been studied on GNS dimers in previous studies. It was found the primary peak amplitude increases with gap distance, or in other words the optical properties of loosely aggregated GNSs became closer to an isolated GNS spectra.[136] Therefore, aggregation shape and interparticle gap distance exert opposite influence on the photothermal heating of GNS aggregations on the base of our compact geometries.

(A)

Size	5 GNPs	10 GNPs	20 GNPs
Geometry (Sparse)	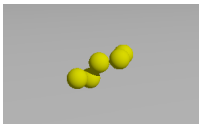	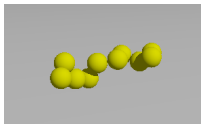	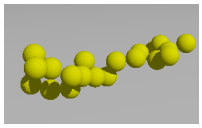

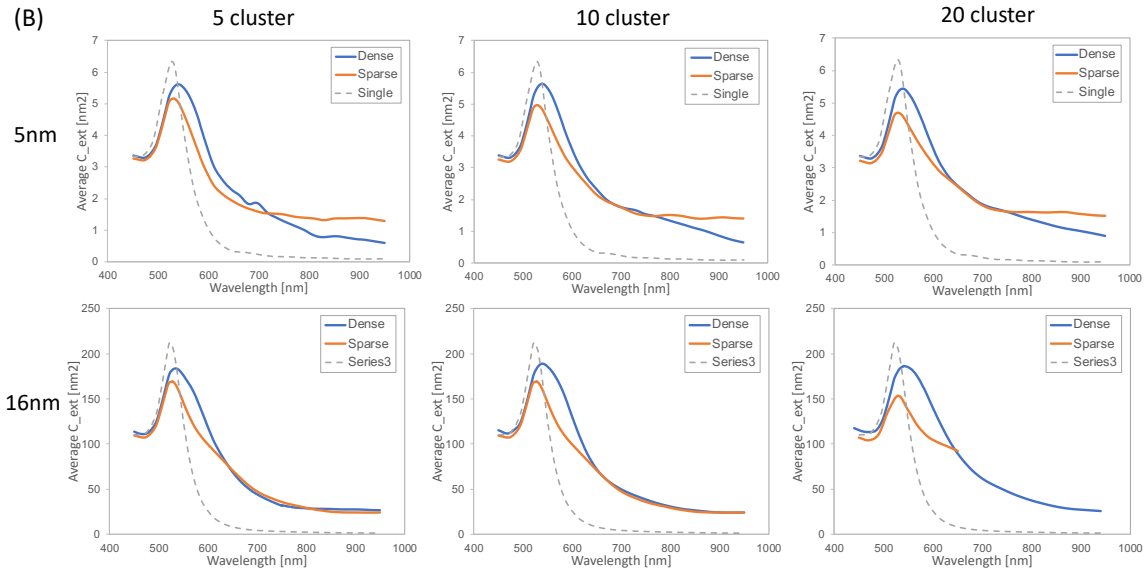

Figure 6.8. DDA simulation of sparse aggregation geometries. (A) Sparse geometries. (B) DDA results for 5 and 16 nm GNS aggregations.

Experimentally, with the stable, repeatable GNS aggregation samples synthesized, we were able to compare the photothermal conversion of different aggregation conditions. Sediments are common byproduct when inducing aggregation in GNP solutions and they impede the quantitative comparison of the heating.[144] The saline and stabilization molecule method for controlled aggregation was extended to fit larger GNSs and proven to be temporally and thermally stable during heating. Although DNA linking is another widely applied method to study GNP aggregation for large size, customized uniform aggregation shapes, it has a major drawback in poor thermal stability.[145] The saline method was able to fix the aggregation during the laser heating. In the laser calorimetry experiment, low NaCl samples did not show a rapid drop in heating as the modelled dimers and trimers. However, the trend of these experimental data is very similar to the numerical

data if the single GNS case is taken out. We believe this outcome is mainly caused by the heating deficit of monodispersed control GNS rather than the surplus of aggregated GNS samples. Since the Maxwell Garnett effect's condition is $d \leq 5R$, the control solution we tested may not be optically thin enough to totally avoid its influence. This is important, because the *SAR* in biomedical applications is oftentimes estimated with the optical properties of isolated GNPs that is likely to result in an overestimation even for non-aggregated conditions. For the range of GNP concentration, size and aggregation size we tested, aggregation does affect the photothermal heating outcome. It is worth mentioning that further decrease in GNS optical extinction has been measured with increasing of aggregation size by other groups.[12,145] Thus, we suggest taking 15-28% deduction from the heating calculated by isolated GNSs when evaluating the heat source in real application counting for the aggregation effect.

Our study suggests the aggregation affects GNS photothermal heating in a very complicated way. Besides estimating the real heating in a biomedical application, it may inspire the design of GNS photothermal systems and new GNPs. For instance, per a certain amount of gold, using as single large GNS is preferred in heating rather than a cluster of smaller GNSs. Also, isolating individual GNPs may improve the photothermal heating (e.g. adding a silica coating layer) by increasing the inter-particle distance and avoiding aggregation as dimers and trimers are experimentally difficult to avoid. This may be particularly important for GNPs of more complicated geometries, such as gold nanorods. It then leads to the need for better understanding in collective

effect when reporting a new photothermal nanoheater since the heating outcome is highly affected by the distribution states (i.e. polydispersity and aggregation). In addition, this work provides a framework that could be applied in quantitative characterization of photothermal applications of other simple or complex nanostructures. For future studies, we will measure the quantitative GNP photothermal heating in more complicated biosystems (e.g. cultured cells, embryos and tumors). Numerical and experimental work on aggregation's effect with other GNPs such as gold nanorods will also be performed.

6.4 Conclusions

We studied the photothermal heating of gold nanospheres numerically and experimentally for a wide size range. Discrete dipole approximation and calibrated cuvette calorimetry were used in the study. 15-28% decrease in heat generation was calculated with aggregated GNSs comparing to isolated single particles in the size range 16 to 30 nm. It may help predict the outcome of a GNP photothermal application more precisely if taken heating loss by GNP aggregation into consideration. Our data also shows the effect of aggregation works quite differently with GNS size, aggregation size and shape. This work provides a general framework to understanding the impact of aggregation on laser heating of aggregated nanostructures.

Chapter 7 Conclusions and Future Directions

In this dissertation, I first introduced the photothermal heating of GNPs in biomedicine and numerical and experimental tools to measure it, including our integrating sphere spectrophotometer laser calorimetry methods. Then the two methods were applied in charactering the Thermal Contrast Amplification reader and the effect of GNS aggregation for photothermal heating. Moreover, the TCA reader was validated in a clinical study in strep throat diagnosis; the optimized parameters, algorithm and components were also prepared for the next generation TCA reader. Along with the applications of GNP photothermal heating introduced in this dissertation, the foundations of future work were also been laid for the following:

7.1 Larger scale clinical trials of TCA reader

The next generation TCA reader would be small to size, portable, and with high efficiency and throughput. It would be suitable in a clinician's office (and other point-of-care settings) to test the fresh LFA samples from patients. Clinical trials of such devices used in point-of-care settings would provide more precise and a larger volume of data than our strep throat study and help move the device toward commercialization.

7.2 Next generation TCA specific LFAs

Our optical-thermal modeling results of the TCA suggest some key features for the next generation of LFAs: low scattering/absorbing lateral flow membrane for higher contrast, no

backing layer or an insulated backing layer for less heat loss. These could be combined with another study by our lab[107] for high LFA sensitivity by engineering the GNPs and together lead to new TCA-LFA for optimal performance.

7.3 Characterizing other GNP-laden systems with our measurement methods

a. GNR laden zebra fish embryos

A rapid warming rate (>10^7 °C/min) is necessary in the laser assisted GNR warming to achieve successful zebrafish embryo cryopreservation. The estimation of this warming rate and any optimization of parameters (GNP dose, cryoprotectants, pulse duration, thermal stress, etc.) are dependent on the knowledge of the precise heat generation of the embryo. The C_{abs} of the GNR and an equivalent absorption cross section caused by other heat sources (absorption by water, embryo material, and cryoprotectants) could be measured with the cuvette laser calorimetry. We have finished the system setup and characterization and calibrating with the 1064 nm laser (~200 mW). The heating of 1064 resonance GNRs has been characterized and published (see Appendix C).

To perform these measurements, several GNP samples will be provided by the manufacturer (nanoComposix Inc.) (Fig.7.1) including gold nanorods (12 nm x 100 nm), hollow gold nanoshells (180 nm) and silica core/gold shell nanoshells (200 nm core, 12 nm shell). TEM, DLS, and UV-Vis-NIR characterization of samples will be conducted. The concentration of the GNR solution need be checked by ICP-OES measurement which is available in the

Research Analytical Laboratory on St. Paul Campus of the University of Minnesota. The same concentration of GNP solutions will be measured. More cases need to be designed to study the performance of these particles in an embryo.

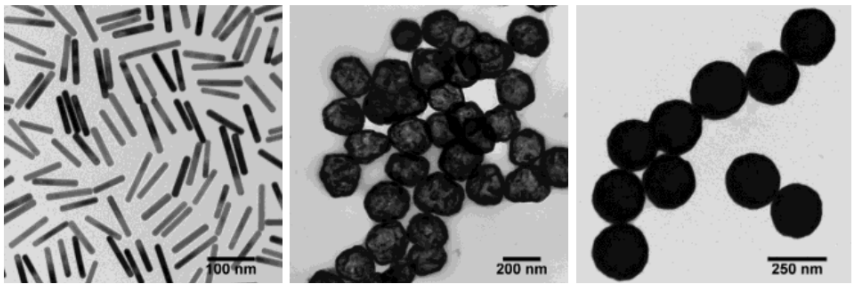

Figure 7.1. Transmission electron microscope (TEM) images of gold nanorods, hollow gold nanoshells, and silica-core gold nanoshells (left to right) with plasmon resonances near 1064 nm (by nanoComposix, product details).

b. GNP-laden tumor tissues

The characterization of tumor tissue photothermal heating could help control the thermal ablation doses, especially for the cases where the surrounding tissues are very sensitive to heat, such as brain tumor. The measurement could be done with both methods; i.e. the cuvette laser calorimetry would provide the real heating results of a small amount of tissue and the integrating sphere spectrophotometer would provide the necessary optical properties for the modeling.

c. Aggregation effects in differently shaped GNPs

Chapter 6 provides the frame work to characterize GNP's aggregation. We have known that GNR heating is more sensitive to size polydispersity (70% decrease in heating for 20%

polydispersity). Such aggregation could be an important factor in heating deficits in GNR systems. The same may be true for other complicated GNPs/GNP composites such as gold nanostar, gold nanorice ant etc.

Bibliography

1 P. Ghosh, G. Han, M. De and C. K. Kim, *Adv. Drug Deliv. Rev.*, 2008, **60**, 1307–1315.

2 R. Shukla, V. Bansal, M. Chaudhary, A. Basu, R. R. Bhonde and M. Sastry, *Langmuir*, 2005, **21**, 10644–10654.

3 C. Burda, X. Chen, R. Narayanan and M. A. El-Sayed, *Chem. Rev.*, 2005, **105**, 1025–1102.

4 M. Grzelczak, J. Pérez-Juste, P. Mulvaney and L. M. Liz-Marzán, *Chem. Soc. Rev.*, 2008, **37**, 1783.

5 C. J. Murphy, T. K. Sau, A. M. Gole, C. J. Orendorff, J. Gao, L. Gou, S. E. Hunyadi and T. Li, *J. Phys. Chem. B*, 2005, **109**, 13857–13870.

6 Y. Sun and Y. Xia, *Science (80-.).*, 2002, **298**, 2176–2179.

7 R. Wilson, *Chem. Soc. Rev.*, 2008, **37**, 2028.

8 J.-M. Nam, C. S. Thaxton and C. A. Mirkin, *Science*, 2003, **301**, 1884–1886.

9 W. C. W. Chan and S. Nie, *Science (80-.).*, 1998, **281**, 2016–2018.

10 E. Boisselier and D. Astruc, *Chem. Soc. Rev.*, 2009, **38**, 1759.

11 Z. Qin and J. C. Bischof, *Chem. Soc. Rev.*, 2012, **41**, 1191–217.

12 N. T. Kim Thanh and Z. Rosenzweig, *Anal. Chem.*, 2002, **74**, 1624–1628.

13 G. A. Posthuma-Trumpie, J. Korf and A. van Amerongen, *Anal. Bioanal. Chem.*, 2009, **393**, 569–82.

14 K. Cho, X. Wang, S. Nie, Z. G. Chen and D. M. Shin, *Clin. Cancer Res.*, 2008, **14**, 1310–6.

15 L. R. Hirsch, R. J. Stafford, J. A. Bankson, S. R. Sershen, B. Rivera, R. E. Price, J. D. Hazle, N. J. Halas and J. L. West, *Proc. Natl. Acad. Sci.*, 2003, **100**, 13549–13554.

16 Z. Qin, Y. Wang, J. Randrianalisoa, V. Raeesi, W. C. W. Chan, W. Lipiński and J. C. Bischof, *Sci. Rep.*, 2016, **6**, 29836.

17 E. C. Dreaden, A. M. Alkilany, X. Huang, C. J. Murphy and M. A. El-Sayed, *Chem. Soc. Rev.*, 2012, **41**, 2740–2779.

18 B. D. Chithrani, A. A. Ghazani and W. C. W. Chan, *Nano Lett.*, 2006, **6**, 662–668.

19 J. Rejman, V. Oberle, I. S. Zuhorn and D. Hoekstra, *Biochem. J.*, 2004, **377**, 159–69.

20 S. D. Perrault, C. Walkey, T. Jennings, H. C. Fischer and W. C. W. Chan, *Nano Lett.*, 2009, **9**, 1909–1915.

21 N. Lewinski, V. Colvin and R. Drezek, *Small*, 2008, **4**, 26–49.

22 P. K. Jain, K. S. Lee, I. H. El-Sayed and M. A. El-Sayed, *J. Phys. Chem. B*, 2006, **110**, 7238–48.

23 S. W. Prescott and P. Mulvaney, *J. Appl. Phys.*, 2006, **99**, 123504.

24 E. Stefan Kooij and B. Poelsema, *Phys. Chem. Chem. Phys.*, 2006, **8**, 3349.

25 G. Baffou, R. Quidant and C. Girard, *Appl. Phys. Lett.*, 2009, **94**, 153109.

26 S. Kessentini and D. Barchiesi, *Biomed. Opt. Express*, 2012, **3**, 590–604.

27 H. Chen, L. Shao, T. Ming, Z. Sun, C. Zhao, B. Yang and J. Wang, *Small*, 2010, **6**, 2272–2280.
28 H. H. Richardson, M. T. Carlson, P. J. Tandler, P. Hernandez and A. O. Govorov, *Nano Lett.*, 2009, **9**, 1139–1146.
29 L. M. Maestro, E. Camarillo, J. A. Sánchez-Gil, R. Rodríguez-Oliveros, J. Ramiro-Bargueño, A. J. Caamaño, F. Jaque, J. G. Solé and D. Jaque, *RSC Adv.*, 2014, **4**, 54122–54129.
30 L. M. Maestro, P. Haro-González, A. Sánchez-Iglesias, L. M. Liz-Marzán, J. García Solé and D. Jaque, *Langmuir*, 2014, **30**, 1650–1658.
31 E. C. Cho, C. Kim, F. Zhou, C. M. Cobley, K. H. Song, J. Chen, Z.-Y. Li, L. V. Wang and Y. Xia, *J. Phys. Chem. C*, 2009, **113**, 9023–9028.
32 C. F. Bohren and D. R. Huffman, *Absorption and Scattering of Light by Small Particles*, John Wiley & Sons, 2008.
33 C. Ungureanu, R. G. Rayavarapu, S. Manohar and T. G. van Leeuwen, *J. Appl. Phys.*, 2009, **105**, 102032.
34 D. K. Roper, W. Ahn and M. Hoepfner, *J. Phys. Chem. C*, 2007, **111**, 3636–3641.
35 A. W. H. Lin, N. A. Lewinski, J. L. West, N. J. Halas and R. A. Drezek, *J. Biomed. Opt.*, 2005, **10**, 064035.
36 M. Kirillin, M. Shirmanova, M. Sirotkina, M. Bugrova, B. Khlebtsov and E. Zagaynova, *J. Biomed. Opt.*, 2009, **14**, 021017.
37 A. J. Welch and M. J. C. Van Gemert, *Optical-Thermal Response of Laser-Irradiated Tissue*, Springer Science & Business Media, 2nd edn., 2011.
38 L. Wang and S. L. Jacques, *Med. Phys.*, 1994, **21**, 1081–1083.
39 S. L. Jacques, in *Optical-Thermal Response of Laser-Irradiated Tissue*, Springer Netherlands, Dordrecht, 2010, pp. 109–144.
40 L. Wang, S. L. Jacques and L. Zheng, *Comput. Methods Programs Biomed.*, 1995, **47**, 131–146.
41 L. Wang, S. L. Jacques and L. Zheng, *Comput. Methods Programs Biomed.*, 1997, **54**, 141–50.
42 X. Wang, G. Li, Y. Ding and S. Sun, *RSC Adv.*, 2014, **4**, 30375.
43 A. Brioude, X. C. Jiang and M. P. Pileni, *J. Phys. Chem. B*, 2005, **109**, 13138–13142.
44 Z. Qin, W. C. W. Chan, D. R. Boulware, T. Akkin, E. K. Butler and J. C. Bischof, *Angew. Chemie - Int. Ed.*, 2012, **51**, 4358–4361.
45 J. Chen, F. Saeki, B. J. Wiley, H. Cang, M. J. Cobb, Z.-Y. Li, L. Au, H. Zhang, M. B. Kimmey, *,‡ and Li and Y. Xia, *Nano Lett.*, 2005, **5**, 473–477.
46 P. Yager, G. J. Domingo and J. Gerdes, *Annu. Rev. Biomed. Eng.*, 2008, **10**, 107–144.
47 C. M. Surawicz, L. J. Brandt, D. G. Binion, A. N. Ananthakrishnan, S. R. Curry, P. H. Gilligan, L. V McFarland, M. Mellow and B. S. Zuckerbraun, *Am. J. Gastroenterol.*, 2013,

108, 478–98; quiz 499.

48 P. J. Gavin and R. B. Thomson, *Clin. Appl. Immunol. Rev.*, 2003, **4**, 151–172.

49 C. Wongsrichanalai, M. J. Barcus, S. Muth, A. Sutamihardja and W. H. Wernsdorfer, *Am. J. Trop. Med. Hyg.*, 2007, **77**, 119–127.

50 J. M. Klostranec, Q. Xiang, G. A. Farcas, J. A. Lee, A. Rhee, E. I. Lafferty, S. D. Perrault, K. C. Kain and W. C. W. Chan, *Nano Lett.*, 2007, **7**, 2812–8.

51 T. Laksanasopin, T. W. Guo, S. Nayak, A. A. Sridhara, S. Xie, O. O. Olowookere, P. Cadinu, F. Meng, N. H. Chee, J. Kim, C. D. Chin, E. Munyazesa, P. Mugwaneza, A. J. Rai, V. Mugisha, A. R. Castro, D. Steinmiller, V. Linder, J. E. Justman, S. Nsanzimana and S. K. Sia, *Sci. Transl. Med.*, 2015, **7**, 273re1.

52 Geneva: World Helath Organization, *Summ. results WHO Prod. Test. Malar. RDTs Round 1–5*.

53 O. Gaye, M. Diouf and S. Diallo, *Parasite*, 2014, **6**, 273–275.

54 X. Ge, A. M. Asiri, D. Du, W. Wen, S. Wang and Y. Lin, *TrAC Trends Anal. Chem.*, 2014, **58**, 31–39.

55 M. Ren, H. Xu, X. Huang, M. Kuang, Y. Xiong, H. Xu, Y. Xu, H. Chen and A. Wang, *ACS Appl. Mater. Interfaces*, 2014, **6**, 14215–22.

56 H. Xu, J. Chen, J. Birrenkott, J. X. Zhao, S. Takalkar, K. Baryeh and G. Liu, *Anal. Chem.*, 2014, **86**, 7351–9.

57 M. Li, H. Yang, S. Li, K. Zhao, J. Li, D. Jiang, L. Sun and A. Deng, *J. Agric. Food Chem.*, 2014, **62**, 10896–902.

58 M. R. Akanda, H.-A. Joung, V. Tamilavan, S. Park, S. Kim, M. H. Hyun, M.-G. Kim and H. Yang, *Analyst*, 2014, **139**, 1420–5.

59 X. Zhu, P. Shah, S. Stoff, H. Liu and C. Li, *Analyst*, 2014, **139**, 2850–7.

60 Y. Y. Lin, J. Wang, G. Liu, H. Wu, C. M. Wai and Y. Lin, *Biosens. Bioelectron.*, 2008, **23**, 1659–1665.

61 Y. Bai, C. Tian, X. Wei, Y. Wang, D. Wang and X. Shi, *RSC Adv.*, 2012, **2**, 1778.

62 C. Zheng, X. Wang, Y. Lu and Y. Liu, *Food Control*, 2012, **26**, 446–452.

63 J. M. Barnett, P. Wraith, J. Kiely, R. Persad, K. Hurley, P. Hawkins and R. Luxton, *Biosensors*, 2014, **4**, 204–220.

64 S. Workman, S. K. Wells, C.-P. Pau, S. M. Owen, X. F. Dong, R. LaBorde and T. C. Granade, *J. Virol. Methods*, 2009, **160**, 14–21.

65 C. Parolo, A. de la Escosura-Muñiz and A. Merkoçi, *Biosens. Bioelectron.*, 2013, **40**, 412–6.

66 C. Liu, Q. Jia, C. Yang, R. Qiao, L. Jing, L. Wang, C. Xu and M. Gao, *Anal. Chem.*, 2011, **83**, 6778–84.

67 D. R. Boulware, M. A. Rolfes, R. Rajasingham, M. von Hohenberg, Z. Qin, K. Taseera, C. Schutz, R. Kwizera, E. K. Butler, G. Meintjes, C. Muzoora, J. C. Bischof and D. B. Meya,

Emerg. Infect. Dis., 2014, **20**, 45–53.

68 A. Peci, A.-L. Winter, E.-C. King, J. Blair and J. B. Gubbay, *J. Clin. Microbiol.*, 2014, **52**, 4309–17.

69 W. M. Stauffer, C. P. Cartwright, D. A. Olson, B. A. Juni, C. M. Taylor, S. H. Bowers, K. L. Hanson, J. E. Rosenblatt and D. R. Boulware, *Clin. Infect. Dis.*, 2009, **49**, 908–13.

70 C. G. Diagnoses, *PLoS Med.*, , DOI:10.1371/journal.pmed.1000396 <http://dx.doi.org/10.1371/journal.pmed.1000396>.

71 G. L. Long and J. D. Winefordner, *Anal. Chem.*, 1983, **55**, 712A–724A.

72 D. A. Armbruster and T. Pry, *Clin. Biochem. Rev.*, 2008, **29**, S49-52.

73 H.-P. Loock and P. D. Wentzell, *Sensors Actuators B Chem.*, 2012, **173**, 157–163.

74 L. Wang, D. Lu, J. Wang, D. Du, Z. Zou, H. Wang, J. N. Smith, C. Timchalk, F. Liu and Y. Lin, *Biosens. Bioelectron.*, 2011, **26**, 2835–40.

75 L. Shi, F. Wu, Y. Wen, F. Zhao, J. Xiang and L. Ma, *Anal. Bioanal. Chem.*, 2015, **407**, 529–535.

76 Y. Wang, H. Xu, M. Wei, H. Gu, Q. Xu and W. Zhu, *Mater. Sci. Eng. C*, 2009, **29**, 714–718.

77 Q. Y. Xie, Y. H. Wu, Q. R. Xiong, H. Y. Xu, Y. H. Xiong, K. Liu, Y. Jin and W. H. Lai, *Biosens. Bioelectron.*, 2014, **54**, 262–265.

78 S. Workman, S. K. Wells, C.-P. Pau, S. M. Owen, X. F. Dong, R. LaBorde and T. C. Granade, *J. Virol. Methods*, 2009, **160**, 14–21.

79 W. Qiu, H. Xu, S. Takalkar, A. S. Gurung, B. Liu, Y. Zheng, Z. Guo, M. Baloda, K. Baryeh and G. Liu, *Biosens. Bioelectron.*, 2015, **64**, 367–72.

80 A. J. Saah and D. R. Hoover, *Ann. Intern. Med.*, 1997, **126**, 91–94.

81 A. K. Akobeng, *Acta Paediatr.*, 2007, **96**, 338–341.

82 S. Yang and R. E. Rothman, *Lancet Infect. Dis.*, 2004, **4**, 337–348.

83 C. D. Brown and H. T. Davis, *Chemom. Intell. Lab. Syst.*, 2006, **80**, 24–38.

84 D. E. Noyola and G. J. Demmler, *Pediatr. Infect. Dis. J.*, 2000, **19**, 303–7.

85 A. R. Falsey, Y. Murata and E. E. Walsh, *Arch. Intern. Med.*, 2007, **167**, 354–360.

86 J. F. Cohen, R. Cohen and M. Chalumeau, in *Cochrane Database of Systematic Reviews*, ed. M. Chalumeau, John Wiley & Sons, Ltd, Chichester, UK, 2013.

87 W. Scheychon, Leibniz Universität Hannover, 2012.

88 J. M. Khosrofian and B. A. Garetz, *Appl. Opt.*, 1983, **22**, 3406.

89 J. M. Khosrofian and B. A. Garetz, *Appl. Opt.*, 1983, **22**, 3406.

90 J. R. Carapetis, A. C. Steer, E. K. Mulholland and M. Weber, *Lancet Infect. Dis.*, 2005, **5**, 685–694.

91 J. N. Cole, T. C. Barnett, V. Nizet and M. J. Walker, *Nat. Rev. Microbiol.*, 2011, **9**, 724–736.

92 M. H. Ebell, M. A. Smith, H. C. Barry, K. Ives and M. Carey, *JAMA*, 2000, **284**, 2912.

93 K. E. Gieseker, M. H. Roe, T. MacKenzie and J. K. Todd, *Pediatrics*.

94 R. E. O'Loughlin, A. Roberson, P. R. Cieslak, R. Lynfield, K. Gershman, A. Craig, B. A.

Albanese, M. M. Farley, N. L. Barrett, N. L. Spina, B. Beall, L. H. Harrison, A. Reingold and C. V. Beneden, *Clin. Infect. Dis.*, 2007, **45**, 853–862.

95 S. T. Shulman, A. L. Bisno, H. W. Clegg, M. A. Gerber, E. L. Kaplan, G. Lee, J. M. Martin and C. Van Beneden, *Clin. Infect. Dis.*, , DOI:10.1093/cid/cis629.

96 P. Yager, G. J. Domingo and J. Gerdes, *Annu. Rev. Biomed. Eng.*, 2008, **10**, 107–44.

97 M. A. Gerber and S. T. Shulman, *Clin. Microbiol. Rev.*, 2004, **17**, 571–80, table of contents.

98 A. D. Camurdan, O. M. Camurdan, I. Ok, F. Sahin, M. N. Ilhan and U. Beyazova, *Int. J. Pediatr. Otorhinolaryngol.*, 2008, **72**, 1203–1206.

99 O. Santos, L. L. M. Weckx, A. C. C. Pignatari and S. S. N. Pignatari, *Brazilian J. Infect. Dis.*, 2003, **7**, 297–300.

100 A. L. Bisno, M. A. Gerber, J. M. Gwaltney, Jr., E. L. Kaplan and R. H. Schwartz, *Clin. Infect. Dis.*, 35, 113–125.

101 M. L. Alcaide and A. L. Bisno, *Infect. Dis. Clin. North Am.*, 2007, **21**, 449–469.

102 R. H. Barker, *Parasitol. Today*, 1994, **10**, 117–119.

103 GasDirect test | Hologic, http://www.hologic.ca/package-inserts/clinical-diagnostics/assays-and-tests/GasDirect-test, (accessed 31 July 2018).

104 J. W. Fox, D. M. Cohen, M. J. Marcon, W. H. Cotton and B. K. Bonsu, *J. Clin. Microbiol.*, 2006, **44**, 3918–22.

105 A. K. Jarmusch, V. Pirro, K. S. Kerian and R. G. Cooks, *Analyst*, 2014, **139**, 4785–4789.

106 Y. Wang, Z. Qin, D. R. Boulware, B. S. Pritt, L. M. Sloan, I. J. González, D. Bell, R. R. Rees-Channer, P. Chiodini, W. C. W. Chan and J. C. Bischof, *Anal. Chem.*, 2016, **88**, 11774–11782.

107 L. Zhan, S. Guo, F. Song, Y. Gong, F. Xu, D. R. Boulware, M. C. McAlpine, W. C. W. Chan and J. C. Bischof, *Nano Lett.*, 2017, **17**, 7207–7212.

108 G. FRENS, *Nat. Phys. Sci.*, 1973, **241**, 20–22.

109 M. Khayet, A. Velá zquez and J. I. Mengual, *J. Non-Equilib. Thermodyn. Á*, 2004, **29**, 279–299.

110 C. A. Harper, *Handbook of Plastics Elastomers, and Composites*, New York: McGraw-Hill, 1992.

111 J. E. Mark, *Physical Properties of Polymers Handbook*, New York: Springer, 2007.

112 G. M. Brauer and E. Horowitz, *Analytical Chemistry of Polymers, part III*, John Wiley & Sons, 1962.

113 M. Idicula, A. Boudenne, L. Umadevi, L. Ibos, Y. Candau and S. Thomas, *Compos. Sci. Technol.*, 2006, **66**, 2719–2725.

114 S. Yu, P. Hing and X. Hu, *Compos. Part A Appl. Sci. Manuf.*, 2002, **33**, 289–292.

115 U. Gaur and B. Wunderlich, *J. Phys. Chem. Ref. Data*, 1982, **11**, 313–325.

116 J. C. Bischof and K. R. Diller, *Annu. Rev. Biomed. Eng.*, 2018, **20**, 301–327.

117 L. Dykman and N. Khlebtsov, *Chem. Soc. Rev.*, 2012, **41**, 2256–2282.

118 Y. Cheng, A. C. Samia, J. D. Meyers, I. Panagopoulos, B. Fei and C. Burda, *J. Am. Chem. Soc.*, 2008, **130**, 10643–10647.
119 A. Albanese and W. C. W. Chan, *ACS Nano*, 2011, **5**, 5478–5489.
120 K. Khosla, L. Zhan, A. Bhati, A. Carley-Clopton, M. Hagedorn and J. Bischof, *Langmuir*, 2018, acs.langmuir.8b03011.
121 K. Khosla, Y. Wang, M. Hagedorn, Z. Qin and J. Bischof, *ACS Nano*, 2017, **11**, 7869–7878.
122 M. Mathiyazhakan, C. Wiraja and C. Xu, *Nano-Micro Lett.*, 2018, **10**, 10.
123 J. Tan, T. J. Cho, D.-H. Tsai, J. Liu, J. M. Pettibone, R. You, V. A. Hackley and M. R. Zachariah, *Langmuir*, 2018, **34**, 154–163.
124 M. Borzenkov, G. Chirico, M. Collini and P. Pallavicini, Springer, Cham, 2018, pp. 343–390.
125 V. P. Zharov, K. E. Mercer, E. N. Galitovskaya and M. S. Smeltzer, *Biophys. J.*, 2006, **90**, 619–627.
126 R. Sean Norman, J. W. Stone, A. Gole, C. J. Murphy and T. L. Sabo-Attwood, *Nano Lett.*, 2008, **8**, 302–306.
127 T. C. Pagonis, J. Chen, C. R. Fontana, H. Devalapally, K. Ruggiero, X. Song, F. Foschi, J. Dunham, Z. Skobe, H. Yamazaki, R. Kent, A. C. R. Tanner, M. M. Amiji and N. S. Soukos, *J. Endod.*, 2010, **36**, 322–328.
128 M. Nazari, M. Xi, S. Lerch, M. H. Alizadeh, C. Ettinger, H. Akiyama, C. Gillespie, S. Gummuluru, S. Erramilli and B. M. Reinhard, *Sci. Rep.*, 2017, **7**, 11951.
129 P. Kang, Z. Chen, S. O. Nielsen, K. Hoyt, S. D'Arcy, J. J. Gassensmith and Z. Qin, *Small*, 2017, **13**, 1700841.
130 F. Hao and P. Nordlander, *Chem. Phys. Lett.*, 2007, **446**, 115–118.
131 K. Zagorovsky and W. C. W. Chan, *Angew. Chemie Int. Ed.*, 2013, **52**, 3168–3171.
132 M. L. Etheridge, K. R. Hurley, J. Zhang, S. Jeon, H. L. Ring, C. Hogan, C. L. Haynes, M. Garwood and J. C. Bischof, *TECHNOLOGY*, 2014, **02**, 214–228.
133 S. Jeon, K. R. Hurley, J. C. Bischof, C. L. Haynes and C. J. Hogan, *Nanoscale*, 2016, **8**, 16053–16064.
134 G. Baffou, R. Quidant and F. J. García de Abajo, *ACS Nano*, 2010, **4**, 709–716.
135 J. Randrianalisoa, X. Li, M. Serre and Z. Qin, *Adv. Opt. Mater.*, 2017, **5**, 1700403.
136 V. S. Godakhindi, P. Kang, M. Serre, N. A. Revuru, J. M. Zou, M. R. Roner, R. Levitz, J. S. Kahn, J. Randrianalisoa and Z. Qin, *ACS Sensors*, 2017, **2**, 1627–1636.
137 S. K. Friedlander and D. Smoke, *Haze: Fundamentals of Aerosol Dynamics*, Oxford University Press, 2000.
138 A. V. Filippov, M. Zurita and D. E. Rosner, *J. Colloid Interface Sci.*, 2000, **229**, 261–273.
139 D. W. Mackowski, *Appl. Opt.*, 1995, **34**, 3535.
140 B. T. Draine and P. J. Flatau, *J. Opt. Soc. Am. A*, 1994, **11**, 1491.
141 S. K. Ghosh and T. Pal, *Chem. Rev.*, 2007, 107, 4797–4862.

142 J. C. Maxwell Garnett, *Philos. Trans. R. Soc.*, 1904, **203**, 805.
143 D. Vilela, M. C. González and A. Escarpa, *Anal. Chim. Acta*, 2012, 751, 24–43.
144 A. N. Shipway, M. Lahav, R. Gabai and I. Willner, *Langmuir*, 2000, **16**, 8789–8795.
145 J. J. Storhoff, A. A. Lazarides, R. C. Mucic, C. A. Mirkin, R. L. Letsinger and G. C. Schatz, *J. Am. Chem. Soc.*, 2000, **122**, 4640–4650.

Appendix A

MATLAB code for quantitative data analysis of TCA reader

This appendix includes an example of quantitative analysis of TCA reading results. The temperature rise score output by the LabVIEW control program will be further analyzed here to get a thermal signal. Clinical strep throat LFAs by Quidel is taken as an example. The total reading length of this LFA is 7 mm, with 1 mm width control and test lines.

```
% Strep clinical LFAs. 53 data points in total. 52 valid in the txt
file.

clear;

cur_ts = textread(['/Users/yiruwang/Google Drive/UMN/Projects/TCR
developing/data analysis /1.txt']);
active_data(1,:) = cur_ts; %copy all the data points to the .txt file.
The last point will be lost.

% Find CL start point
for i = 1:51
    remain(1,i) = active_data(1,i+1)-active_data(1,i);
    i = i+1;
end

CL = 0;
for i = 2:20
    if remain(1,i)-1.5>=0
    CL = i;
    break
    else
        i = i+1;
    end
```

```
end

% Calculate AUC in 2 position and find the larger one
TL = CL+32; % TL is 33 points after CL

TL_X(1,:) = [1:12];
TL_Y(1,:) = [active_data(1,TL:TL+11)];

for i = 1:2
    background_X(i,:) = [1+i-1,2+i-1,10+i-1,11+i-1];
    background_Y(i,:) = [TL_Y(1+i-1),TL_Y(2+i-1),TL_Y(10+i-1),TL_Y(11+i-
1)];

    coefficients(i,:) = polyfit(background_X(i,:),background_Y(i,:),1);
    fitting_Y(i,:) = polyval(coefficients(i,:),linspace(1,9,9));
    plot(background_X(i,:),background_Y(i,:),'o')
    %axis([1 19 0 40])
    hold all;
    plot(fitting_Y(i,:),'x')

    residual(i,:) = TL_Y(1,4+i-1:8+i-1)-fitting_Y(i,i+3:i+7); % error
here: not the sum of the TL region.
    Score(i,1) = sum(residual(i,:))/7;
end

Score

plot(TL_Y)
```

Appendix B

Integrating sphere spectrophotometer measurement report

This appendix includes the major data and parameters in the report of the LFA membrane/GNP laden LFA membrane optical measurement prepared by Dr. Scott Prahl.

Abstract

Measurements were made by an EG&G PARC 1453A Silicon Photodiode Detector with the EG&G PARC 1462 Detector Controller Module operated by the EG&G PARC 1471A Detector Interface. The 1453A has 1024 pixels that are 25 by 2.5 microns on 25 micron centers for a total length of 25 mm. The dynamic range is 215 or 32,768. Typical sensitivity at 550 nm is 1160 photons/count.

The spectrometer is a Jarrel Ash MonoSpec 18 with a crossed Czerny-Turner optical design. The focal length is 156 mm and the aperture is F/3.8.

The detector was held at -20 C and the exposure time was 120 ms.

The original source files were acquired between Sun Jan 22, 2017 at 15:46:53 and Sun Jan 22, 2017 at 16:10:05.

1 General Experimental Conditions

Inverse Adding-Doubling 3-9-11 (4 Apr 2016)

Beam diameter	10.0 mm
Sample thickness	0.180 mm
Top slide thickness	0.000 mm
Bottom slide thickness	0.000 mm
Sample index of refraction	1.4500
Top slide index of refraction	1.0000
Bottom slide index of refraction	1.0000
Fraction unscattered refl. in M_R	100.0 %
Fraction unscattered trans. in M_T	100.0 %
Reflection sphere	
sphere diameter	203.2 mm
sample port diameter	19.1 mm
entrance port diameter	8.0 mm
detector port diameter	25.4 mm
wall reflectance	0.434–0.958 %
standard reflectance	0.980 %
detector reflectance	0.0 %
Transmission sphere	
sphere diameter	203.2 mm
sample port diameter	19.1 mm
entrance port diameter	19.1 mm
detector port diameter	25.4 mm
wall reflectance	0.434–0.958 %
standard transmittance	100.0 %
detector reflectance	0.0 %
AD quadrature points	8
AD tolerance for success	0.00010
MC tolerance for μ_a and μ_s'	0.010 %
Photons used to estimate lost light	0

2 Calibration Data

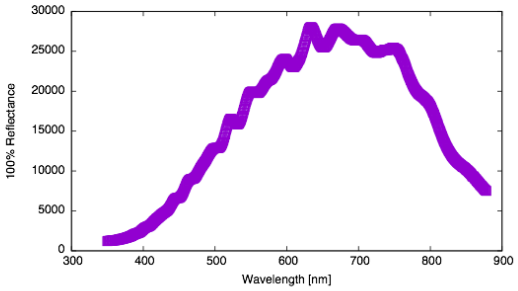

(a) 100% Reflectance.

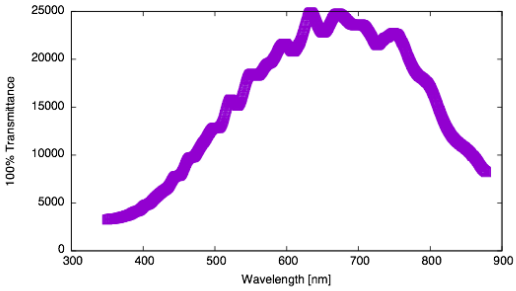

(b) 100% Transmittance.

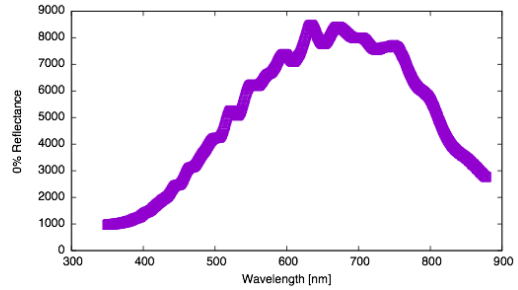

(c) 0% Reflectance.

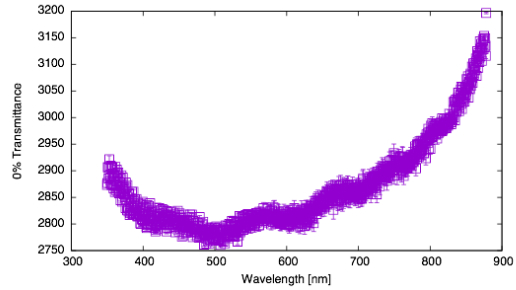

(d) 0% Transmittance.

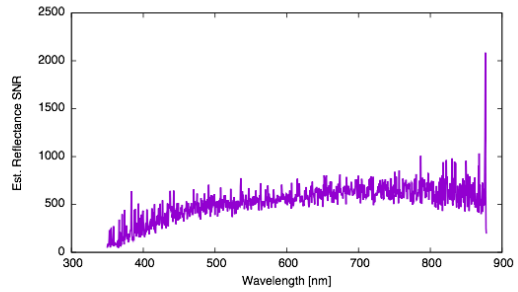

(e) Reflectance SNR

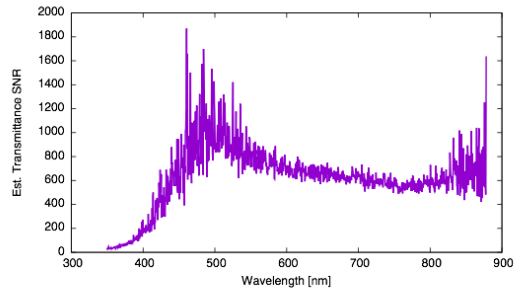

(f) Transmittance SNR

Figure 1: Reflection and Transmission Calibration Data. The SNR curves are approximated by $(M_{100} - M_0)/(2\Delta M_0)$ where ΔM_0 is the standard deviation of the 0% measurement.

3 Sample blank

The command-line conversion was `iad -V 1 -g 0.6 -M 0 <filename>`.

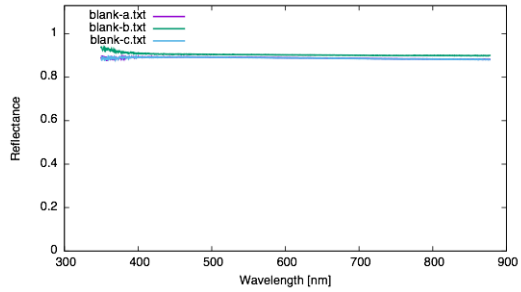

(a) Reflectance

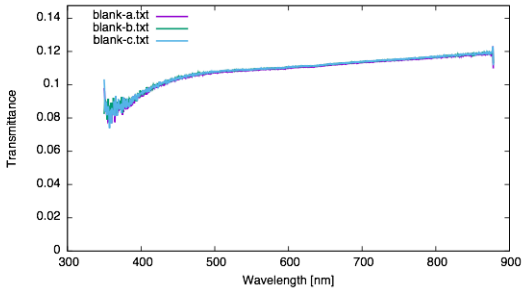

(b) Transmittance

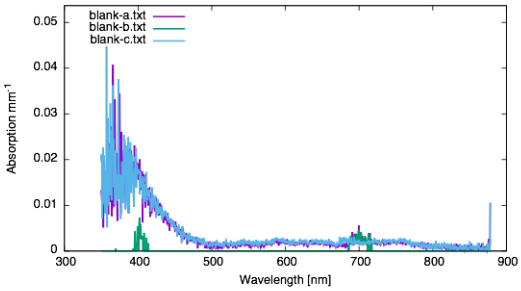

(c) Absorption

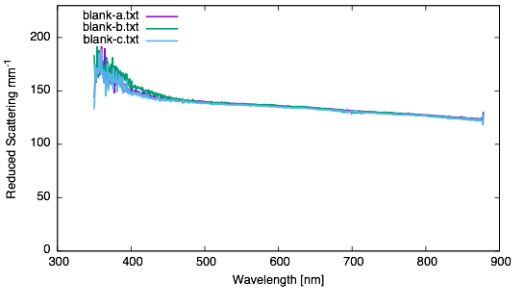

(d) Reduced Scattering

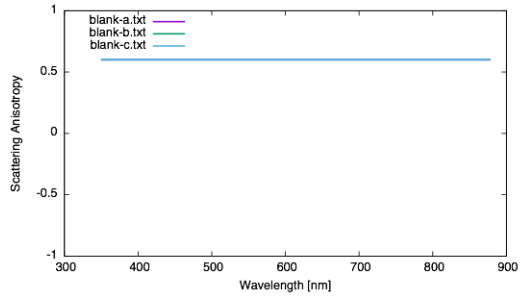

(e) Scattering Anisotropy

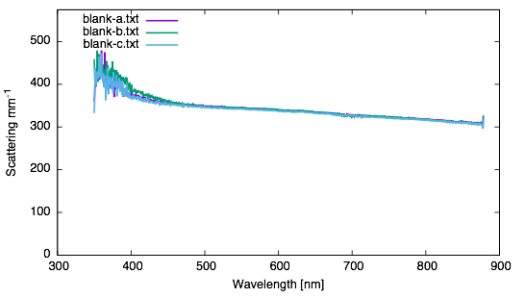

(f) Scattering

Figure 2: Summary of results for blank-a.txt, blank-b.txt, and blank-c.txt.

4 Sample onex

The command-line conversion was `iad -V 1 -g 0.6 -M 0 <filename>`.

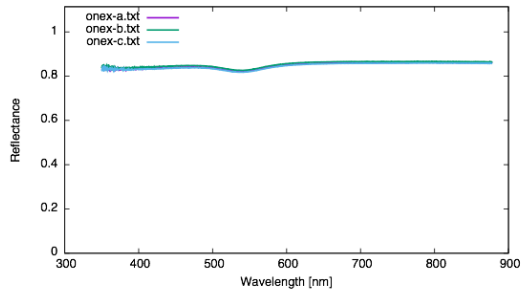

(a) Reflectance

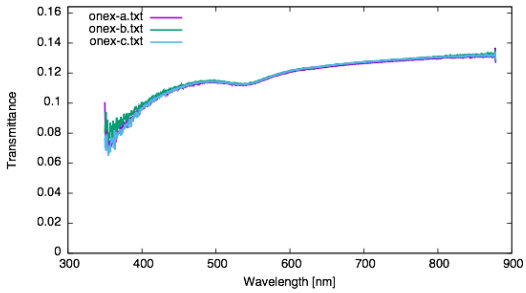

(b) Transmittance

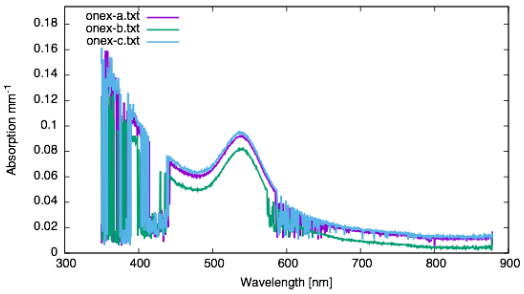

(c) Absorption

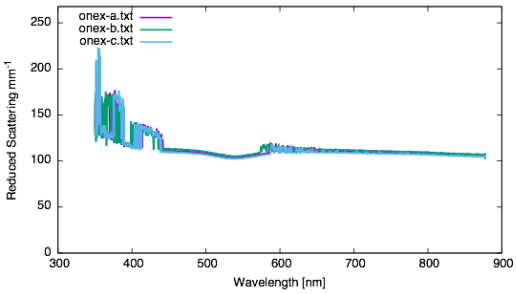

(d) Reduced Scattering

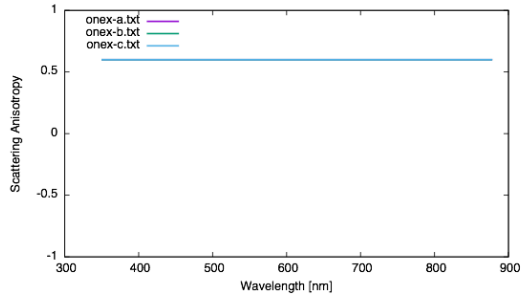

(e) Scattering Anisotropy

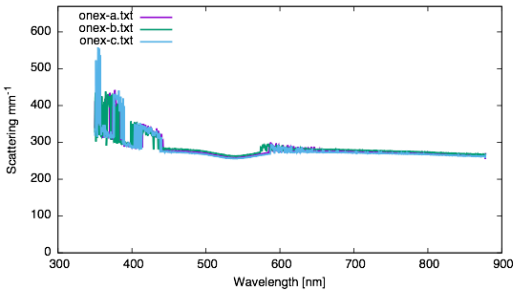

(f) Scattering

Figure 6: Summary of results for onex-a.txt, onex-b.txt, and onex-c.txt.

5 Sample twox

The command-line conversion was `iad -V 1 -g 0.6 -M 0 <filename>`.

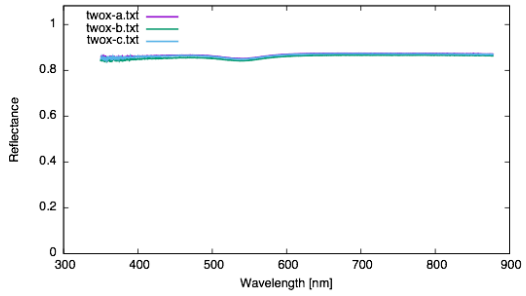

(a) Reflectance

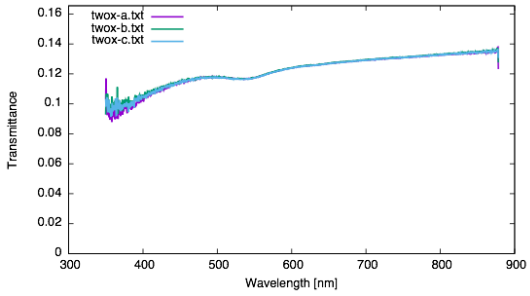

(b) Transmittance

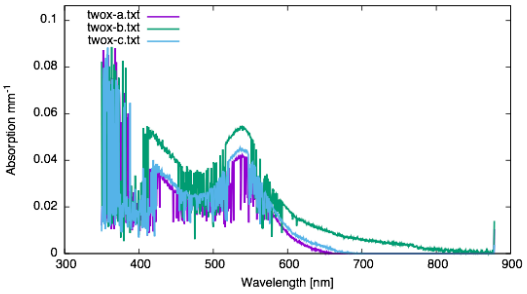

(c) Absorption

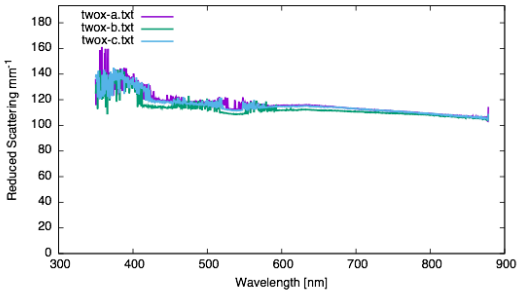

(d) Reduced Scattering

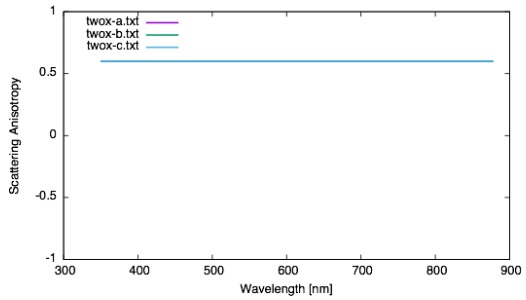

(e) Scattering Anisotropy

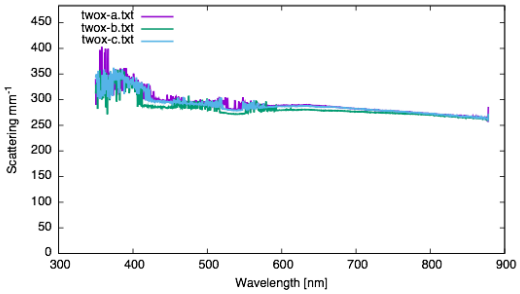

(f) Scattering

Figure 10: Summary of results for twox-a.txt, twox-b.txt, and twox-c.txt.

6 Summary Plots

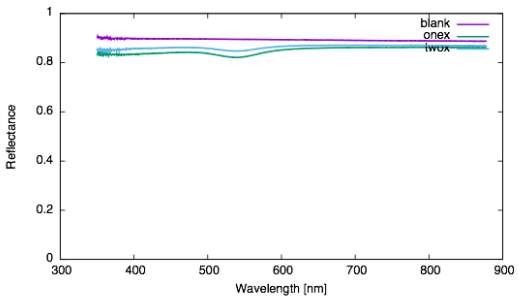

(a) Reflectance

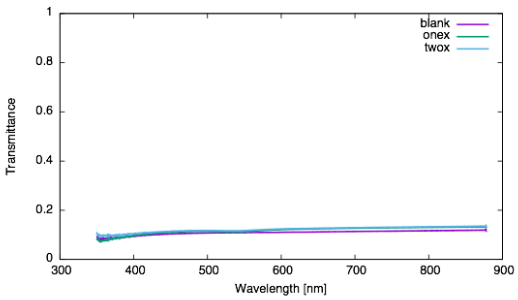

(b) Transmittance

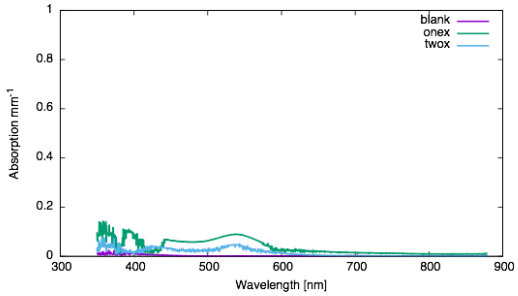

(c) Absorption

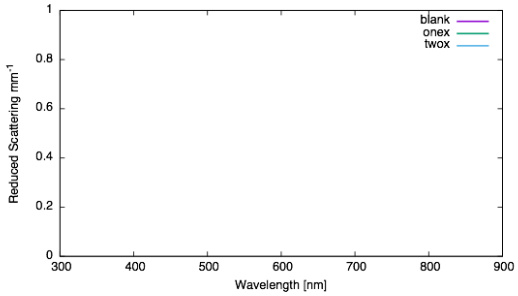

(d) Reduced Scattering

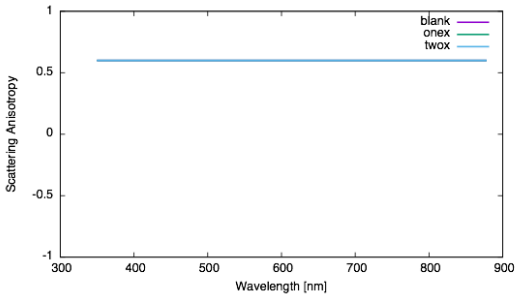

(e) Scattering Anisotropy

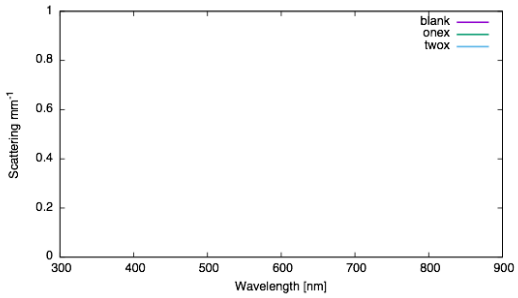

(f) Scattering

Figure 14: Representative files from the dataset.

7 Tabulated Optical Data

wave	blank μ_a	blank μ_s'	onex μ_a	onex μ_s'	twox μ_a	twox μ_s'
485.3	0.0015	139.9667	0.0581	109.7333	0.0206	117.8333
485.9	0.0015	139.8333	0.0589	109.5667	0.0233	116.7667
486.4	0.0015	139.9333	0.0588	109.5000	0.0232	117.0333
486.9	0.0011	139.7667	0.0584	109.6333	0.0276	115.5667
487.5	0.0014	139.9000	0.0586	109.4667	0.0265	115.7000
488	0.0010	139.7667	0.0587	109.7333	0.0209	117.6000
488.6	0.0015	139.7000	0.0595	109.3667	0.0232	116.5667
489.1	0.0014	139.5667	0.0589	109.4000	0.0240	116.6000
489.6	0.0015	139.5000	0.0595	109.3333	0.0212	117.4333
490.2	0.0011	139.4667	0.0596	109.2000	0.0227	116.6333
490.7	0.0012	139.3667	0.0597	109.2000	0.0244	116.4667
491.2	0.0006	139.8000	0.0590	109.3333	0.0245	116.3000
491.8	0.0009	139.9667	0.0603	109.0000	0.0228	116.9667
492.3	0.0012	139.7333	0.0603	109.2333	0.0240	116.6333
492.9	0.0012	139.3667	0.0599	109.1667	0.0267	115.3667
493.4	0.0012	139.6667	0.0608	109.0333	0.0180	119.0000
493.9	0.0007	139.6000	0.0604	108.9333	0.0230	116.7333
494.5	0.0009	139.4667	0.0605	108.7667	0.0254	115.9667
495	0.0006	139.8333	0.0607	108.9667	0.0225	117.2000
495.6	0.0010	139.5000	0.0612	108.8667	0.0262	115.6000
496.1	0.0009	139.2333	0.0613	108.9000	0.0252	116.0333
496.6	0.0011	139.4000	0.0614	108.8000	0.0252	116.1333
497.2	0.0013	139.0000	0.0620	108.4000	0.0276	115.3333
497.7	0.0006	139.3000	0.0617	108.5000	0.0242	116.5333
498.2	0.0009	139.2333	0.0625	108.2667	0.0213	117.4333
498.8	0.0009	139.1000	0.0624	108.3333	0.0276	115.1000
499.3	0.0007	139.1000	0.0629	108.4667	0.0187	118.4333
499.9	0.0010	138.9000	0.0638	108.2000	0.0169	118.8667
500.4	0.0012	138.8333	0.0633	108.3667	0.0289	115.0333
500.9	0.0011	138.8667	0.0639	108.1667	0.0277	115.5333
501.5	0.0008	139.1000	0.0643	108.3000	0.0309	114.2000
502	0.0007	139.2000	0.0650	108.2667	0.0249	116.4667
502.6	0.0010	138.7667	0.0653	107.7667	0.0192	118.1000
503.1	0.0010	138.7333	0.0653	107.6667	0.0307	114.5333
503.6	0.0011	139.0000	0.0665	107.8667	0.0213	117.5333
504.2	0.0009	139.0333	0.0663	107.7000	0.0267	115.7333
504.7	0.0008	138.9000	0.0667	107.6667	0.0263	115.9667
505.2	0.0006	139.1667	0.0666	107.6333	0.0251	116.5000
505.8	0.0008	138.7000	0.0678	107.6333	0.0257	116.1667
506.3	0.0011	138.5333	0.0684	107.2667	0.0218	117.5333
506.9	0.0011	138.7667	0.0684	107.3667	0.0284	115.2000
507.4	0.0007	138.9333	0.0686	107.1667	0.0263	116.1667
507.9	0.0010	138.5333	0.0689	107.2000	0.0283	115.5000

wave	blank μ_a	blank μ_s'	onex μ_a	onex μ_s'	twox μ_a	twox μ_s'
508.5	0.0009	138.3333	0.0698	107.0000	0.0227	117.2667
509	0.0007	138.6667	0.0697	107.0000	0.0253	116.4333
509.6	0.0009	138.5333	0.0709	106.9333	0.0283	115.5667
510.1	0.0008	138.4000	0.0709	106.7333	0.0235	117.2000
510.6	0.0007	138.7000	0.0716	106.7333	0.0235	117.1000
511.2	0.0007	138.3667	0.0718	106.6000	0.0257	116.3000
511.7	0.0007	138.5333	0.0721	106.5333	0.0303	115.0667
512.2	0.0007	138.5000	0.0727	106.5667	0.0265	116.2667
512.8	0.0010	138.4667	0.0736	106.4667	0.0376	112.8667
513.3	0.0009	138.2333	0.0740	106.3000	0.0314	114.6667
513.9	0.0006	138.5333	0.0746	106.3667	0.0275	116.1667
514.4	0.0006	138.4333	0.0747	106.1333	0.0244	117.2000
514.9	0.0006	138.4667	0.0753	106.1667	0.0290	115.6000
515.5	0.0006	138.3667	0.0758	106.1333	0.0244	117.2000
516	0.0013	138.0667	0.0762	105.9333	0.0191	119.4333
516.6	0.0008	138.2333	0.0762	106.0000	0.0272	116.8333
517.1	0.0008	138.5333	0.0770	105.9667	0.0320	115.2000
517.6	0.0009	138.1333	0.0779	105.7000	0.0342	114.4667
518.2	0.0012	138.5000	0.0781	105.7667	0.0377	113.3667
518.7	0.0009	138.2333	0.0783	105.5667	0.0314	115.4333
519.3	0.0013	138.4000	0.0789	105.5000	0.0413	112.3333
519.8	0.0013	138.2667	0.0799	105.4667	0.0353	114.2667
520.3	0.0009	138.4000	0.0800	105.3000	0.0333	114.7667
520.9	0.0008	138.5333	0.0803	105.3667	0.0419	112.2333
521.4	0.0010	138.4333	0.0817	105.0667	0.0366	113.9667
521.9	0.0007	138.6333	0.0814	105.4667	0.0379	113.8000
522.5	0.0007	138.3000	0.0817	105.1333	0.0364	114.0333
523	0.0010	138.2000	0.0819	104.9333	0.0401	112.7000
523.6	0.0009	138.4667	0.0827	104.8667	0.0372	113.7667
524.1	0.0008	138.1333	0.0827	105.0667	0.0349	114.7333
524.6	0.0009	138.1333	0.0832	104.8667	0.0369	114.0000
525.2	0.0010	138.2000	0.0840	104.8000	0.0427	112.0667
525.7	0.0011	138.1333	0.0845	104.6333	0.0437	111.7333
526.3	0.0013	137.8667	0.0848	104.7333	0.0439	111.7333
526.8	0.0010	138.3000	0.0850	104.6000	0.0442	111.6000
527.3	0.0009	137.9000	0.0846	104.4667	0.0357	114.2000
527.9	0.0010	137.9667	0.0857	104.4667	0.0448	111.5000
528.4	0.0006	138.0667	0.0858	104.4333	0.0447	111.5000
528.9	0.0007	137.7000	0.0862	104.2667	0.0447	111.4000
529.5	0.0012	138.0000	0.0865	104.1000	0.0452	111.3000
530	0.0012	138.0000	0.0869	104.1000	0.0458	111.1333
530.6	0.0008	137.7667	0.0874	104.1667	0.0454	111.2000
531.1	0.0010	137.8667	0.0873	104.2667	0.0453	111.3667

wave	blank μ_a	blank μ_s'	onex μ_a	onex μ_s'	twox μ_a	twox μ_s'
531.6	0.0010	137.5333	0.0880	104.0000	0.0459	111.2000
532.2	0.0009	137.8667	0.0880	104.0000	0.0455	111.1333
532.7	0.0009	137.6000	0.0882	104.0000	0.0460	111.0667
533.3	0.0009	137.8000	0.0885	103.9333	0.0459	111.0333
533.8	0.0008	137.6667	0.0886	103.8667	0.0465	110.9333
534.3	0.0006	137.8667	0.0886	103.9333	0.0462	111.1000
534.9	0.0014	137.5667	0.0895	103.8000	0.0464	111.0333
535.4	0.0011	137.7000	0.0891	103.8333	0.0461	111.1333
536	0.0011	137.6333	0.0895	103.7667	0.0473	110.8667
536.5	0.0010	137.6333	0.0890	103.8000	0.0470	110.8667
537	0.0009	137.7000	0.0895	103.7000	0.0391	113.3667
537.6	0.0009	137.4000	0.0890	103.7333	0.0410	112.6333
538.1	0.0013	137.6000	0.0892	103.8000	0.0469	110.9333
538.6	0.0012	137.8667	0.0897	103.7667	0.0473	110.8000
539.2	0.0010	137.5667	0.0891	103.7333	0.0464	110.8667
539.7	0.0011	137.5667	0.0890	103.6333	0.0464	110.8000
540.3	0.0012	137.7333	0.0894	103.7333	0.0467	110.9667
540.8	0.0014	137.5333	0.0900	103.6333	0.0465	110.8667
541.3	0.0012	137.5333	0.0895	103.6667	0.0466	110.9000
541.9	0.0010	137.9333	0.0889	103.8667	0.0465	111.1000
542.4	0.0011	137.5333	0.0887	103.7333	0.0399	113.0333
543	0.0015	137.5667	0.0887	103.9000	0.0462	111.0667
543.5	0.0011	137.6667	0.0880	103.8667	0.0409	112.6333
544	0.0010	137.7333	0.0877	103.9667	0.0460	111.0667
544.6	0.0013	137.6667	0.0878	103.9667	0.0461	111.0667
545.1	0.0014	137.4667	0.0874	103.9333	0.0458	110.9000
545.6	0.0012	137.5333	0.0876	103.9333	0.0457	111.0333
546.2	0.0010	137.6000	0.0864	103.9333	0.0398	112.8333
546.7	0.0012	137.5000	0.0868	104.0000	0.0396	112.9667
547.3	0.0011	137.7000	0.0858	104.0667	0.0397	112.6000
547.8	0.0013	137.6000	0.0861	104.1667	0.0302	116.0000
548.3	0.0013	137.6000	0.0858	104.2000	0.0336	114.6000
548.9	0.0011	137.4667	0.0851	104.2333	0.0379	113.2667
549.4	0.0013	137.4333	0.0847	104.2333	0.0397	112.3333
550	0.0009	137.5333	0.0837	104.3667	0.0323	114.8000
550.5	0.0014	137.3333	0.0837	104.3333	0.0368	113.3667
551	0.0009	137.7000	0.0828	104.6000	0.0338	114.3333
551.6	0.0008	137.6667	0.0826	104.5000	0.0291	115.6667
552.1	0.0012	137.5667	0.0821	104.4333	0.0371	112.9000
552.6	0.0009	137.4667	0.0814	104.6333	0.0370	112.8000
553.2	0.0007	137.4000	0.0807	104.6000	0.0379	112.4333
553.7	0.0009	137.2000	0.0805	104.6333	0.0274	115.7333
554.3	0.0009	137.4000	0.0799	104.7667	0.0391	112.0000

wave	blank μ_a	blank μ_s'	onex μ_a	onex μ_s'	twox μ_a	twox μ_s'
554.8	0.0013	137.4000	0.0796	104.8000	0.0364	113.0000
555.3	0.0009	137.2667	0.0784	104.9333	0.0306	114.4667
555.9	0.0014	137.2333	0.0780	104.8333	0.0302	114.4333
556.4	0.0014	137.0667	0.0778	104.9000	0.0320	113.9333
556.9	0.0008	137.4000	0.0767	105.2333	0.0288	114.9000
557.5	0.0010	137.2333	0.0762	105.0667	0.0304	114.1333
558	0.0011	137.0333	0.0754	105.1333	0.0349	112.6333
558.6	0.0010	137.1333	0.0750	105.2000	0.0216	116.8667
559.1	0.0012	137.1000	0.0746	105.3000	0.0226	116.6000
559.6	0.0012	137.1000	0.0745	105.3000	0.0282	114.3333
560.2	0.0015	136.9333	0.0733	105.4333	0.0218	116.6333
560.7	0.0010	136.9667	0.0724	105.5667	0.0300	113.8000
561.3	0.0009	137.0000	0.0718	105.6000	0.0191	117.1333
561.8	0.0010	136.9333	0.0709	105.7667	0.0289	114.0000
562.3	0.0009	136.9333	0.0705	105.7000	0.0283	114.0000
562.9	0.0011	136.8667	0.0696	105.7667	0.0276	114.4667
563.4	0.0007	136.8667	0.0688	105.8667	0.0277	113.8667
563.9	0.0008	137.0333	0.0683	106.0000	0.0243	115.1333
564.5	0.0009	136.8667	0.0674	106.0667	0.0270	114.1333
565	0.0011	136.8667	0.0670	106.1333	0.0232	115.2667
565.6	0.0008	137.0000	0.0665	106.3667	0.0218	115.7000
566.1	0.0010	136.8000	0.0655	106.2333	0.0215	115.7000
566.6	0.0010	137.0000	0.0648	106.4000	0.0192	116.2667
567.2	0.0008	136.8333	0.0642	106.3333	0.0201	115.7667
567.7	0.0013	136.7667	0.0638	106.4667	0.0238	114.3667
568.2	0.0012	136.8667	0.0628	106.5667	0.0201	115.8667
568.8	0.0011	136.7667	0.0621	106.7333	0.0276	113.1667
569.3	0.0011	136.9000	0.0614	106.9667	0.0253	113.9333
569.9	0.0011	136.8000	0.0607	106.8667	0.0271	113.0333
570.4	0.0008	136.6333	0.0598	106.9000	0.0252	113.4667
570.9	0.0010	136.7333	0.0594	107.1667	0.0238	113.9667
571.5	0.0008	136.6333	0.0582	107.3333	0.0188	115.4333
572	0.0011	136.6333	0.0583	107.3000	0.0268	112.9333
572.5	0.0011	136.6667	0.0577	107.3000	0.0265	112.8667
573.1	0.0013	136.6000	0.0575	107.2667	0.0216	114.4333
573.6	0.0011	136.6000	0.0563	107.5000	0.0249	113.2667
574.1	0.0012	136.5333	0.0499	109.3667	0.0208	114.5333
574.7	0.0015	136.5000	0.0500	109.3000	0.0248	113.2000
575.2	0.0013	136.7333	0.0488	109.6333	0.0238	113.3667
575.8	0.0011	136.6333	0.0528	108.1667	0.0161	115.9333
576.3	0.0013	136.5333	0.0504	108.8333	0.0242	113.1000
576.8	0.0011	136.4333	0.0450	110.3333	0.0193	114.5667
577.4	0.0011	136.5333	0.0446	110.4000	0.0211	113.8000

wave	blank μ_a	blank μ_s'	onex μ_a	onex μ_s'	twox μ_a	twox μ_s'
577.9	0.0011	136.3667	0.0459	109.8667	0.0176	114.8667
578.4	0.0012	136.3333	0.0464	109.6000	0.0172	115.2333
579	0.0013	136.5333	0.0460	109.6000	0.0154	115.8667
579.5	0.0014	136.6000	0.0431	110.5333	0.0206	113.8000
580.1	0.0010	136.5667	0.0429	110.5000	0.0211	113.5667
580.6	0.0012	136.3667	0.0476	108.8000	0.0209	113.4333
581.1	0.0009	136.5667	0.0427	110.2667	0.0208	113.3333
581.7	0.0011	136.7000	0.0439	109.8667	0.0185	114.3000
582.2	0.0011	136.5333	0.0475	108.6000	0.0188	114.0000
582.7	0.0015	136.4667	0.0404	110.9000	0.0172	114.6333
583.3	0.0011	136.5667	0.0391	111.2000	0.0197	113.6333
583.8	0.0016	136.2333	0.0407	110.4333	0.0184	113.8667
584.3	0.0015	136.3333	0.0396	110.8000	0.0163	114.6667
584.9	0.0013	136.3667	0.0383	111.1667	0.0192	113.6333
585.4	0.0014	136.1333	0.0284	114.2000	0.0189	113.5333
586	0.0018	136.4333	0.0308	113.3667	0.0191	113.6000
586.5	0.0014	136.2667	0.0441	109.0333	0.0158	114.4333
587	0.0017	136.1000	0.0323	112.7333	0.0170	114.1000
587.6	0.0017	136.1000	0.0255	114.7667	0.0169	114.0000
588.1	0.0016	136.3333	0.0319	112.6000	0.0169	114.0667
588.6	0.0014	136.2667	0.0169	117.4333	0.0171	113.8667
589.2	0.0017	136.1667	0.0202	116.0667	0.0151	114.4000
589.7	0.0014	136.2000	0.0288	113.2333	0.0165	113.9333
590.2	0.0017	136.1333	0.0270	113.8667	0.0138	114.7667
590.8	0.0011	136.2000	0.0348	111.1000	0.0162	113.7000
591.3	0.0016	136.0667	0.0235	114.8000	0.0162	113.9000
591.9	0.0015	136.0000	0.0265	113.8000	0.0164	113.7667
592.4	0.0012	136.0667	0.0302	112.4667	0.0114	115.3667
592.9	0.0014	136.2667	0.0329	111.6667	0.0153	114.1667
593.5	0.0016	136.3333	0.0255	113.9000	0.0156	114.0000
594	0.0013	136.0000	0.0287	112.6667	0.0150	113.9333
594.5	0.0016	135.9333	0.0250	113.8333	0.0149	113.9000
595.1	0.0016	135.7667	0.0229	114.5667	0.0148	113.8000
595.6	0.0015	136.0333	0.0266	113.3333	0.0147	114.0000
596.1	0.0013	135.9333	0.0265	113.1333	0.0144	114.0333
596.7	0.0014	135.7667	0.0271	112.8333	0.0142	114.1000
597.2	0.0017	135.8333	0.0254	113.3667	0.0141	114.0000
597.7	0.0014	135.6333	0.0206	114.8667	0.0137	114.0000
598.3	0.0015	135.6667	0.0220	114.3667	0.0136	114.0333
598.8	0.0010	135.9333	0.0287	112.3333	0.0135	114.0667
599.3	0.0014	135.7667	0.0227	114.1000	0.0131	114.0333
599.9	0.0014	135.6000	0.0299	111.5000	0.0130	113.9667
600.4	0.0013	135.4333	0.0286	111.7667	0.0128	114.0333

wave	blank μ_a	blank μ_s'	onex μ_a	onex μ_s'	twox μ_a	twox μ_s'
601	0.0013	135.5667	0.0251	113.0667	0.0129	114.1000
601.5	0.0012	135.5333	0.0277	112.0333	0.0123	114.1000
602	0.0015	135.3000	0.0260	112.5333	0.0122	114.0333
602.6	0.0012	135.5333	0.0319	110.7000	0.0123	114.1333
603.1	0.0012	135.6000	0.0200	114.4667	0.0119	114.1667
603.6	0.0015	135.4667	0.0237	113.1000	0.0118	114.1333
604.2	0.0014	135.2000	0.0186	114.5333	0.0116	113.9667
604.7	0.0012	135.3333	0.0253	112.5000	0.0114	114.0333
605.2	0.0011	135.4333	0.0235	112.9333	0.0113	114.1000
605.8	0.0011	135.4667	0.0207	113.8667	0.0109	114.2333
606.3	0.0012	135.1000	0.0252	112.2667	0.0108	114.0333
606.8	0.0010	135.2333	0.0271	111.6000	0.0098	114.3667
607.4	0.0012	135.2333	0.0206	113.8333	0.0106	114.2000
607.9	0.0015	135.2000	0.0313	110.3000	0.0106	114.1333
608.4	0.0012	135.2667	0.0257	111.9000	0.0105	114.0000
609	0.0012	134.9667	0.0263	111.6667	0.0104	113.9333
609.5	0.0009	135.2333	0.0233	112.6333	0.0097	114.2333
610	0.0012	134.9667	0.0261	111.6000	0.0097	114.0333
610.6	0.0012	135.1000	0.0232	112.7333	0.0101	114.0000
611.1	0.0011	135.1333	0.0230	112.5000	0.0095	114.1333
611.6	0.0014	135.2000	0.0231	112.5667	0.0099	114.1667
612.2	0.0013	135.0333	0.0239	112.2333	0.0085	114.4667
612.7	0.0011	135.0333	0.0244	111.9667	0.0091	114.1333
613.2	0.0009	135.1667	0.0198	113.4000	0.0089	114.2333
613.8	0.0011	135.1000	0.0241	112.0333	0.0093	114.0000
614.3	0.0010	135.1667	0.0240	112.2000	0.0090	114.2667
614.8	0.0013	135.0000	0.0254	111.4000	0.0089	114.1333
615.4	0.0011	134.9333	0.0228	112.2333	0.0089	114.3000
615.9	0.0011	134.8667	0.0159	114.6667	0.0093	114.1333
616.4	0.0010	135.0333	0.0266	111.0000	0.0084	114.3000
617	0.0012	135.0000	0.0221	112.5667	0.0088	114.2667
617.5	0.0010	134.7000	0.0249	111.2667	0.0085	114.0667
618	0.0012	134.8000	0.0278	110.5667	0.0086	114.1333
618.6	0.0013	134.6333	0.0221	112.3000	0.0083	114.2000
619.1	0.0014	134.7000	0.0264	110.8333	0.0084	114.0667
619.6	0.0013	134.6333	0.0234	111.6667	0.0083	113.9333
620.2	0.0013	134.7667	0.0272	110.6000	0.0082	114.0000
620.7	0.0014	134.8000	0.0246	111.5000	0.0082	114.1667
621.2	0.0015	134.6333	0.0219	112.0667	0.0084	113.9667
621.8	0.0015	134.6667	0.0211	112.4667	0.0079	114.2333
622.3	0.0013	134.8333	0.0229	111.9667	0.0076	114.2333
622.8	0.0013	134.6667	0.0262	110.7000	0.0075	114.2000
623.4	0.0014	134.7667	0.0247	111.1667	0.0075	114.4333

	blank	blank	onex	onex	twox	twox
wave	μ_a	μ_s'	μ_a	μ_s'	μ_a	μ_s'
623.9	0.0012	134.7667	0.0263	110.7000	0.0078	114.2667
624.4	0.0011	134.8667	0.0217	112.3000	0.0076	114.2667
625	0.0011	134.6667	0.0186	112.9667	0.0072	114.1333
625.5	0.0013	134.6000	0.0235	111.3667	0.0071	114.1000
626	0.0011	134.6333	0.0201	112.5333	0.0072	114.3000
626.6	0.0013	134.9000	0.0238	111.4667	0.0073	114.3333
627.1	0.0015	134.8333	0.0254	110.8667	0.0070	114.4000
627.6	0.0013	134.6667	0.0185	113.0667	0.0070	114.2000
628.2	0.0014	134.7667	0.0218	111.9333	0.0070	114.3000
628.7	0.0013	134.7333	0.0241	111.1667	0.0069	114.3667
629.2	0.0010	134.9000	0.0246	110.9667	0.0068	114.3000
629.8	0.0008	134.9000	0.0156	113.9333	0.0067	114.3333
630.3	0.0008	134.7000	0.0209	112.0000	0.0065	114.3333
630.8	0.0010	134.8000	0.0173	113.3000	0.0065	114.5333
631.4	0.0011	134.7000	0.0225	111.4667	0.0062	114.4333
631.9	0.0011	134.7667	0.0212	111.9333	0.0064	114.4000
632.4	0.0013	134.7000	0.0240	111.0667	0.0066	114.3333
632.9	0.0011	134.7333	0.0223	111.5667	0.0063	114.4333
633.5	0.0010	134.8333	0.0230	111.2000	0.0059	114.5333
634	0.0015	134.7333	0.0208	112.1000	0.0063	114.4667
634.5	0.0009	134.7667	0.0202	112.1333	0.0059	114.4333
635.1	0.0012	134.6333	0.0193	112.4333	0.0059	114.3667
635.6	0.0011	134.5333	0.0230	111.1333	0.0060	114.3333
636.1	0.0013	134.5000	0.0226	111.3000	0.0058	114.4000
636.7	0.0012	134.5000	0.0199	112.0000	0.0057	114.3667
637.2	0.0013	134.4667	0.0215	111.4667	0.0058	114.1667
637.7	0.0012	134.4667	0.0223	111.3000	0.0057	114.3000
638.3	0.0013	134.3333	0.0196	112.0667	0.0059	114.2000
638.8	0.0013	134.4667	0.0179	112.7000	0.0054	114.3333
639.3	0.0013	134.2000	0.0200	111.9000	0.0058	114.1333
639.8	0.0012	134.3333	0.0223	111.1667	0.0054	114.2000
640.4	0.0014	134.3667	0.0221	111.0333	0.0054	114.1667
640.9	0.0012	134.2667	0.0193	112.0000	0.0053	114.1333
641.4	0.0013	134.2333	0.0212	111.3333	0.0054	114.0333
642	0.0014	133.9333	0.0222	111.0333	0.0057	114.1000
642.5	0.0014	134.0667	0.0175	112.5000	0.0054	114.1333
643	0.0011	134.1000	0.0218	110.9667	0.0052	114.0667
643.6	0.0011	134.1000	0.0177	112.3333	0.0051	114.0667
644.1	0.0016	134.0000	0.0199	111.5667	0.0054	113.9667
644.6	0.0013	133.9000	0.0212	111.1667	0.0049	114.0000
645.1	0.0014	133.9000	0.0195	111.5667	0.0050	113.8333
645.7	0.0012	133.9667	0.0217	110.9333	0.0051	114.0000
646.2	0.0013	133.8333	0.0217	110.8667	0.0048	114.0000

	blank	blank	onex	onex	twox	twox
wave	μ_a	μ_s'	μ_a	μ_s'	μ_a	μ_s'
646.7	0.0012	133.8333	0.0169	112.4667	0.0050	113.9000
647.3	0.0011	133.9000	0.0194	111.4667	0.0048	113.9667
647.8	0.0012	133.7000	0.0211	110.8667	0.0046	113.9000
648.3	0.0013	133.5333	0.0208	110.9000	0.0046	113.8000
648.9	0.0015	133.4667	0.0197	111.3000	0.0046	113.8333
649.4	0.0013	133.5333	0.0196	111.2667	0.0046	113.9000
649.9	0.0015	133.5667	0.0196	111.1667	0.0046	113.9000
650.4	0.0014	133.4333	0.0208	110.7000	0.0047	113.6667
651	0.0014	133.4000	0.0209	110.8000	0.0046	113.7667
651.5	0.0012	133.4667	0.0202	110.8333	0.0040	113.8667
652	0.0010	133.3000	0.0176	111.6333	0.0043	113.6667
652.6	0.0011	133.5000	0.0205	110.7333	0.0046	113.7000
653.1	0.0012	133.4000	0.0206	110.7333	0.0045	113.6333
653.6	0.0012	133.4333	0.0203	110.8333	0.0041	113.7333
654.1	0.0013	133.1333	0.0186	111.3000	0.0039	113.6667
654.7	0.0009	133.2000	0.0198	110.8333	0.0038	113.6667
655.2	0.0013	133.3000	0.0199	110.8667	0.0041	113.6333
655.7	0.0011	133.1000	0.0193	110.8333	0.0038	113.6000
656.3	0.0011	133.1667	0.0196	110.7000	0.0036	113.6667
656.8	0.0012	133.0000	0.0193	110.8333	0.0041	113.4333
657.3	0.0012	133.2000	0.0194	110.8333	0.0040	113.6000
657.8	0.0012	133.1000	0.0184	111.1667	0.0040	113.5333
658.4	0.0011	133.1333	0.0196	110.7333	0.0036	113.5333
658.9	0.0010	133.2667	0.0170	111.5667	0.0037	113.7333
659.4	0.0014	132.9000	0.0194	110.7000	0.0039	113.5000
659.9	0.0011	133.0667	0.0187	110.8667	0.0037	113.6000
660.5	0.0009	132.9667	0.0190	110.7000	0.0034	113.5000
661	0.0010	133.0667	0.0191	110.7000	0.0035	113.4667
661.5	0.0010	132.9000	0.0187	110.7333	0.0034	113.5333
662.1	0.0012	133.0000	0.0191	110.7000	0.0035	113.4667
662.6	0.0012	132.8333	0.0189	110.7000	0.0033	113.5000
663.1	0.0011	132.8000	0.0184	110.7667	0.0034	113.4333
663.6	0.0010	132.7333	0.0188	110.6333	0.0034	113.4667
664.2	0.0008	133.0333	0.0184	110.8333	0.0030	113.7000
664.7	0.0011	132.8333	0.0177	110.9667	0.0031	113.4667
665.2	0.0010	132.8333	0.0174	110.9667	0.0031	113.5333
665.7	0.0011	132.7667	0.0183	110.7667	0.0030	113.5000
666.3	0.0009	132.9000	0.0180	110.8000	0.0030	113.5333
666.8	0.0010	132.8333	0.0160	111.3667	0.0028	113.4333
667.3	0.0008	132.9000	0.0179	110.7333	0.0030	113.5000
667.8	0.0008	132.7333	0.0183	110.7333	0.0032	113.4000
668.4	0.0008	132.8333	0.0178	110.7000	0.0030	113.3667
668.9	0.0007	132.8333	0.0177	110.7667	0.0029	113.4333

	blank	blank	onex	onex	twox	twox
wave	μ_a	μ_s'	μ_a	μ_s'	μ_a	μ_s'
669.4	0.0007	132.6667	0.0174	110.8667	0.0028	113.3000
669.9	0.0010	132.6667	0.0172	110.9000	0.0031	113.3667
670.5	0.0010	132.6333	0.0176	110.7000	0.0030	113.3333
671	0.0006	132.7667	0.0174	110.8000	0.0030	113.4000
671.5	0.0010	132.4333	0.0174	110.6667	0.0028	113.3667
672	0.0009	132.5333	0.0172	110.7333	0.0026	113.3667
672.6	0.0009	132.5000	0.0176	110.7000	0.0030	113.2667
673.1	0.0012	132.4333	0.0170	110.8000	0.0029	113.2333
673.6	0.0011	132.3333	0.0174	110.6333	0.0029	113.1333
674.1	0.0015	132.1000	0.0173	110.6333	0.0027	113.1667
674.7	0.0010	132.3000	0.0173	110.6000	0.0026	113.1667
675.2	0.0008	132.5000	0.0169	110.6000	0.0026	113.2000
675.7	0.0009	132.3000	0.0155	111.1667	0.0024	113.2000
676.2	0.0011	132.3000	0.0168	110.6667	0.0025	113.1333
676.8	0.0013	132.0333	0.0167	110.6667	0.0024	113.1000
677.3	0.0012	132.1000	0.0158	110.9333	0.0026	113.1667
677.8	0.0011	132.0000	0.0167	110.6000	0.0025	113.0333
678.3	0.0010	132.3667	0.0147	111.3667	0.0025	113.1333
678.9	0.0014	131.9333	0.0168	110.6333	0.0025	113.0000
679.4	0.0015	131.9333	0.0166	110.7000	0.0024	113.1333
679.9	0.0014	131.9667	0.0163	110.7000	0.0027	113.0333
680.4	0.0011	131.9333	0.0167	110.5000	0.0025	112.9333
681	0.0012	131.9000	0.0156	110.7667	0.0024	112.9667
681.5	0.0012	132.0000	0.0163	110.5333	0.0024	113.0333
682	0.0009	132.1000	0.0164	110.5333	0.0022	112.9000
682.5	0.0012	131.8667	0.0160	110.5000	0.0023	112.9333
683.1	0.0012	131.7333	0.0164	110.3333	0.0023	112.8333
683.6	0.0015	131.7667	0.0166	110.4000	0.0024	112.8000
684.1	0.0012	131.8667	0.0155	110.6667	0.0024	112.8000
684.6	0.0014	131.7333	0.0164	110.4667	0.0023	112.9333
685.1	0.0011	131.7333	0.0163	110.5667	0.0025	112.7667
685.7	0.0018	131.3000	0.0159	110.4667	0.0023	112.7667
686.2	0.0013	131.7667	0.0162	110.3667	0.0023	112.7000
686.7	0.0023	131.0333	0.0163	110.4000	0.0024	112.7333
687.2	0.0024	131.1667	0.0159	110.3667	0.0024	112.7667
687.8	0.0023	131.1000	0.0161	110.3000	0.0023	112.6333
688.3	0.0025	130.9000	0.0149	110.6000	0.0022	112.6333
688.8	0.0018	131.3333	0.0163	110.3000	0.0024	112.6333
689.3	0.0023	131.0667	0.0157	110.4000	0.0022	112.6000
689.8	0.0027	130.8333	0.0156	110.3333	0.0022	112.6667
690.4	0.0025	130.7000	0.0153	110.3000	0.0022	112.5667
690.9	0.0024	130.8000	0.0158	110.1667	0.0022	112.4667
691.4	0.0027	130.7667	0.0160	110.1333	0.0022	112.4667
691.9	0.0025	130.8000	0.0156	110.3000	0.0021	112.5667
692.4	0.0020	130.8667	0.0154	110.1333	0.0021	112.3000
693	0.0018	131.2333	0.0154	110.3333	0.0022	112.5667
693.5	0.0027	130.7000	0.0157	110.2000	0.0024	112.4000
694	0.0020	131.0333	0.0155	110.2000	0.0024	112.3333
694.5	0.0027	130.7667	0.0153	110.3333	0.0022	112.3667
695.1	0.0020	130.9667	0.0153	110.1667	0.0021	112.4000
695.6	0.0021	130.9667	0.0153	110.2667	0.0020	112.3667
696.1	0.0019	130.9333	0.0153	110.3000	0.0021	112.3000
696.6	0.0027	130.5667	0.0157	110.0667	0.0021	112.3333
697.1	0.0022	130.8333	0.0154	110.2000	0.0020	112.4333
697.7	0.0022	130.5667	0.0150	110.1333	0.0019	112.4000
698.2	0.0020	130.8000	0.0151	110.2333	0.0019	112.3000
698.7	0.0018	130.7333	0.0153	109.9333	0.0022	112.0667
699.2	0.0031	130.3333	0.0154	110.1667	0.0021	112.2000
699.7	0.0032	130.3333	0.0151	110.0000	0.0019	112.2333
700.3	0.0029	130.4000	0.0153	110.1000	0.0020	112.1333
700.8	0.0017	130.8333	0.0152	110.1667	0.0021	112.2000
701.3	0.0021	130.5000	0.0148	110.0667	0.0019	112.2000
701.8	0.0021	130.5667	0.0146	110.2333	0.0021	112.1667
702.3	0.0018	130.8000	0.0149	110.1333	0.0019	112.1333
702.8	0.0033	130.0667	0.0124	110.7667	0.0019	112.2333
703.4	0.0018	130.6667	0.0141	110.3333	0.0019	112.1333
703.9	0.0022	130.4000	0.0149	109.9667	0.0018	112.0333
704.4	0.0018	130.5333	0.0141	110.1667	0.0019	112.0333
704.9	0.0020	130.3667	0.0143	110.0000	0.0019	111.9667
705.4	0.0020	130.5333	0.0149	110.1000	0.0021	112.0333
706	0.0022	130.4000	0.0144	109.9667	0.0019	112.0000
706.5	0.0020	130.3000	0.0142	110.0333	0.0019	111.9333
707	0.0025	130.2333	0.0145	110.1000	0.0018	111.9333
707.5	0.0018	130.6333	0.0144	110.1000	0.0018	112.0667
708	0.0022	130.2667	0.0142	110.1667	0.0019	111.9667
708.5	0.0019	130.3667	0.0144	109.8333	0.0018	111.8667
709.1	0.0022	130.3333	0.0147	109.9000	0.0019	112.0000
709.6	0.0020	130.4000	0.0142	110.0333	0.0017	112.0333
710.1	0.0020	130.4333	0.0143	110.0667	0.0017	111.9000
710.6	0.0020	130.3000	0.0145	109.9000	0.0020	111.9667
711.1	0.0019	130.3000	0.0144	109.9333	0.0019	111.8000
711.7	0.0011	130.6000	0.0143	109.9667	0.0019	111.9333
712.2	0.0016	130.4000	0.0144	109.7667	0.0017	111.7333
712.7	0.0027	129.9333	0.0142	109.8333	0.0020	111.7667
713.2	0.0017	130.2667	0.0141	109.8000	0.0018	111.7000
713.7	0.0020	130.1667	0.0143	109.8667	0.0019	111.9000

wave	blank μ_a	blank μ_s'	onex μ_a	onex μ_s'	twox μ_a	twox μ_s'
714.2	0.0017	130.1667	0.0144	109.7333	0.0017	111.7333
714.8	0.0020	130.2333	0.0142	109.8333	0.0019	111.6667
715.3	0.0018	130.2333	0.0134	110.0667	0.0017	111.7333
715.8	0.0012	130.2333	0.0142	109.7000	0.0017	111.5000
716.3	0.0014	130.2333	0.0144	109.6000	0.0019	111.5667
716.8	0.0021	130.0667	0.0140	109.8000	0.0018	111.6000
717.3	0.0018	130.1667	0.0142	109.8000	0.0018	111.7000
717.8	0.0013	130.2000	0.0140	109.7000	0.0018	111.4667
718.4	0.0011	130.3667	0.0117	110.4333	0.0017	111.5333
718.9	0.0015	130.2000	0.0145	109.5667	0.0018	111.4333
719.4	0.0013	130.2667	0.0137	109.9667	0.0017	111.4667
719.9	0.0012	130.0000	0.0141	109.6667	0.0018	111.3000
720.4	0.0012	130.1333	0.0143	109.5333	0.0018	111.5000
720.9	0.0016	130.0667	0.0140	109.5667	0.0017	111.5000
721.4	0.0013	130.1667	0.0139	109.7000	0.0017	111.5000
722	0.0015	129.9333	0.0142	109.5667	0.0017	111.4333
722.5	0.0015	130.0000	0.0136	109.6667	0.0017	111.3333
723	0.0013	129.9667	0.0139	109.5000	0.0016	111.2667
723.5	0.0011	130.0000	0.0135	109.6667	0.0017	111.3000
724	0.0011	130.1000	0.0136	109.5667	0.0016	111.3333
724.5	0.0013	129.9667	0.0138	109.5000	0.0018	111.2667
725	0.0012	129.9667	0.0136	109.7000	0.0016	111.4667
725.6	0.0012	129.9000	0.0133	109.6333	0.0016	111.1333
726.1	0.0013	129.9333	0.0135	109.5667	0.0017	111.3667
726.6	0.0013	129.9333	0.0127	109.8000	0.0017	111.2000
727.1	0.0014	129.8000	0.0131	109.7667	0.0016	111.2667
727.6	0.0012	129.8000	0.0133	109.5000	0.0015	111.2000
728.1	0.0012	129.8667	0.0134	109.6333	0.0017	111.3333
728.6	0.0010	129.8333	0.0129	109.6667	0.0015	111.2000
729.1	0.0009	129.9333	0.0132	109.6667	0.0015	111.3333
729.7	0.0011	129.8000	0.0134	109.6000	0.0015	111.3333
730.2	0.0012	129.8000	0.0132	109.4333	0.0014	111.2000
730.7	0.0014	129.9333	0.0134	109.5667	0.0018	111.1667
731.2	0.0014	129.6000	0.0136	109.3667	0.0015	111.1000
731.7	0.0014	129.6333	0.0131	109.5333	0.0014	111.1000
732.2	0.0016	129.5333	0.0134	109.4333	0.0015	111.1000
732.7	0.0016	129.4667	0.0134	109.3333	0.0015	110.9667
733.2	0.0013	129.6333	0.0131	109.3333	0.0015	110.9333
733.8	0.0011	129.5333	0.0116	109.8333	0.0015	110.9667
734.3	0.0012	129.5333	0.0126	109.5667	0.0015	110.9000
734.8	0.0015	129.4333	0.0121	109.7333	0.0017	110.8333
735.3	0.0011	129.5667	0.0129	109.3667	0.0015	110.9667
735.8	0.0010	129.5667	0.0130	109.3333	0.0015	110.8000

wave	blank μ_a	blank μ_s'	onex μ_a	onex μ_s'	twox μ_a	twox μ_s'
736.3	0.0012	129.6000	0.0113	109.9667	0.0015	111.0333
736.8	0.0014	129.4000	0.0129	109.2667	0.0016	110.9333
737.3	0.0015	129.5000	0.0118	109.8000	0.0014	110.8667
737.8	0.0013	129.3333	0.0128	109.3333	0.0014	110.9000
738.4	0.0015	129.4667	0.0128	109.2667	0.0015	110.8333
738.9	0.0013	129.4667	0.0127	109.3667	0.0014	110.8333
739.4	0.0014	129.4667	0.0130	109.3333	0.0014	110.9667
739.9	0.0012	129.4333	0.0127	109.3000	0.0015	110.7333
740.4	0.0013	129.3000	0.0126	109.3333	0.0016	110.8667
740.9	0.0013	129.4667	0.0127	109.3667	0.0014	110.8000
741.4	0.0015	129.3333	0.0128	109.2667	0.0015	110.8333
741.9	0.0011	129.3333	0.0123	109.3667	0.0013	110.7333
742.4	0.0014	129.3000	0.0131	109.1333	0.0014	110.8000
742.9	0.0014	129.3667	0.0129	109.1667	0.0016	110.8000
743.4	0.0012	129.4000	0.0129	109.2333	0.0014	110.8333
744	0.0014	129.2667	0.0126	109.1667	0.0015	110.6667
744.5	0.0015	129.4000	0.0129	109.2333	0.0015	110.8333
745	0.0012	129.1333	0.0127	109.2333	0.0013	110.7000
745.5	0.0013	129.3333	0.0127	109.1667	0.0015	110.7667
746	0.0013	129.0667	0.0123	109.1000	0.0014	110.5667
746.5	0.0016	129.1667	0.0127	109.2333	0.0014	110.8333
747	0.0014	129.1000	0.0127	109.1000	0.0015	110.6000
747.5	0.0015	129.1000	0.0126	109.2667	0.0015	110.7000
748	0.0016	128.9667	0.0127	109.1000	0.0012	110.7667
748.5	0.0013	129.1667	0.0124	109.2000	0.0014	110.7000
749	0.0013	129.0667	0.0121	109.2667	0.0014	110.6333
749.5	0.0013	129.2667	0.0121	109.2667	0.0013	110.6333
750	0.0012	129.1667	0.0117	109.3667	0.0014	110.5333
750.5	0.0013	129.0333	0.0125	109.2000	0.0013	110.6333
751.1	0.0012	129.0333	0.0121	109.1667	0.0014	110.4667
751.6	0.0014	129.0000	0.0124	109.0333	0.0012	110.6000
752.1	0.0014	128.9667	0.0114	109.4333	0.0014	110.5333
752.6	0.0013	128.9333	0.0121	109.1333	0.0013	110.4667
753.1	0.0013	128.7000	0.0123	109.0000	0.0015	110.4000
753.6	0.0015	128.9333	0.0123	109.1667	0.0013	110.5333
754.1	0.0016	128.8000	0.0122	108.9333	0.0014	110.4000
754.6	0.0013	128.8000	0.0123	108.9667	0.0014	110.4000
755.1	0.0014	128.9333	0.0121	109.0333	0.0013	110.4333
755.6	0.0012	128.9333	0.0120	109.0333	0.0015	110.5000
756.1	0.0015	128.7000	0.0120	108.9667	0.0013	110.3333
756.6	0.0015	128.8000	0.0122	109.0333	0.0014	110.4667
757.1	0.0016	128.6000	0.0120	108.8333	0.0013	110.1667
757.6	0.0012	128.8667	0.0119	108.9000	0.0014	110.2000

wave	blank μ_a	blank μ_s'	onex μ_a	onex μ_s'	twox μ_a	twox μ_s'
758.1	0.0016	128.6000	0.0120	108.9000	0.0013	110.2333
758.6	0.0012	128.6667	0.0119	108.9000	0.0012	110.2667
759.1	0.0015	128.6000	0.0119	108.9667	0.0013	110.2333
759.6	0.0014	128.6000	0.0121	108.8667	0.0013	110.1667
760.1	0.0012	128.5333	0.0116	109.1333	0.0012	110.2000
760.7	0.0017	128.4333	0.0124	108.8333	0.0013	110.3000
761.2	0.0017	128.5000	0.0121	108.8333	0.0012	110.2000
761.7	0.0014	128.6667	0.0119	108.9333	0.0012	110.2333
762.2	0.0016	128.5000	0.0120	108.8000	0.0012	110.1333
762.7	0.0014	128.6333	0.0116	108.9667	0.0011	110.2333
763.2	0.0010	128.4000	0.0119	108.8333	0.0012	110.2000
763.7	0.0015	128.5000	0.0120	108.8333	0.0013	110.1333
764.2	0.0014	128.4333	0.0100	109.3333	0.0012	110.1000
764.7	0.0012	128.3333	0.0117	108.7000	0.0012	109.9667
765.2	0.0012	128.5333	0.0112	108.8000	0.0013	110.0667
765.7	0.0013	128.3333	0.0120	108.7333	0.0014	109.9000
766.2	0.0014	128.3000	0.0113	108.9333	0.0013	110.0000
766.7	0.0013	128.4333	0.0108	109.1333	0.0012	110.0667
767.2	0.0014	128.1333	0.0112	108.7333	0.0011	109.9000
767.7	0.0012	128.2667	0.0109	108.8333	0.0012	109.9333
768.2	0.0012	128.4000	0.0115	108.8333	0.0013	110.0333
768.7	0.0015	128.1333	0.0113	108.7333	0.0011	109.8333
769.2	0.0012	128.2000	0.0107	108.9667	0.0012	109.8000
769.7	0.0010	128.2667	0.0110	108.7667	0.0010	109.9000
770.2	0.0007	128.2667	0.0111	108.7667	0.0010	109.8000
770.7	0.0011	128.3333	0.0111	108.8000	0.0010	109.9667
771.2	0.0011	128.1333	0.0109	108.7667	0.0010	109.8333
771.7	0.0011	128.0000	0.0096	109.2000	0.0010	109.7333
772.2	0.0006	128.0667	0.0109	108.6000	0.0010	109.6333
772.7	0.0011	128.0667	0.0112	108.7333	0.0011	109.8333
773.2	0.0011	128.0667	0.0111	108.7000	0.0011	109.7333
773.7	0.0010	128.2333	0.0106	108.7000	0.0011	109.7000
774.2	0.0010	128.0667	0.0099	109.0000	0.0010	109.7333
774.7	0.0010	128.1333	0.0107	108.7667	0.0009	109.7667
775.2	0.0009	128.1000	0.0102	108.7000	0.0007	109.7000
775.7	0.0008	128.1333	0.0103	108.7667	0.0006	109.8000
776.2	0.0010	127.9667	0.0109	108.6667	0.0010	109.6000
776.7	0.0008	128.2333	0.0100	108.8000	0.0007	109.7000
777.2	0.0010	127.8667	0.0105	108.7667	0.0008	109.6000
777.7	0.0009	127.9333	0.0101	108.6000	0.0009	109.4667
778.2	0.0011	127.7667	0.0109	108.4667	0.0008	109.5333
778.7	0.0010	127.9667	0.0101	108.7333	0.0009	109.5333
779.2	0.0010	127.9000	0.0097	108.8667	0.0007	109.6333
779.7	0.0010	127.9000	0.0099	108.7333	0.0009	109.5000
780.2	0.0008	127.8000	0.0107	108.5667	0.0008	109.4000
780.7	0.0008	127.9667	0.0108	108.5333	0.0008	109.5000
781.2	0.0010	127.6333	0.0104	108.4333	0.0008	109.3667
781.7	0.0009	127.7000	0.0099	108.6667	0.0008	109.5000
782.2	0.0009	127.6333	0.0103	108.5000	0.0007	109.3667
782.6	0.0009	127.9333	0.0101	108.4333	0.0009	109.3000
783.1	0.0009	127.8333	0.0104	108.5667	0.0006	109.4000
783.6	0.0007	127.6333	0.0104	108.6000	0.0007	109.3000
784.1	0.0008	127.5667	0.0104	108.5333	0.0007	109.2000
784.6	0.0010	127.7333	0.0099	108.6333	0.0007	109.4667
785.1	0.0009	127.5333	0.0098	108.5333	0.0005	109.2000
785.6	0.0011	127.3333	0.0101	108.3667	0.0007	109.3667
786.1	0.0011	127.5000	0.0100	108.4333	0.0007	109.3333
786.6	0.0010	127.5000	0.0098	108.6000	0.0008	109.2333
787.1	0.0004	127.5333	0.0100	108.4333	0.0006	109.0333
787.6	0.0011	127.3333	0.0102	108.3333	0.0007	109.1333
788.1	0.0010	127.4000	0.0101	108.3000	0.0008	109.2667
788.6	0.0006	127.5667	0.0096	108.6667	0.0008	109.2333
789.1	0.0010	127.3333	0.0099	108.3333	0.0008	109.1333
789.6	0.0009	127.5333	0.0094	108.5333	0.0006	109.2000
790.1	0.0010	127.4667	0.0103	108.3333	0.0007	109.1333
790.6	0.0007	127.3333	0.0102	108.3667	0.0005	109.1333
791.1	0.0006	127.1667	0.0094	108.4667	0.0006	109.0000
791.6	0.0003	127.3000	0.0092	108.5333	0.0006	108.8667
792	0.0010	127.2333	0.0100	108.3667	0.0007	109.0000
792.5	0.0009	127.3000	0.0083	108.7667	0.0006	109.1333
793	0.0005	127.2333	0.0096	108.4000	0.0005	109.1000
793.5	0.0010	127.4000	0.0105	108.2333	0.0008	109.0333
794	0.0006	127.0333	0.0099	108.1667	0.0006	108.8000
794.5	0.0009	127.2333	0.0090	108.5333	0.0008	108.9000
795	0.0004	127.1000	0.0087	108.5000	0.0004	108.9000
795.5	0.0008	127.1000	0.0097	108.2000	0.0006	108.9000
796	0.0005	127.2000	0.0093	108.4000	0.0003	109.1333
796.5	0.0004	127.1333	0.0099	108.0333	0.0006	108.9000
797	0.0010	127.0667	0.0099	108.0667	0.0007	108.9333
797.5	0.0007	127.1000	0.0099	108.1333	0.0005	108.9333
798	0.0005	127.0333	0.0101	108.2333	0.0007	108.7000
798.4	0.0006	126.9333	0.0103	107.9667	0.0006	108.7000
798.9	0.0008	126.9333	0.0100	108.0667	0.0007	108.7000
799.4	0.0006	127.1667	0.0098	108.2000	0.0006	108.8333
799.9	0.0004	127.0333	0.0078	108.8000	0.0007	108.7333
800.4	0.0008	126.9000	0.0095	108.1333	0.0006	108.7000

wave	blank μ_a	blank μ_s'	onex μ_a	onex μ_s'	twox μ_a	twox μ_s'
800.9	0.0009	127.0000	0.0097	108.1667	0.0005	108.7333
801.4	0.0010	127.0000	0.0097	108.1333	0.0006	108.7667
801.9	0.0009	126.9333	0.0097	108.0000	0.0007	108.6667
802.4	0.0008	126.6667	0.0095	108.1333	0.0006	108.5667
802.9	0.0004	127.1000	0.0099	108.1000	0.0004	108.8000
803.3	0.0005	126.8000	0.0099	107.8333	0.0005	108.6000
803.8	0.0009	126.5667	0.0098	107.7000	0.0007	108.5333
804.3	0.0011	126.8000	0.0102	107.9000	0.0006	108.6667
804.8	0.0006	126.6333	0.0095	107.8000	0.0003	108.5000
805.3	0.0003	126.6667	0.0097	107.8333	0.0005	108.3000
805.8	0.0010	126.6667	0.0098	107.9000	0.0004	108.4333
806.3	0.0007	126.5333	0.0098	107.9667	0.0004	108.3000
806.8	0.0008	126.3333	0.0097	107.9333	0.0007	108.5000
807.2	0.0009	126.6667	0.0093	107.9000	0.0007	108.5333
807.7	0.0008	126.3000	0.0098	107.6000	0.0005	108.4667
808.2	0.0009	126.4333	0.0096	107.7667	0.0004	108.3667
808.7	0.0004	126.5667	0.0092	107.8667	0.0002	108.3667
809.2	0.0005	126.5000	0.0096	107.6667	0.0002	108.4000
809.7	0.0006	126.2333	0.0095	107.7333	0.0004	108.1667
810.2	0.0008	126.4000	0.0097	107.6667	0.0003	108.2667
810.7	0.0006	126.1000	0.0097	107.6000	0.0005	108.2333
811.1	0.0008	126.2333	0.0092	107.7333	0.0006	108.2667
811.6	0.0001	126.1667	0.0089	107.7667	0.0004	108.2000
812.1	0.0009	126.0667	0.0101	107.4000	0.0006	108.2000
812.6	0.0005	126.0667	0.0097	107.5000	0.0005	107.9333
813.1	0.0008	126.2333	0.0096	107.6000	0.0006	108.0667
813.6	0.0004	126.3667	0.0098	107.6000	0.0006	107.9667
814.1	0.0008	126.2333	0.0095	107.5333	0.0006	107.9000
814.5	0.0005	125.9667	0.0094	107.4000	0.0005	107.9667
815	0.0010	126.0000	0.0097	107.4667	0.0004	108.0667
815.5	0.0010	125.8333	0.0099	107.3333	0.0005	107.9000
816	0.0010	125.9667	0.0095	107.6000	0.0005	108.0333
816.5	0.0009	125.8333	0.0098	107.5667	0.0001	108.0000
817	0.0004	125.9000	0.0092	107.4667	0.0005	107.8667
817.4	0.0008	125.9333	0.0101	107.4667	0.0004	107.9000
817.9	0.0006	126.0667	0.0101	107.3667	0.0004	107.8000
818.4	0.0003	125.8667	0.0087	107.5667	0.0003	107.7000
818.9	0.0006	125.7667	0.0093	107.3333	0.0005	107.7667
819.4	0.0008	125.8000	0.0096	107.3000	0.0007	107.7000
819.9	0.0007	125.9333	0.0091	107.5000	0.0003	107.8333
820.3	0.0008	125.7333	0.0096	107.3667	0.0005	107.6000
820.8	0.0007	125.8667	0.0097	107.5000	0.0005	107.8000
821.3	0.0004	125.6667	0.0095	107.5667	0.0007	107.7667

wave	blank μ_a	blank μ_s'	onex μ_a	onex μ_s'	twox μ_a	twox μ_s'
821.8	0.0006	125.8667	0.0099	107.3667	0.0004	107.7000
822.3	0.0006	125.4000	0.0101	107.1667	0.0004	107.5667
822.7	0.0005	125.7333	0.0095	107.3333	0.0005	107.7333
823.2	0.0003	125.6667	0.0095	107.3667	0.0003	107.9667
823.7	0.0008	125.4333	0.0089	107.2333	0.0001	107.6667
824.2	0.0006	125.6000	0.0096	107.3667	0.0003	107.6333
824.7	0.0005	125.7333	0.0090	107.4000	0.0003	107.6667
825.2	0.0008	125.4000	0.0097	107.2667	0.0006	107.6333
825.6	0.0006	125.6667	0.0098	107.0667	0.0001	107.5333
826.1	0.0005	125.4667	0.0089	107.1667	0.0004	107.3000
826.6	0.0003	125.6667	0.0095	107.2000	0.0005	107.5667
827.1	0.0005	125.3333	0.0092	107.2333	0.0004	107.4000
827.6	0.0006	125.4333	0.0095	107.3000	0.0005	107.5667
828	0.0002	125.3667	0.0092	107.1000	0.0004	107.5333
828.5	0.0002	125.1333	0.0093	107.2333	0.0003	107.4000
829	0.0007	125.0333	0.0094	107.0333	0.0004	107.3333
829.5	0.0007	125.1333	0.0097	107.0333	0.0002	107.4000
829.9	0.0002	125.0667	0.0088	107.1333	0.0005	107.3333
830.4	0.0004	125.4667	0.0101	106.9667	0.0005	107.4667
830.9	0.0006	125.0667	0.0097	106.8667	0.0003	107.3333
831.4	0.0004	125.2667	0.0094	106.9667	0.0005	107.3333
831.9	0.0008	124.9000	0.0101	106.9667	0.0004	107.2333
832.3	0.0008	125.3333	0.0093	107.1333	0.0006	107.3333
832.8	0.0006	125.3333	0.0101	106.8667	0.0005	107.1667
833.3	0.0004	124.9000	0.0093	106.8000	0.0000	107.1667
833.8	0.0003	125.1667	0.0090	107.0667	0.0001	107.3333
834.2	0.0005	125.2333	0.0099	107.0000	0.0004	107.2333
834.7	0.0002	124.7667	0.0093	106.9000	0.0004	107.1333
835.2	0.0002	124.8667	0.0095	106.9667	0.0003	107.3000
835.7	0.0006	124.9333	0.0097	106.6667	0.0002	107.1667
836.1	0.0003	124.9667	0.0096	106.7333	0.0003	107.1667
836.6	0.0010	124.7333	0.0096	106.6667	0.0004	106.9667
837.1	0.0010	124.9667	0.0094	107.0000	0.0004	107.2000
837.6	0.0005	124.6000	0.0098	106.7667	0.0002	106.8667
838	0.0003	124.7000	0.0091	106.9333	0.0000	107.0333
838.5	0.0006	124.5333	0.0093	106.9000	0.0003	106.8333
839	0.0003	124.7000	0.0094	106.7000	0.0004	107.0000
839.5	0.0005	124.6333	0.0099	106.6000	0.0005	106.8667
839.9	0.0003	124.5667	0.0096	106.6667	0.0003	107.0667
840.4	0.0004	124.3333	0.0094	106.6667	0.0000	106.7667
840.9	0.0003	124.7000	0.0089	106.7000	0.0001	106.7000
841.4	0.0004	124.6000	0.0089	106.9333	0.0002	106.9000
841.8	0.0004	124.6333	0.0094	106.5667	0.0001	106.9333

wave	blank μ_a	blank μ'_s	onex μ_a	onex μ'_s	twox μ_a	twox μ'_s
842.3	0.0005	124.5000	0.0088	106.7667	0.0001	106.7333
842.8	0.0005	124.5333	0.0094	106.5333	0.0004	106.6333
843.3	0.0008	124.2333	0.0090	106.4667	0.0002	106.6000
843.7	0.0001	124.4333	0.0088	106.7000	0.0001	106.8000
844.2	0.0004	124.1667	0.0092	106.5333	0.0004	106.6333
844.7	0.0003	124.3667	0.0101	106.3000	0.0004	106.7333
845.1	0.0006	124.6667	0.0099	106.6333	0.0005	106.8333
845.6	0.0006	124.6667	0.0097	106.5333	0.0006	106.7667
846.1	0.0005	124.5333	0.0099	106.6667	0.0005	106.8000
846.6	0.0002	124.3667	0.0093	106.5667	0.0002	106.9667
847	0.0003	124.6000	0.0091	106.7667	0.0002	106.6333
847.5	0.0003	124.6667	0.0093	106.7000	0.0006	106.9667
848	0.0006	124.1333	0.0091	106.4000	0.0001	106.4667
848.4	0.0003	124.4333	0.0092	106.6333	0.0002	106.9000
848.9	0.0000	124.3333	0.0094	106.6667	0.0001	106.8333
849.4	0.0006	124.5667	0.0095	106.6333	0.0001	106.6000
849.8	0.0005	124.3333	0.0101	106.5000	0.0002	106.6000
850.3	0.0007	124.1333	0.0093	106.4333	0.0004	106.6667
850.8	0.0005	124.2667	0.0095	106.4667	0.0001	106.5667
851.3	0.0003	124.0333	0.0093	106.4333	0.0002	106.6333
851.7	0.0007	124.3000	0.0105	106.2667	0.0003	106.6000
852.2	0.0006	124.0000	0.0105	106.1667	0.0003	106.4667
852.7	0.0007	124.2667	0.0097	106.5333	0.0002	106.5000
853.1	0.0006	124.1333	0.0098	106.3667	0.0004	106.5000
853.6	0.0002	124.0667	0.0092	106.4667	0.0000	106.5000
854.1	0.0004	124.0000	0.0088	106.5000	0.0001	106.3667
854.5	0.0003	124.1667	0.0090	106.4667	0.0001	106.5000
855	0.0007	124.0667	0.0097	106.3000	0.0006	106.6000
855.5	0.0003	124.0000	0.0095	106.3333	0.0002	106.5333
855.9	0.0002	123.8667	0.0095	106.4333	0.0001	106.4667
856.4	0.0000	123.9333	0.0095	106.3000	0.0003	106.3333
856.9	0.0004	123.9667	0.0093	106.2000	0.0003	106.2000
857.3	0.0008	123.9000	0.0094	106.5000	0.0002	106.6667
857.8	0.0001	124.1667	0.0091	106.6667	0.0001	106.4333
858.3	0.0003	123.7000	0.0089	106.2000	0.0000	106.0000
858.7	0.0001	123.3000	0.0089	106.0333	0.0000	106.0000
859.2	0.0002	123.7000	0.0091	106.3667	0.0000	106.0667
859.7	0.0004	123.7667	0.0094	106.1333	0.0001	106.1333
860.1	0.0002	123.8667	0.0091	106.3667	0.0001	106.2000
860.6	0.0004	123.8333	0.0104	106.0667	0.0005	106.1667
861.1	0.0008	123.7333	0.0104	105.9667	0.0004	106.3333
861.5	0.0004	123.8667	0.0099	106.3333	0.0003	106.0333
862	0.0010	123.6000	0.0099	106.3000	0.0004	106.4667

wave	blank μ_a	blank μ'_s	onex μ_a	onex μ'_s	twox μ_a	twox μ'_s
862.4	0.0005	123.6333	0.0100	106.2333	0.0000	105.9000
862.9	0.0010	123.5000	0.0097	106.0333	0.0002	106.1000
863.4	0.0004	123.5333	0.0096	106.1333	0.0000	106.0333
863.8	0.0000	123.6667	0.0092	106.2000	0.0001	106.0333
864.3	0.0005	123.6000	0.0092	106.3333	0.0002	106.2000
864.8	0.0002	123.5333	0.0090	106.3333	0.0002	106.2667
865.2	0.0000	123.2333	0.0095	105.8333	0.0001	105.9667
865.7	0.0003	123.3333	0.0099	106.2333	0.0003	105.7667
866.1	0.0002	123.4333	0.0096	105.9333	0.0003	105.7333
866.6	0.0005	123.4333	0.0102	106.0667	0.0000	105.5000
867.1	0.0006	123.1000	0.0097	105.9333	0.0000	105.9667
867.5	0.0005	123.3667	0.0093	106.1333	0.0005	106.0333
868	0.0009	123.1000	0.0104	105.6000	0.0006	105.7333
868.5	0.0007	123.3333	0.0102	105.9667	0.0005	105.7667
868.9	0.0001	122.9667	0.0097	105.7667	0.0001	105.5667
869.4	0.0005	123.2000	0.0100	105.8000	0.0002	105.9667
869.8	0.0003	123.4667	0.0100	105.9000	0.0002	105.8000
870.3	0.0003	122.9667	0.0096	105.7667	0.0000	105.3333
870.8	0.0002	123.5333	0.0095	105.7000	0.0002	105.6333
871.2	0.0003	123.0667	0.0095	105.8333	0.0002	105.7667
871.7	0.0006	122.5667	0.0101	105.2000	0.0001	105.4333
872.1	0.0000	122.6333	0.0097	105.6667	0.0002	105.5667
872.6	0.0000	122.8333	0.0100	105.7667	0.0000	105.4333
873	0.0006	122.9667	0.0107	105.6000	0.0002	105.7333
873.5	0.0003	122.9667	0.0100	105.9000	0.0001	105.6667
874	0.0002	122.9667	0.0098	105.8000	0.0000	105.5000
874.4	0.0004	122.9000	0.0110	105.5333	0.0001	105.6000
874.9	0.0004	123.1333	0.0093	106.0333	0.0000	105.5333
875.3	0.0010	123.2000	0.0106	105.6000	0.0000	105.7000
875.8	0.0011	122.7667	0.0104	105.7667	0.0005	104.8667
876.2	0.0003	122.6333	0.0096	105.4000	0.0000	104.8333
876.7	0.0000	122.1667	0.0089	105.3000	0.0000	104.3000
877.2	0.0000	120.4667	0.0084	104.9333	0.0000	103.9000
877.6	0.0000	118.9333	0.0070	103.2667	0.0008	103.9000
878.1	0.0079	129.5333	0.0159	107.9000	0.0094	110.6333

7.1 Tabulated Anisotropy Data

The single scattering anisotropy was constant g=0.600000000

Appendix C

Example application of the laser calorimetry: characterizing zebra fish embryo with 1064 nm resonance GNRs

This appendix describes a cryopreservation study led by Mr. Kanav Khosla, where the laser calorimetry method was used to provide with a precise heat source term in estimating the cryopreserved embryo re-warming speed. The author performed the measurement experiment for this work. Full text of this paper is available at

https://pubs.acs.org/doi/abs/10.1021/acsnano.7b02216

- Khosla, K., **Wang, Y.**, Hagedorn, M., Qin, Z., & Bischof, J. "Gold nanorod induced warming of embryos from the cryogenic state enhances viability". *ACS nano*, *11*(8), 7869-7878. (2017).

Abstract

Zebrafish embryos can attain a stable cryogenic state by microinjection of cryoprotectants followed by rapid cooling, but the massive size of the embryo has consistently led to failure during the convective warming process. Here we address this zebrafish cryopreservation problem by using gold nanorods (GNRs) to assist in the warming process. Specifically, we microinjected the cryoprotectant propylene glycol into zebrafish embryos along with GNRs, and the samples were cooled at a rate of 90 000 °C/min in liquid nitrogen. We demonstrated the ability to unfreeze the zebrafish rapidly (1.4×10^7 °C/min) by irradiating the sample with a 1064 nm laser pulse for

1 ms due to the excitation of GNRs. This rapid warming process led to the outrunning of ice formation, which can damage the embryos. The results from 14 trials (n = 223) demonstrated viable embryos with consistent structure at 1 h (31%) and continuing development at 3 h (17%) and movement at 24 h (10%) post-warming. This compares starkly with 0% viability, structure, or movement at all time points in convectively warmed controls (n = 50, p < 0.001, ANOVA). Our nanoparticle-based warming process could be applied to the storage of fish, and with proper modification, can potentially be used for other vertebrate embryos.

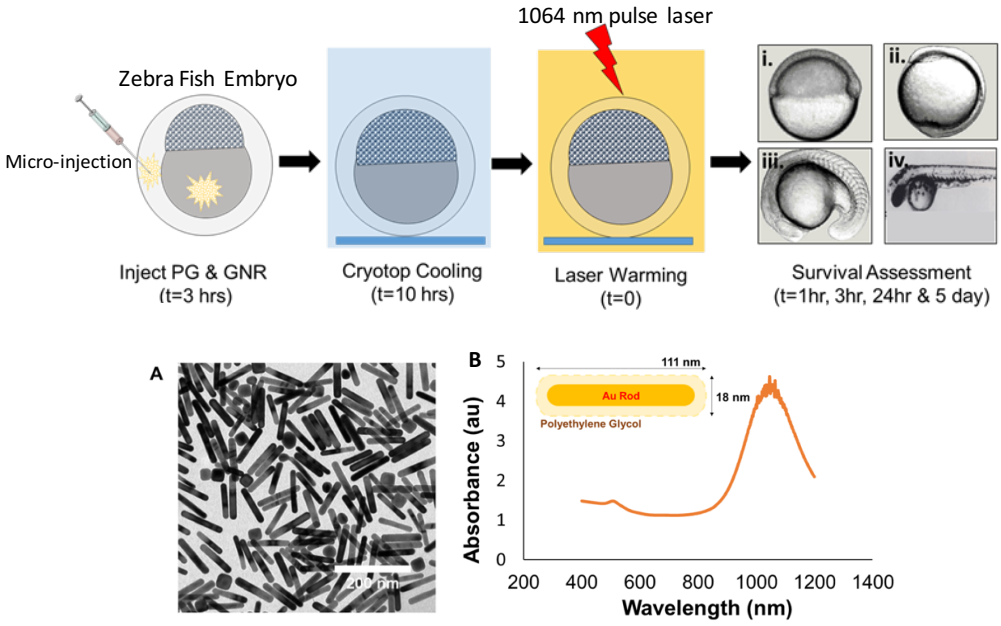

Principle Figure. (**Up**) Overview of the cryopreservation (injection, freezing and warming). (**Down**) Characterization of the GNR used in the zebrafish embryo cryopreservation. (**A**) TEM images of GNR, coated with polyethylene glycol suspended in Milipore water. (**B**) Extinction spectrum shows the plasmon peak at 1064 nm.

Appendix D

DDA simulation results of GNS aggregations

absorption and scattering cross section plots

- 5 nm GNS aggregations

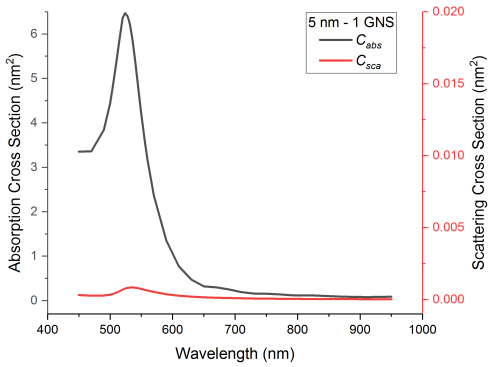

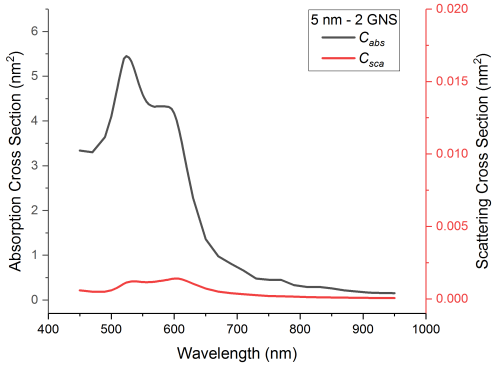

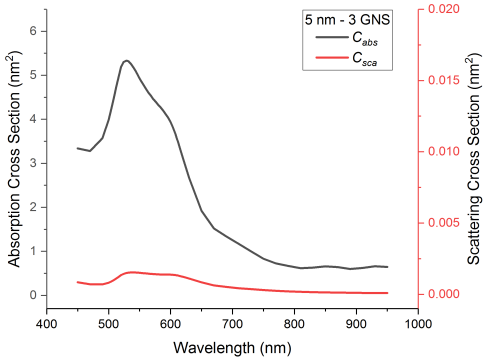

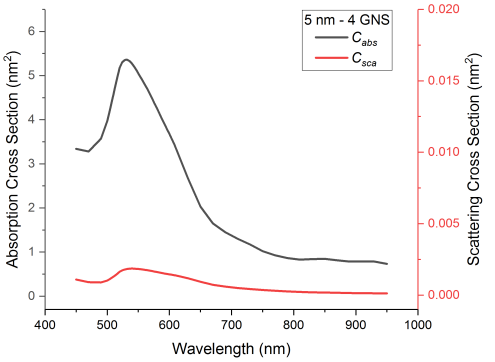

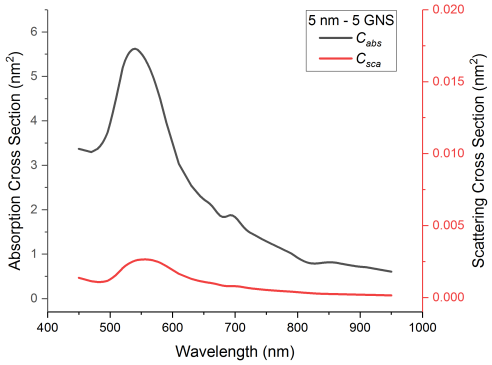

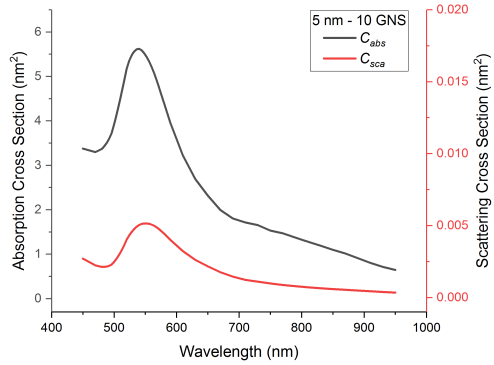

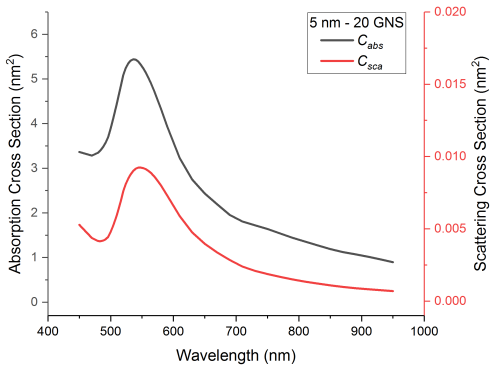

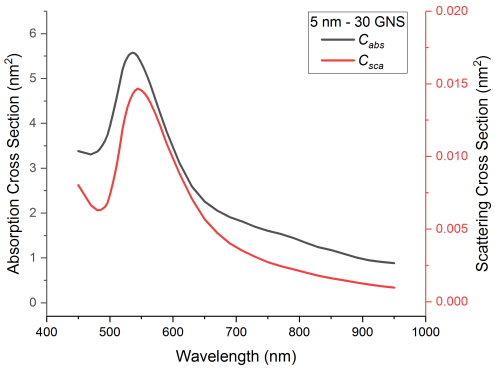

- 16 nm GNS aggregations

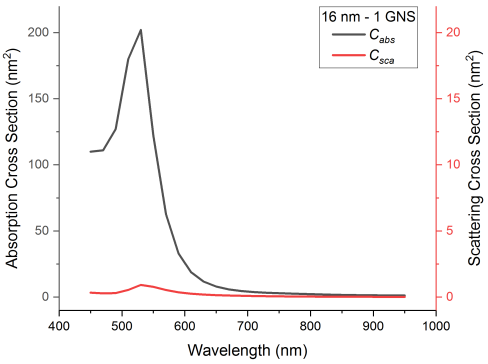

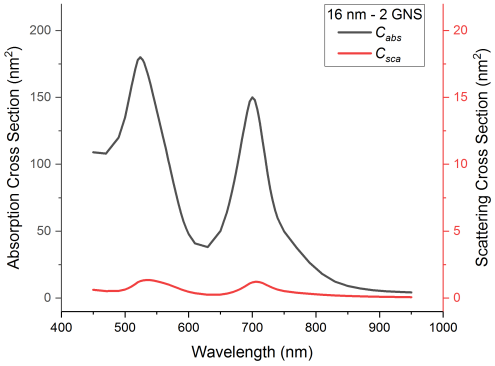

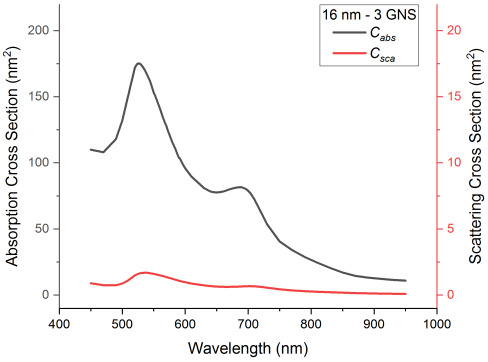

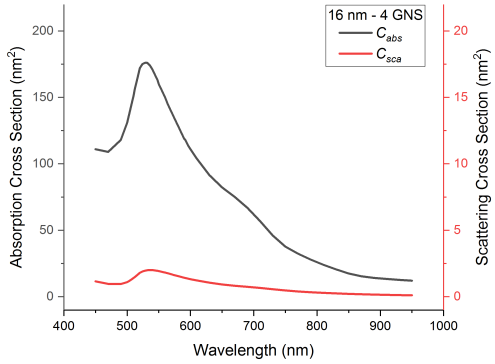

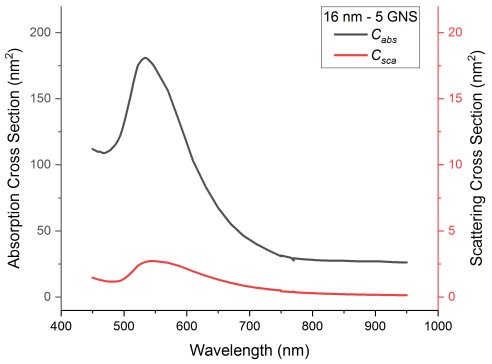

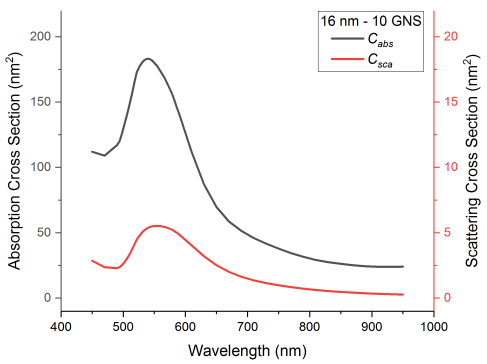

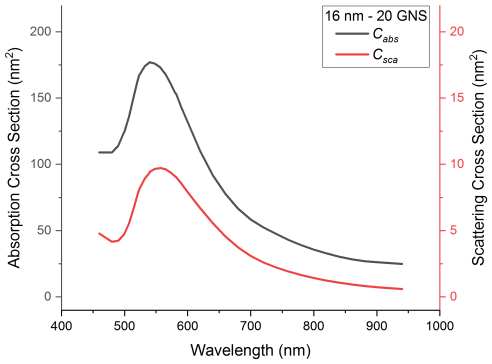

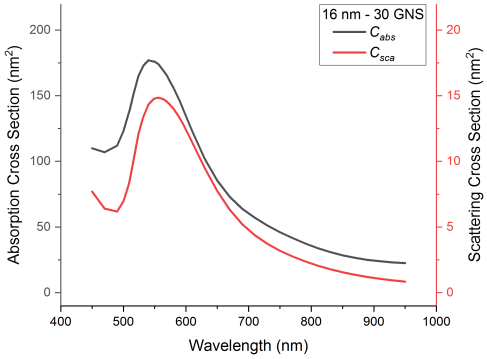

- 30 nm GNS aggregations

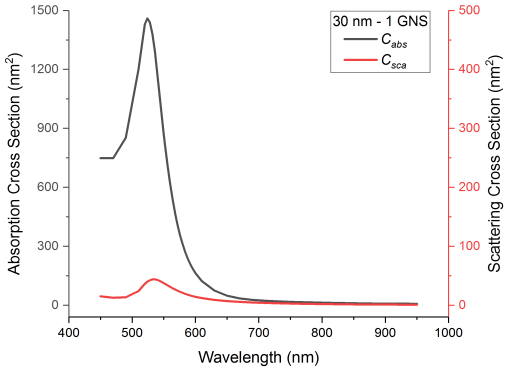

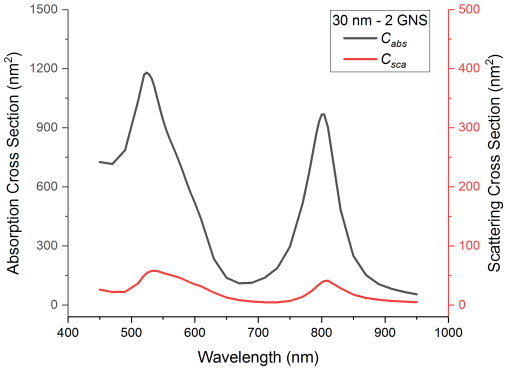

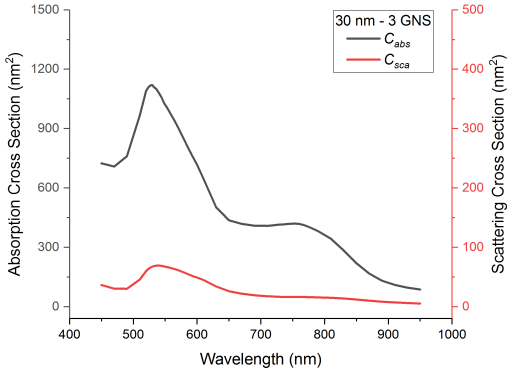
30 nm - 3 GNS
C_{abs}
C_{sca}
Absorption Cross Section (nm^2)
Scattering Cross Section (nm^2)
Wavelength (nm)
0
300
600
900
1200
1500
0
100
200
300
400
500
400
500
600
700
800
900
1000

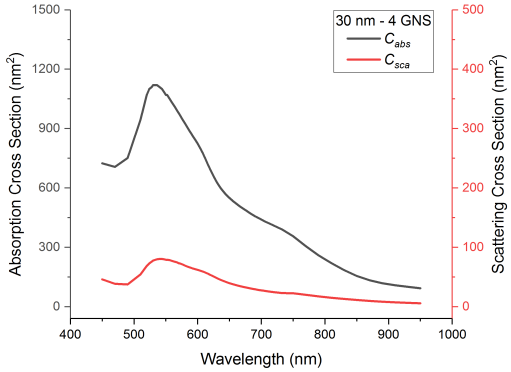
30 nm - 4 GNS
C_{abs}
C_{sca}
Absorption Cross Section (nm^2)
Scattering Cross Section (nm^2)
Wavelength (nm)
0
300
600
900
1200
1500
0
100
200
300
400
500
400
500
600
700
800
900
1000

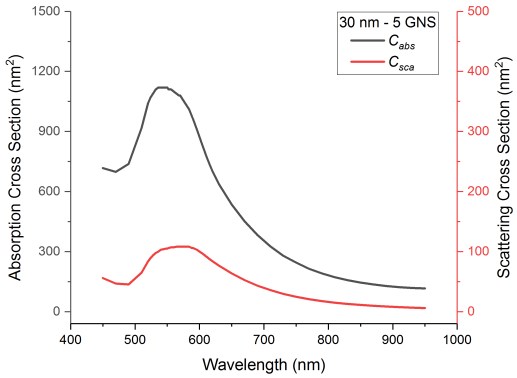
30 nm - 5 GNS
C_{abs}
C_{sca}
Absorption Cross Section (nm^2)
Scattering Cross Section (nm^2)
Wavelength (nm)
0
300
600
900
1200
1500
0
100
200
300
400
500
400
500
600
700
800
900
1000

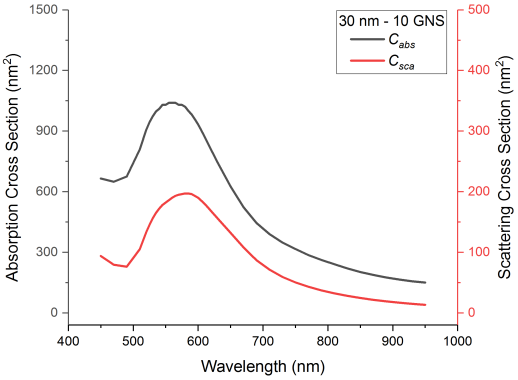
30 nm - 10 GNS
C_{abs}
C_{sca}
Absorption Cross Section (nm^2)
Scattering Cross Section (nm^2)
Wavelength (nm)
0
300
600
900
1200
1500
0
100
200
300
400
500
400
500
600
700
800
900
1000

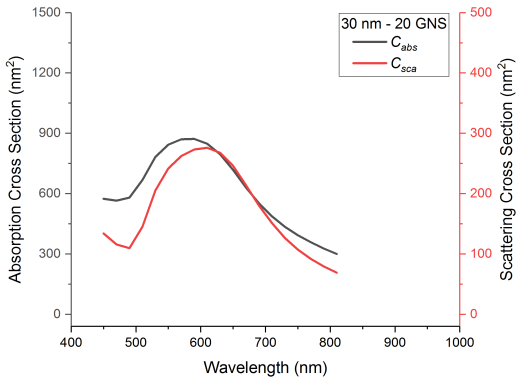
30 nm - 20 GNS
C_{abs}
C_{sca}
Absorption Cross Section (nm^2)
Scattering Cross Section (nm^2)
Wavelength (nm)
0
300
600
900
1200
1500
0
100
200
300
400
500
400
500
600
700
800
900
1000

- Sparse Geometries